

AN ABSTRACT OF THE THESIS OF

Christopher L. Duncan for the degree of Master of Science in Radiation Health Physics presented on June 8, 2011.

Title: Prototyping a Triple-Layer Phoswich Detection System

Abstract approved:

David M. Hamby

Multi-layer optically coupled scintillation based radiation detectors, known as phoswich detectors, have rapidly evolved in recent years. During the same time, digital signal processing has improved radiation discrimination accuracy and enhanced reliability, while reducing complexity and size of traditional analog signal processing methods. A new generation of high-speed radiation detectors that can measure mixed radiation fields has been developed by coupling these advancements. A prototype of one of the first commercially available phoswich detection systems has been analyzed to determine operational characteristics. The phoswich detector was analyzed using a variety of radioactive sources across a battery of tests compiled from the literature, Federal government regulations, and end-users specifications. It was found that the phoswich detection system operates equally well in beta particle, gamma-ray, and combined radiation fields. Testing at 5 centimeters demonstrated the phoswich detector's gamma-ray full-energy-peak intrinsic efficiency to range from 0.64 to 3.25 percent, full-energy-peak resolution from 6.29 (1332 keV) to 12.07 (356 keV) percent, and detectable energy range from 30 keV to 2754 keV. Similar testing for beta particles demonstrated an intrinsic efficiency of up to 58 percent. The system did exhibit saturation in radiation fields above 0.008 μCi when used with MATLAB. The phoswich detection system demonstrated that it is quite capable of accurately measuring the type and energy of radiation present in combined beta particle and gamma-ray radiation fields.

© Copyright by Christopher L. Duncan

June 8, 2011

All Rights Reserved

Prototyping a Triple-Layer Phoswich Detection System

by

Christopher L. Duncan

A THESIS

submitted to

Oregon State University

in partial fulfillment of
the requirements for the
degree of

Master of Science

Presented June 8, 2011

Commencement June 2012

Master of Science thesis of Christopher L. Duncan
presented on June 8, 2011.

APPROVED:

Major Professor, representing Radiation Health Physics

Head of the Department of Nuclear Engineering and Radiation Health Physics

Dean of the Graduate School

I understand that my thesis will become part of the permanent collection of Oregon State University libraries. My signature below authorizes release of my thesis to any reader upon request.

Christopher L. Duncan, Author

ACKNOWLEDGEMENTS

I would like to acknowledge the help provided by several people throughout my graduate education. First, I greatly appreciate the numerous technical discussions and brainstorming sessions held with my two lab-mates; Abdulsalam Alhawsawi and Bemnet Alemayehu. I learned a good deal about different MATLAB coding techniques from my friend Javad Azimi. Dr. Abi Farsoni enhanced my understanding of the electronics, both analog and digital used throughout this work. Finally, I owe much to Dr. David Hamby. His guidance, patience, and tact was integral in my learning throughout the whole program.

TABLE OF CONTENTS

	<u>Page</u>
1 Introduction	1
1.1 Overview	1
1.2 Objective and Intent	2
2 Literature Review	3
2.1 Radioactive Transformations	3
2.2 Isobaric Transformations	5
2.2.1 Negatron (β^-) Transformation	6
2.2.2 Negatron (β^-) Interactions	7
2.2.3 Positron (β^+) Transformation	10
2.2.4 Positron (β^+) Interactions	11
2.2.5 Electron Capture Transformation	12
2.3 Alpha Transformation	12
2.3.1 Alpha Interactions	14
2.4 Isometric Transitions	15
2.4.1 Gamma-Rays	16
2.4.2 Gamma-Ray Interactions	16
2.4.3 Internal Conversion	20
2.5 Atomic Transitions	20
2.6 Scintillation Detection Systems	21
2.6.1 Scintillation Physics	22
2.6.2 Photomultiplier Tube	24
2.6.3 Phoswich Principles	26
2.6.4 Digital Pulse Processing	28
2.6.5 Pulse Shape Discrimination	29
3 Materials and Methods	32
3.1 Prototype Triple-Layer Phoswich	32
3.2 Phoswich Detection System	35
3.2.1 Analog Electronics	36
3.2.2 Digital Pulse Processor	36

TABLE OF CONTENTS (Continued)

	<u>Page</u>
3.3 MATLAB Algorithm.....	37
3.3.1 Offset and Gain	41
3.3.2 Threshold	42
3.3.3 Relaxation Correction	43
3.3.4 Fast Component Ratio and Slow Component Ratio Regions	45
3.3.5 Optimal Filter Size	48
3.4 Radioactive Sources	48
3.5 Characterization Tests.....	50
3.5.1 System Efficiency with varying Energy.....	50
3.5.2 System Efficiency with varying Count Rate.....	52
3.5.3 Effective Range of Measurement	52
3.5.4 Resolution with Varying Energy	52
3.5.5 Minimum Detectable Activity	53
3.5.6 Pulse Discrimination Time.....	54
3.5.7 Digital Pulse Processor Programming Time	54
4 Results.....	56
4.1 System Efficiency with Varying Energy	56
4.2 System Efficiency with Varying Count Rate	57
4.3 Effective Range of Measurement	60
4.4 Resolution with Varying Energy	62
4.5 Minimum Detectable Activity	62
4.6 Pulse Discrimination Time.....	63
4.7 Digital Pulse Processor Programming Time	64
5 Discussions	65
5.1 System Efficiency with Varying Energy	70
5.2 System Efficiency with Varying Count Rate	75
5.3 Effective Range of Measurement	82
5.4 Resolution with Varying Energy	82
5.5 Minimum Detectable Activity	86

TABLE OF CONTENTS (Continued)

	<u>Page</u>
5.6 Pulse Discrimination Time.....	88
5.7 Digital Pulse Processor Programming Time	89
6 Conclusion and Future Work	91
6.1 Conclusion.....	91
6.2 Future Work	92
7 Bibliography	94
8 Appendix A (Real Time MATLAB Algorithm)	98
9 Appendix B (Filter Sizes).....	101

LIST OF FIGURES

<u>Figure</u>	<u>Page</u>
Figure 2-1: Orbital electron shell configuration.....	3
Figure 2-2: Nuclear shell configuration.....	4
Figure 2-3: Nuclide stability chart	5
Figure 2-4: Conversion of a d quark into a u quark	6
Figure 2-5: Beta particle spectrum from ^{14}C	7
Figure 2-6: Path of an electron, producing electromagnetic radiation to conserve energy	9
Figure 2-7: Constructive interference producing Cerenkov radiation	9
Figure 2-8: Positron energy spectrum for ^{64}Cu	11
Figure 2-9: Positronium annihilating into two photons of equal energy	12
Figure 2-10: Alpha transformation inside a nucleus' potential well.....	13
Figure 2-11: Ion production during an Alpha particle track	14
Figure 2-12: ^{137}Cs beta transformation followed by gamma-ray or conversion electron emission from the progeny atom	16
Figure 2-13: Gamma-ray interaction probability with varying gamma-ray energies	17
Figure 2-14: The photoelectric effect in the K-shell of an atom	18
Figure 2-15: Compton interaction with an orbital electron.....	19
Figure 2-16: Pair production and annihilation radiation	20
Figure 2-17: Generic NaI(Tl) scintillator and PM tube	22
Figure 2-18: Organic scintillator excitation levels.....	23
Figure 2-19: Inorganic valence and conduction bands with activator impurity	24
Figure 2-20: Components of a generic PM tube	25
Figure 2-21: High-energy beta particle interacting in two layers of a phoswich and the recorded electrical pulse	27

LIST OF FIGURES (Continued)

<u>Figure</u>	<u>Page</u>
Figure 2-22: Diagram of digital signal processing steps.....	29
Figure 2-23: Multiple digital signal processors, configured in parallel	30
Figure 2-24: Measurement of electrical baseline, peak amplitude, and relative decays M1 and M2	31
Figure 2-25: Area measurements A and B, to assess deposited energy by layer	31
Figure 3-1: Layers of the studied phoswich detector	33
Figure 3-2: Photograph of the studied phoswich in its final state.....	33
Figure 3-3: Shielding configuration during testing phase, the black cloth would be moved over the phoswich window while taking measurements	35
Figure 3-4: Pulse recorded from beta particle interaction in the BC400 layer	38
Figure 3-5: Pulse recorded from gamma-ray interaction in the NaI(Tl) layer	39
Figure 3-6: Pulse recorded from beta particle interaction in the BC400 and CaF ₂ (Eu) layers.....	40
Figure 3-7: 2D histogram of FCR and SCR values from 65,000 pulses collected from an unshielded ¹³⁷ Cs source	40
Figure 3-8: The effect of offset and gain settings on pulses collected from a beta-particle shielded ⁶⁰ Co source	41
Figure 3-9: Validated and invalidated pulses per threshold setting.....	42
Figure 3-10: Average energy of validated and invalidated pulses per threshold setting	43
Figure 3-11: Ringing effect observed by Farsoni et al. (2009)	44
Figure 3-12: Relaxation correction effect on FCR/SCR data set	44
Figure 3-13: Outlined interaction regions of a 2D FCR/SCR histogram from an unshielded ¹³⁷ Cs source.....	45
Figure 3-14: Relaxation corrected 2D FCR/SCR histogram from unshielded ¹³⁷ Cs	46
Figure 3-15: Relaxation corrected 2D FCR/SCR histogram from unshielded ¹³⁷ Cs with NaI(Tl) region selected.....	47

LIST OF FIGURES (Continued)

<u>Figure</u>	<u>Page</u>
Figure 3-16: Relaxation corrected 2D FCR/SCR histogram from unshielded ^{137}Cs with BC400 and $\text{CaF}_2(\text{Eu})$ regions selected.....	47
Figure 3-17: Beta particle and gamma-ray filter samples 1, 10, and 11.....	50
Figure 3-18: Solid angle relative to a point source and detector window.....	51
Figure 3-19: Representation of a full-energy-peak resolution calculation	53
Figure 4-1: Gamma-ray and x-ray spectrum from ^{133}Ba	61
Figure 4-2: Gamma-ray spectrum from ^{24}Na and ^{38}Cl	61
Figure 5-1, Photon spectrum and pulse discrimination level for a beta particle shielded $1.5\text{E}-4$ μCi ^{57}Co button source.....	65
Figure 5-2, Photon spectrum and pulse discrimination level for a beta particle shielded 0.405 μCi ^{133}Ba button source.....	65
Figure 5-3, Photon spectrum and pulse discrimination level for a beta particle shielded 0.855 μCi ^{137}Cs button source	66
Figure 5-4, Photon spectrum and pulse discrimination level for a beta particle shielded 0.78 μCi ^{60}Co button source	66
Figure 5-5, Electron spectrum and pulse discrimination level for a 10 μCi ^{14}C foil source.....	66
Figure 5-6, Electron spectrum and pulse discrimination level for a 0.0188 μCi ^{36}Cl foil source....	67
Figure 5-7, Electron spectrum and pulse discrimination level for a 0.0164 μCi $^{90}\text{Sr}/^{90}\text{Y}$ foil source	67
Figure 5-8, Gamma-ray and beta particle spectra and pulse discrimination level from a mixed radiation field consisting of 0.13 μCi ^{137}Cs , 0.02 μCi ^{14}C and 0.018 μCi $^{90}\text{Sr}/^{90}\text{Y}$ from a filter paper source (Sample 1)	68
Figure 5-9, Gamma-ray and beta particle spectra and pulse discrimination level from a mixed radiation field consisting of 0.077 μCi ^{137}Cs and 0.018 μCi $^{90}\text{Sr}/^{90}\text{Y}$ from a filter paper source (Sample 10)	68
Figure 5-10, Gamma-ray and beta particle spectra and pulse discrimination level from a mixed radiation field consisting of 0.077 μCi ^{137}Cs and 0.048 μCi ^{14}C from a filter paper source (Sample 11)	69

LIST OF FIGURES (Continued)

<u>Figure</u>	<u>Page</u>
Figure 5-11: m number effect on the maximum number of counts.....	72
Figure 5-12: Measured and simulated full-energy-peak efficiencies in NaI(Tl) for ^{57}Co (122 keV), ^{133}Ba (356 keV), ^{137}Cs (662 keV), and ^{60}Co (1173 and 1332 keV)	73
Figure 5-13: Measured efficiencies in BC400 + $\text{CaF}_2(\text{Eu})$ layers for ^{14}C (156 keV), ^{36}Cl (709 keV), and $^{90}\text{Sr}/^{90}\text{Y}$ (2280 keV)	74
Figure 5-14: Measured intrinsic efficiencies for beta particles in BC400 + $\text{CaF}_2(\text{Eu})$ layers for ^{14}C (156 keV) and $^{90}\text{Sr}/^{90}\text{Y}$ (2280 keV) and intrinsic full-energy-peak efficiency for gamma-rays in NaI(Tl) for ^{137}Cs (662 keV)	75
Figure 5-15: Measured intrinsic full-energy-peak efficiencies in the NaI(Tl) layer for ^{137}Cs (662 keV), ^{60}Co (1173 keV), and ^{60}Co (1332 keV) with varying incident count rate	76
Figure 5-16: Measured intrinsic full-energy-peak efficiencies in the NaI(Tl) layer with varying distance between source and phoswich window	77
Figure 5-17: Measured absolute full-energy-peak efficiencies in the NaI(Tl) layer with varying distance between source and detector window	77
Figure 5-18: Measured beta particle intrinsic efficiencies in BC400 + $\text{CaF}_2(\text{Eu})$ layers with varying incident count rate on the phoswich window	78
Figure 5-19: Measured intrinsic efficiencies in BC400 + $\text{CaF}_2(\text{Eu})$ layers with varying distance between source and phoswich window	79
Figure 5-20: Measured absolute efficiencies in BC400 + $\text{CaF}_2(\text{Eu})$ layers with varying distance between source and phoswich window	79
Figure 5-21: Measured intrinsic full-energy-peak efficiency in the NaI(Tl) layer for ^{137}Cs (662 keV) with varying incident count rate, in a mixed beta particle/gamma-ray radiation field	80
Figure 5-22: Measured beta particle intrinsic efficiencies in BC400 + $\text{CaF}_2(\text{Eu})$ layers with varying incident count rate, in a mixed beta particle/gamma-ray radiation field	81
Figure 5-23: Measured beta particle intrinsic efficiencies in BC400 + $\text{CaF}_2(\text{Eu})$ layers and gamma-ray intrinsic full-energy-peak efficiency in the NaI(Tl) layer with varying distance between source and phoswich window, in a mixed beta particle/gamma-ray radiation field	81
Figure 5-24: Resolution of a 2.54 cm x 2.54 cm NaI(Tl) crystal.....	83
Figure 5-25: Measured full-energy-peak resolution in the NaI(Tl) layer from ^{57}Co (122 keV), ^{133}Ba (356 keV), ^{137}Cs (662 keV), and ^{60}Co (1173 and 1332 keV) sealed button sources.....	84

LIST OF FIGURES (Continued)

<u>Figure</u>	<u>Page</u>
Figure 5-26: Absolute and relative standard deviation of the FWHM with varying bin number ..	85
Figure 5-27: Minimum number of bins within the FWHM to maintain a FWHM standard deviation $\leq 5\%$ relative to the number of counts contained in the full-energy-peak	85
Figure 5-28: ^{57}Co spectrum	86
Figure 5-29: Background spectrum collected over 2579 seconds	87
Figure 9-1: FCR/SCR 2D histogram for an unshielded ^{137}Cs source; $f_a = 10, f_b = 60, f_c = 200$	101
Figure 9-2: FCR/SCR 2D histogram for an unshielded ^{137}Cs source; $f_a = 10, f_b = 60, f_c = 600$	101
Figure 9-3: FCR/SCR 2D histogram for an unshielded ^{137}Cs source; $f_a = 10, f_b = 60, f_c = 1000$	102
Figure 9-4: FCR/SCR 2D histogram for an unshielded ^{137}Cs source; $f_a = 5, f_b = 60, f_c = 800$	102
Figure 9-5: FCR/SCR 2D histogram for an unshielded ^{137}Cs source; $f_a = 10, f_b = 60, f_c = 800$	103
Figure 9-6: FCR/SCR 2D histogram for an unshielded ^{137}Cs source; $f_a = 20, f_b = 60, f_c = 800$	103

LIST OF TABLES

<u>Table</u>	<u>Page</u>
Table 3-1: Physical properties of scintillation material used in the studied phoswich	32
Table 3-2: Probability of 1 MeV beta particle or gamma-ray interaction.....	34
Table 3-3: Interaction type and region as defined from the 2D FCR/SCR histogram	45
Table 3-4: Experimentally determined FCR and SCR regions	46
Table 3-5: Radioactive sources used, activity at time of measurement, target emission type, and energy	49
Table 4-1: Absolute and intrinsic full-energy-peak efficiencies for gamma-ray interaction in the NaI(Tl) layer	56
Table 4-2: Absolute and intrinsic efficiencies for beta particle interactions in BC400 + CaF ₂ (Eu) layers.....	56
Table 4-3: Absolute and intrinsic efficiencies for beta particles in BC400 + CaF ₂ (Eu) layers from ¹⁴ C (156 keV), ¹³⁷ Cs (514 keV), and ⁹⁰ Sr/ ⁹⁰ Y (2280 keV) and absolute and intrinsic full-energy-peak efficiencies for gamma-rays in NaI(Tl) from ¹³⁷ Cs (662 keV).....	57
Table 4-4: Absolute and intrinsic full-energy-peak efficiencies with varying distance from the phoswich window from a beta particle shielded 0.855 μCi ¹³⁷ Cs (662 keV) button source	57
Table 4-5: Absolute and intrinsic full-energy-peak efficiencies with varying distance from the phoswich window from a beta particle shielded 0.78 μCi ⁶⁰ Co (1173 keV) button source	58
Table 4-6: Absolute and intrinsic full-energy-peak efficiencies with varying distance from the phoswich window from a beta particle shielded 0.78 μCi ⁶⁰ Co (1332 keV) button source	58
Table 4-7: Absolute and intrinsic efficiencies with varying distance from the phoswich window from a 10 μCi ¹⁴ C (156 keV) foil source	58
Table 4-8: Absolute and intrinsic efficiencies with varying distance from the phoswich window from a 0.0188 μCi ³⁶ Cl (708 keV) foil source	59
Table 4-9: Absolute and intrinsic efficiencies with varying distance from the phoswich window from a 0.0164 μCi ⁹⁰ Sr/ ⁹⁰ Y (2280 keV) foil source.....	59
Table 4-10: Absolute and intrinsic full-energy-peak efficiencies for the NaI(Tl) layer, and absolute and intrinsic efficiencies for BC400 + CaF ₂ (Eu) layers from a combined activity of 0.33 μCi (0.13 μCi ¹³⁷ Cs, 0.02 μCi ¹⁴ C, 0.018 μCi ⁹⁰ Sr/ ⁹⁰ Y) from filter paper source (Sample 1)	59

LIST OF TABLES

<u>Table</u>	<u>Page</u>
Table 4-11: Absolute and intrinsic full-energy-peak efficiencies for the NaI(Tl), and absolute and intrinsic efficiencies for BC400 + CaF ₂ (Eu) layers from a combined activity of 0.095 μ Ci (0.077 μ Ci ¹³⁷ Cs, 0.018 μ Ci ⁹⁰ Sr/ ⁹⁰ Y) from filter paper source (Sample 10)	60
Table 4-12: Absolute and intrinsic full-energy-peak efficiencies for the NaI(Tl), and absolute and intrinsic efficiencies for BC400 + CaF ₂ (Eu) from a combined activity of 0.125 μ Ci (0.077 μ Ci ¹³⁷ Cs, 0.048 μ Ci ¹⁴ C) from filter paper source (Sample 11).....	60
Table 4-13: Gamma-ray resolution in the NaI(Tl) layer by energy	62
Table 4-14: Minimum Detectable Activity around specified regions of interest.....	63
Table 4-15: Theoretical and measured pulse discrimination time	63
Table 4-16: Maximum detection system initialization time	64

Prototyping a Triple-Layer Phoswich Detection System

1 Introduction

1.1 Overview

Multi-layer scintillation based radiation detectors, commonly referred to as phoswich detectors, have rapidly evolved in recent years. These detection systems may be tailored by design to simultaneously detect alpha particle, beta particle, and gamma-ray radiation fields by virtue of the properties inherent to each scintillation layer (Hennig et al. 2007, Farsoni et al. 2006, Celis et al. 2007, Farsoni et al. 2008, 2010a). Digital signal processing has improved radiation discrimination accuracy and enhanced reliability, while reducing complexity and size of traditional analog signal processing techniques (Grzywacz 2003, Miller et al. 2005, Farsoni et al. 2008).

The flexibility and capabilities of these new digital phoswich radiation detection systems continues to mature. There is a continuing need for more accurate portal monitoring survey equipment, dose measurement systems, and environmental remediation equipment (Kouzes 2005). Oregon State University has recently been awarded a patent for a new variant phoswich scintillator and digital pulse processor (DPP), that when coupled produce a fast and highly accurate dual beta particle and gamma-ray detection system (Farsoni et al. 2007a, 2007b, 2008).

First generation production models of this phoswich system are already on order. Prior to delivery to end-users, the operating parameters and characteristics need to be fully evaluated and documented. Future generations will become viable replacements for industry's current radiation and dosimetry measurement systems.

1.2 Objective and Intent

The objective of this work is to classify operational characteristics and behavior of this latest generator phoswich detector and digital pulse processing system. The intent is to help usher this detection system from specialty applications into a broad based commercial replacement for antiquated systems currently found in the nuclear industry.

2 Literature Review

2.1 Radioactive Transformations

An atom is the basic form of matter from which all substances come into being (Ponomarev 1993). The Rutherford-Bohr model describes an atom as being comprised of a central positively charged nucleus surrounded by an electron cloud (Krane 1996). Simplistically, an atom's nucleus contains protons and neutrons (Turner 2007). The number of protons and neutrons determines the nuclide and its physical properties. Both the nucleus and electron cloud are arranged in very specific configurations based on energy and other parameters (Navratil 2003). These configurations are often modeled as shells surrounding the center of the atom. Events that involve changes to the configuration of the electron cloud are referred to as atomic transitions. Likewise, events that involve changes to the configuration of the nucleus are referred to as nuclear transformations (Martin 2006). Figures 2-1 and 2-2 illustrate atomic and nuclear shells (Navratil 2003)

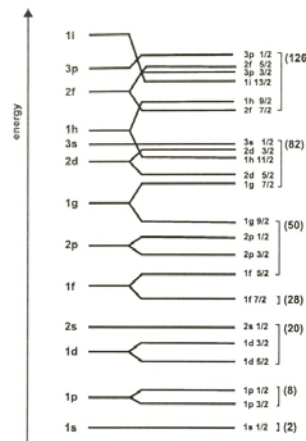


Figure 2-1: Orbital electron shell configuration (taken from Navratil 2003)

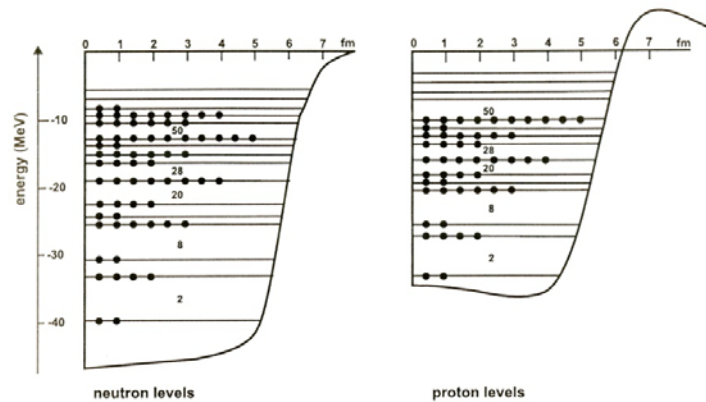


Figure 2-2: Nuclear shell configuration (taken from Navratil 2003)

Atoms generally prefer to reside in their most stable and consequently lowest energy configurations. However, they are often formed or excited into higher energy states in which their atomic or nuclear configurations do not represent the lowest possible rest energy. It is in these situations that atoms undergo a variety of atomic transitions and nuclear transformations which relieve that excess energy.

The nucleus contains positively charged particles (protons) in a very small space. Neutral particles (neutrons) act as buffers and oppose the Coulomb repulsion generated within the nucleus (Martin 2006). This relationship is not merely linear. As the number of protons increases, exceedingly more neutrons are required to mitigate the Coulomb repulsion (Martin 2006). For this reason nuclear transformations occur in the following three scenarios: there are an excessive number of protons; there are an excessive number of neutrons; or the inherent size of the nucleus is so large that it cannot maintain itself and fragments. Figure 2-3 depicts the stability of nuclides with varying number of protons and neutrons (Navratil 2003).

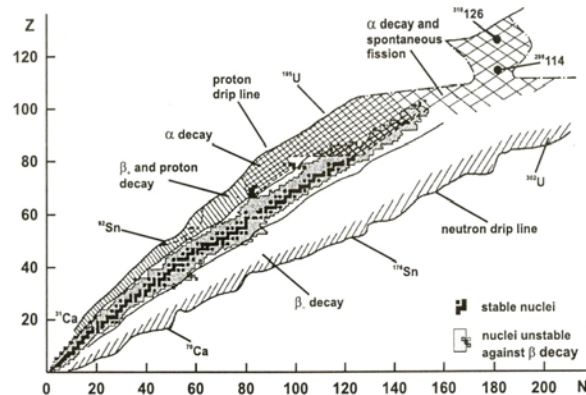


Figure 2-3: Nuclide stability chart (taken from Navratil 2003)

Nuclear transformations often incorporate atomic transition as part of the overall decay mechanism and are commonly referred to as radioactive decay. There are specific mechanisms and permutations to radioactive decay that will be discussed in the following sections.

2.2 Isobaric Transformations

Nuclei with excess protons or neutrons may undergo beta transformation to obtain a lower energy state. Beta transformations may be explained through the weak nuclear force. Subatomic physics describes protons and neutrons as each consisting of three quarks. A neutron consists of one u quark and two d quarks (u d d), while a proton consists of a u quark, a d quark, and another u quark (u d u) (Navratil 2003). The weak force describes a process in which a neutron transforms into a proton and vice versa. This is achieved by converting a d quark into a u quark or conversely a u quark into a d quark by means of exchanging the massive virtual particles W^- and W^+ .

This process is not as straight forward as it may appear. Each flavor of quark has a unique set of subatomic properties, which must be conserved during a transformation. As a result, transformations of proton rich nuclei are dissimilar to transformations of neutron rich nuclei.

2.2.1 Negatron (β^-) Transformation

Nuclei that are rich in neutrons may undergo negatron transformation. In this process a neutron is converted into a proton, a fast electron (beta particle or β^-), and an antineutrino. The beta particle and antineutrino are created and do not exist prior to the transformation (Krane 1996). These two particles are emitted from the nucleus to conserve charge, energy, and subatomic properties (Navratil 2003). The process may be modeled by,

$$n \rightarrow p + e^- + \bar{\nu}_e \quad (2.1)$$

where n is a neutron, p a proton, e^- a fast electron and $\bar{\nu}_e$ represents the antineutrino. Figure 2-4 depicts negatron transformation.

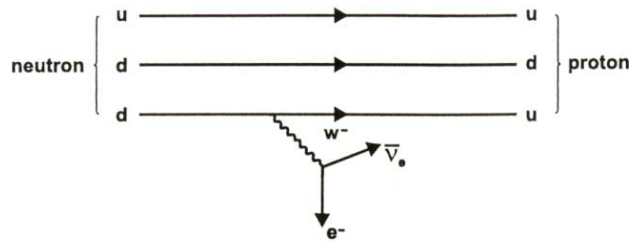


Figure 2-4: Conversion of a d quark into a u quark (taken from Navratil 2003)

In negatron transformation the rest energy of the parent is always greater than that of the progeny and emitted particles (Krane 1996). Excess rest energy is referred to as the Q value. The following equation describes the complete negatron transformation,

$${}^A_Z X \xrightarrow{\beta^-} {}^A_{Z+1} Y + {}^0_{-1} e^- + \bar{\nu}_e + Q \quad (2.2)$$

where the progeny nucleon number (A) remains unchanged while the proton number (Z) increases by one.

Antineutrinos are virtually mass less and are relatively difficult to detect (Turner 2007). However, beta particles are easy to detect as they carry a negative charge and interact with any

material. The energy liberated from a negatron transformation is imparted arbitrarily between the recoil progeny nucleus (negligible), beta particle, and antineutrino, providing a continuous beta particle energy spectrum. The energy imparted to the beta particle and antineutrino may be approximated by:

$$Q \cong E_{\bar{\nu}_e} + E_{\beta^-} \quad (2.3)$$

When the antineutrino receives zero Q value energy, the beta particle is at its maximum energy ($E_{\beta_{\max}}$). Few beta particles receive the maximum energy liberated during the transformation. A reasonable approximate average beta particle energy is found to be $1/3 E_{\beta_{\max}}$ (Martin 2006). Figure 2-5 below illustrates the beta particle spectrum for ^{14}C (Martin 2006).

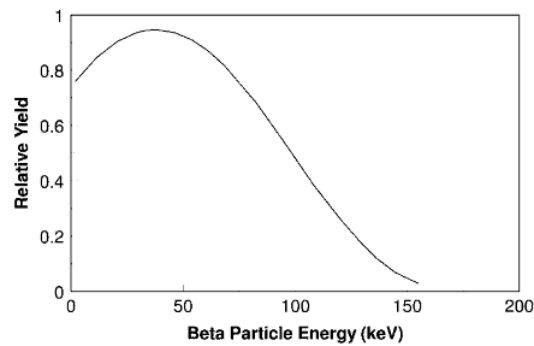


Figure 2-5: Beta particle spectrum from ^{14}C (take from Martin 2006)

2.2.2 Negatron (β^-) Interactions

Since beta particles are electrons, they have the same mass and charge as orbital electrons, and as a consequence, suffer a tortuous path through absorbing materials (Knoll 2000). Beta particles interact with material and lose kinetic energy by two mechanisms: collisions and radiative loss. The rate at which energy loss occurs differs by absorbing material and is referred to as linear stopping power (S) or specific energy loss. Linear stopping power is defined as the differential energy loss over a corresponding differential path length and is solved for by,

$$S = -\frac{dE}{dx} = -\left(\frac{dE}{dx}\right)_c - \left(\frac{dE}{dx}\right)_r \quad (2.4)$$

where c represents collisional loss and r represents radiative loss (Knoll 2000). An approximate ratio between collisional and radiative energy loss may be solved by,

$$\left(\frac{dE}{dx}\right)_r / \left(\frac{dE}{dx}\right)_c \cong \frac{EZ}{700} \quad (2.5)$$

where E is the energy of the beta particle and Z is the atomic number of the absorbing material (Knoll 2000).

Collisional loss occurs when a beta particle dislodges orbital electrons, ionizing the material (Martin 2006). Delta rays are a by-product of collisional interactions where the dislodged electron carries enough energy to ionize other atoms in the material (Martin 2006). Higher energy orbital electrons fill these vacancies, generating additional electromagnetic radiation which will be discussed in section 2.5.

Collisional loss may be described by,

$$-\left(\frac{dE}{dx}\right)_c = \frac{2\pi e^4 NZ}{m_o v^2} \left(\ln \left(\frac{m_o v^2 E}{2I^2 (1 - \beta^2)} \right) - \ln(2) \left(2\sqrt{1 - \beta^2} - 1 + \beta^2 \right) + (1 - \beta^2) + 1/8 \left(1 - \sqrt{1 - \beta^2} \right)^2 \right) \quad (2.6)$$

where v and e are the velocity and charge of the beta particle, N , Z , and I are the density, atomic number, and average excitation/ionization potential of the absorbing material, m_o is the rest energy of an electron and β is equal to v/c (Knoll 2000).

Radiative loss occurs as the beta particle's path is curved by other charged components of the material due to the Coulomb force (Knoll 2000). The curve represents acceleration and to conserve energy, the beta particle emits electromagnetic radiation. Radiative loss may be described by:

$$-\left(\frac{dE}{dx}\right)_r = \frac{NEZ(Z+1)e^4}{137(m_0c^2)^2} \left(4\ln\left(\frac{2E}{m_0c^2}\right) - 4/3 \right) \quad (2.7)$$

Bremsstrahlung, or braking radiation, is this electromagnetic radiation emitted by the beta particle to compensate for the acceleration caused by nuclei acting on the beta particle in the absorbing material (Martin 2006). Figure 2-6 illustrates the Bremsstrahlung phenomena (Martin 2006).

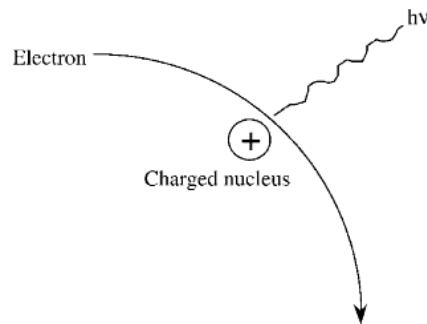


Figure 2-6: Curved path of an electron, producing electromagnetic radiation to conserve energy (taken from Martin 2006)

Cerenkov radiation occurs when bremsstrahlung produced electromagnetic radiation cannot keep up with the beta particle from which it was produced. More electromagnetic radiation is produced and the two sets constructively interfere with each other to produce visible blue photons (Fig. 2-7, Martin 2006).

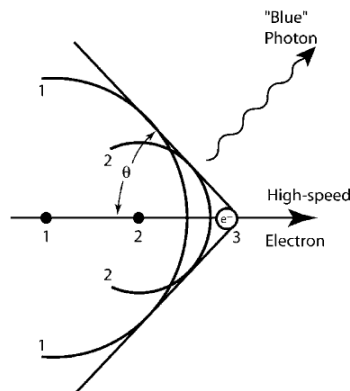


Figure 2-7: Constructive interference producing Cerenkov radiation (taken from Martin 2006)

2.2.3 Positron (β^+) Transformation

Nuclei that are rich in protons may undergo positron transformation, which may appear as a mirror image of negatron transformation. A proton may be converted into a neutron, positron (inverse electron or β^+), and a neutrino. Like negatron transformation, the positron and neutrino conserve charge, mass, and subatomic properties. The transformation may be modeled with the following equation,

$$p \rightarrow n + e^+ + \nu_e \quad (2.8)$$

where e^+ represents a positron and ν_e a neutrino.

The weak force still provides the mechanisms that enables a proton to transition into a neutron and ultimately produce a lower energy nuclear configuration. Positron transformations are described by the following equation,

$${}^A_Z X \xrightarrow{\beta^+} {}^A_{Z-1} Y + {}^0_{+1} e^+ + \nu_e + Q + e^-_{orb} \quad (2.9)$$

where the progeny nucleon number remains unchanged while the proton number decreases by one. The orbital electron is released from the system as the number of protons has decreased.

Like negatron transformation, the positron and neutrino arbitrarily split any excess Q value energy and a continuous distribution is observed. Unlike negatron transformation, the distribution is shifted to the right because there is an additive Coulomb repulsion from the nucleus onto the positron (Martin 2006). Figure 2-8 illustrates the positron spectrum for ${}^{64}\text{Cu}$ (Martin 2006).

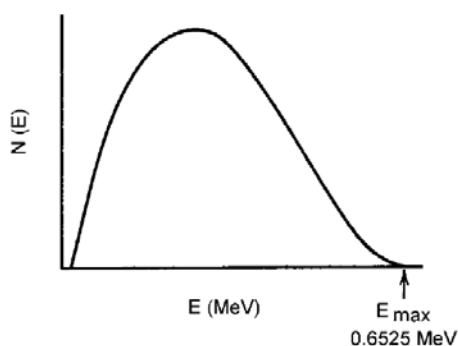


Figure 2-8: Positron energy spectrum for ^{64}Cu (taken from Martin 2006)

However, unlike negatron transformation, the progeny atom and emitted particles have a combined rest energy that is greater than that of the parent. Therefore, the calculated Q value for positron transformation is negative. Furthermore, an orbital electron is also required to balance the charge of the system (Martin 2006). In order for this transformation to occur, protons and neutrons in the nucleus must reorganize themselves into a fundamentally lower energy configuration in order to conserve energy (Martin 2006). At a minimum the parent rest energy must be greater than the progeny rest energy plus two electron masses (1.022 MeV). For this reason positron transformation is never observed in nature (Krane 1996).

2.2.4 Positron (β^+) Interactions

Like the antineutrino, the neutrino does not interact with matter, and as a result is very difficult to detect (Cember 2007). The positron on the other hand is quite easy to detect. The positron is the antiparticle to the electron (Krane 1996). Positrons with energy above rest energy collide with electrons until they reach an equivalent energy to nearby electrons (Krane 1996). At this point a positron and electron will momentarily form positronium (Martin 2006). This union results in the annihilation of the positronium into pure energy. Two identical photons, each with the rest energy of an electron (0.511 MeV) are created and travel 180° apart from each other (Martin 2006). These photons are easily detected and generate a full-energy-peak at 0.511 MeV, commonly referred to as the annihilation peak. Figure 2-9 illustrates positron and negatron annihilation (Martin 2006).

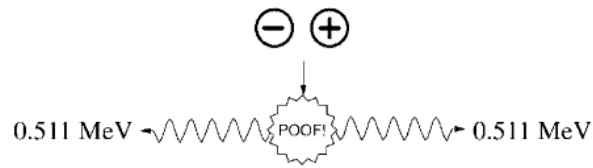


Figure 2-9: Positronium annihilating into two photons of equal energy (taken from Martin 2006)

2.2.5 Electron Capture Transformation

Proton rich nuclei may also undergo electron capture transformation whereby the nucleus converts a proton into a neutron by capturing an inner shell orbital electron (Martin 2006). This process competes with positron transformation (Knoll 2000). Unlike positron transformation, only a neutrino is emitted and carries all excess rest energy (Martin 2006). The process may be modeled with the following equations:

$$p + e^{-} \rightarrow n + \nu_e \quad (2.10)$$

$${}^A_Z X + {}^0_{-1}e_{orb}^{-} \xrightarrow{EC} {}^A_{Z-1} Y + \nu_e \quad (2.11)$$

2.3 Alpha Transformation

Very large unstable nuclei can more quickly reach a stable nuclear configuration by emitting multiple nucleons in a single transformation (Martin 2006). However, such a transformation often competes with other transformations owing to the unstable nature of these nuclei. Inside a large nucleus two protons and two neutrons may exclusively interact with each other, forming an alpha (α) particle (Navratil 2003). Alpha particles are essentially Helium (He) atoms sans electrons and are often described accordingly. Alpha transformation may be modeled by:



The process that enables such a transformation may be explained through quantum mechanics. The alpha particle inside a nucleus effectively decreases the overall rest energy of the nucleus. This seemingly “lost” rest energy is imparted back to the alpha particle, raising its position in the nucleus’ potential well. The alpha particle’s movement inside the nucleus, coupled with the de Broglie wavelength enables it to quantum tunnel through the potential barrier (Martin 2006). The following image (Fig 2-10) illustrates alpha transformation process (Navratil 2003).

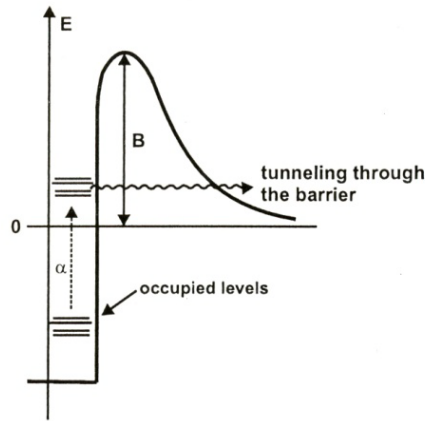


Figure 2-10: Alpha transformation inside a nucleus’ potential well (taken from Navratil 2003)

The Q value in equation 2.12 represents the decrease in rest energy from the formation of the alpha particle. This energy is divided between the progeny nucleus in recoil kinetic energy, progeny nucleus excitation, and alpha particle kinetic energy (Navratil 2003). As a result, there are discrete alpha particle energies rather than a continuous spectrum as seen in beta transformations. The Q value for alpha transformation may be expressed by the following equation:

$$Q = E_{recoil,Y} + E_{excitation,Y} + E_{\alpha} \quad (2.13)$$

Alpha transformations greatly reduce nuclear instability and as a result there is a significant amount of excess rest energy imparted to the alpha particle. Alpha particles typically have energies greater than 4.5 MeV.

2.3.1 Alpha Interactions

There are three types of alpha particle interactions: collisional; alpha particle transmutation; and α -n reactions. Since alpha particles do not have electrons, they possess a net positive charge and interact with all types of material. When an alpha particle collides with an atom, it imparts enough energy to ionize the atom. The linear stopping power is described by the *Bethe formula*,

$$-\frac{dE}{dx} = \frac{4\pi e^4 z^2}{m_o v^2} NZ \left(\ln \left(\frac{2m_o v^2}{I} \right) - \ln \left(1 - \frac{v^2}{c^2} \right) - \frac{v^2}{c^2} \right) \quad (2.14)$$

where the constants above are the same as described for equation 2.6 above (Knoll 2000). On average, an alpha particle losses 35.5 eV of its energy for every ion pair created (Cember 2009).

An alpha particle will continue to ionize material until all of its kinetic energy is spent. As it slows down, the production rate of ion pairs increase to a maximum known as the Bragg peak (Knoll 2000). At this point the alpha particle has spent the majority of its energy. Figure 2-11 below illustrates alpha particle ion pair production (Cember 2009).

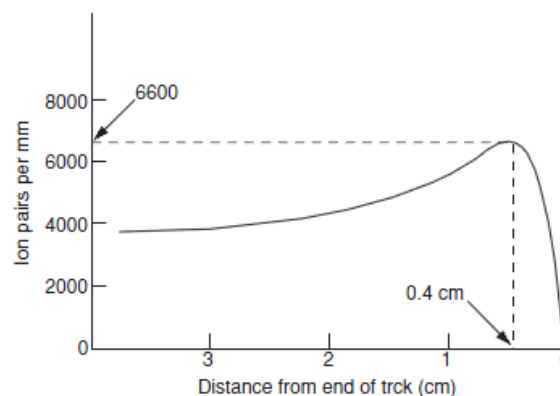
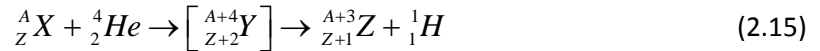


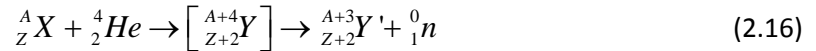
Figure 2-11: Ion production during an Alpha particle track (taken from Cember 2009)

Alpha particle transmutation occurs when an alpha particle collides with a light nucleus, forming a new element. This process was observed by Rutherford for all elements between boron and potassium except for carbon and oxygen (Martin 2006). The progeny of this transmutation is unstable and undergoes an immediate nuclear reorganization, ejecting a proton in the process. Alpha particle transmutation is modeled by,



where Y is the first progeny, Z is the final progeny, and H represents the proton (Hydrogen atom).

Alpha-neutron reactions are similar to alpha transmutations in that an alpha particle collides with a light nucleus producing a new progeny. However, instead of the progeny undergoing transmutation into another element, the progeny emits a neutron and transmutes into a different isotope (Martin 2006). Alpha-neutron reactions are modeled by,



where Y and Y' are isotopes of the same element.

2.4 Isomeric Transitions

Nuclear transformations rarely impart all excess rest energy to emitted particles, leaving the progeny nucleus in an excited state (Navratil 2003). In other words some of the neutrons or protons are in an elevated energy configuration following nuclear transformation. The nucleons will reorganize themselves into a more stable configuration and in order to conserve energy, electromagnetic radiation must be emitted from the nucleus. The strong nuclear force binds the nucleons together and as a consequence, transitions within the nuclear shells produce large changes in rest energy (Navratil 2003). The quantity of energy released during these de-excitations is always discrete, as it is the difference between the nuclear shells illustrated in Figure 2.2 above (Knoll 2003).

2.4.1 Gamma-Rays

Photons are the most common type of de-excitation energy observed (Navratil 2003). Photons that originate within the nucleus due to isometric transition are referred to as gamma-rays (Martin 2006). Isomeric transitions that produce gamma-rays happen after nuclear transformation, which means that technically speaking, gamma-rays belong to the progeny atom. However, de-excitation occurs very quickly after transformation ($10^{-16} - 10^{-4}$ seconds) and it is convention that gamma-rays are said to be associated with the parent rather than progeny atom (Navratil 2003). Gamma-ray energies range from 8 keV (^{169}Er) to many MeV for nuclear reactions. The following illustration (Fig. 2-12) depicts beta transformation followed by gamma-ray emission for the classic nuclide ^{137}Cs (Martin 2006).

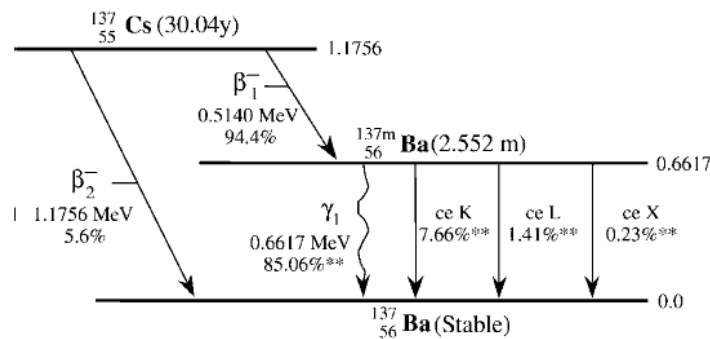


Figure 2-12: ^{137}Cs beta transformation followed by gamma-ray or conversion electron emission from the progeny atom (taken from Martin 2006)

2.4.2 Gamma-Ray Interactions

With respect to detection systems, gamma-rays undergo three primary interactions with material; photoelectric effect; Compton interaction; and pair production (Martin 2006). The probability to observe one interaction over another is dictated by the energy of the gamma-ray and the Z number of the absorbing material (Martin 2006). Figure 2-13 below illustrates the type of interaction expected for lead and water with varying gamma-ray energy (μ or total attenuation coefficient) (Martin 2006).

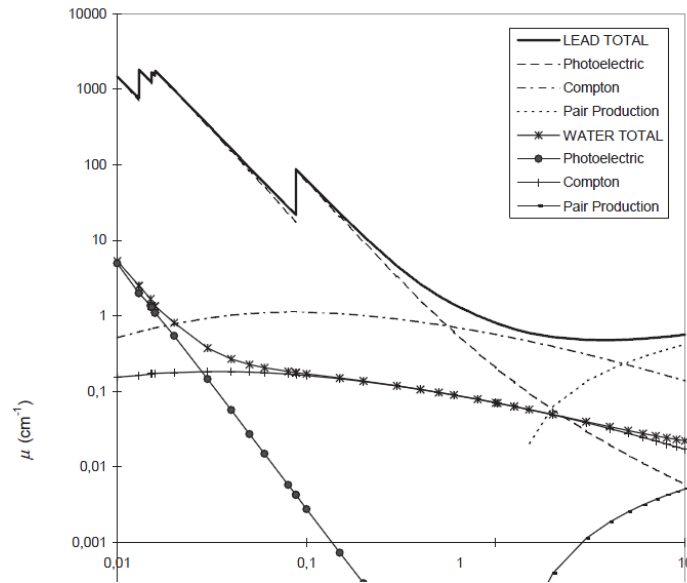


Figure 2-13: Gamma-ray interaction probability with varying gamma-ray energies (taken from Martin 2006)

Photoelectric effect occurs when lower energy gamma-rays interact with an atom and are completely absorbed. The energy of the gamma-ray dislodges an orbital electron which has a resultant energy which may be solved for by,

$$E_{e^-} = h\nu - E_b \quad (2.17)$$

where E_b is the binding energy of the electron to the atom and $h\nu$ is the energy of the gamma-ray. The dislodged orbital electron is referred to as a photoelectron, owing to how it was produced. The kinetic energy of the photoelectron is typically lost to the medium from whence it came (Cember 2009). The probability of photoelectric effect increases with higher Z material and gamma-rays with energies just above E_b (Turner 2007). Figure 2-14 below illustrates the photoelectric effect (Martin 332).

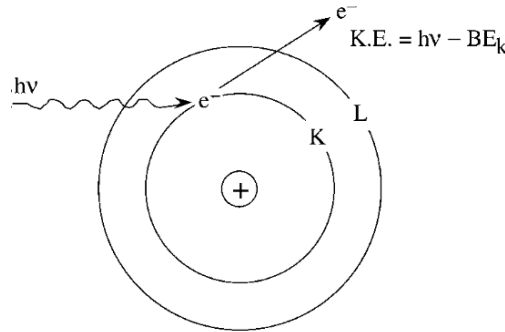


Figure 2-14: The photoelectric effect in the K-shell of an atom (taken from Martin 2006)

Compton interaction is the predominant interaction for typical gamma-ray energies and occurs between a gamma-ray and an electron in a material (Knoll 2000). The gamma-ray collides with the electron relative to an angle ϑ , which causes the gamma-ray to scatter and imparts energy onto the *recoil electron* (Knoll 2000). The energy of the scattered gamma-ray may be determined by,

$$h\nu' = \frac{h\nu}{1 + \frac{h\nu}{m_0c^2}(1 - \cos \vartheta)} \quad (2.18)$$

where m_0c^2 is the rest energy of an electron (0.511 MeV). Equation 2.18 shows that when $\vartheta = 0$, no scatter occurs and when $\vartheta = \pi$, maximum scatter occurs. Compton interaction plays a significant role in gamma-ray detection as the discrete energies expected from isomeric transition are skewed by this scattering. The probability of Compton scattering increases linearly with the absorbing material's Z number (Knoll 2000). Figure 2-15 below illustrates Compton interaction (Martin 2006).

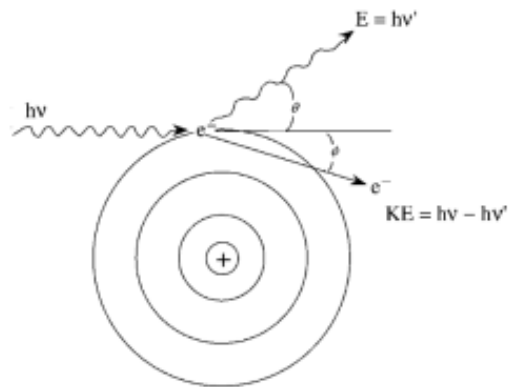


Figure 2-15: Compton interaction with an orbital electron (taken from Martin 2006)

Pair production occurs only with higher energy gamma-rays (≥ 1.022 MeV). An electron and a positron may be created from a gamma-ray which interacts with a strong electromagnetic field as postulated in Einstein's special theory of relativity (Cember 2009). The energy criteria of the gamma-ray is equivalent to the rest energies of the electron and positron (0.511 MeV apiece). Gamma-ray energy above the criteria is unevenly split between the electron and positron due to Coulomb attraction and repulsion with the nucleus (Martin 2006).

Eventually both particles will lose their kinetic energy through collisional losses. The electron becomes a free electron while the positron will undergo annihilation process outlined in positron transformation above (section 2.2.4). The probability of pair production increases with increasing gamma-ray energy and absorbing material Z number (Turner 2007). Figure 2-16 below illustrates pair production (Martin 2006).

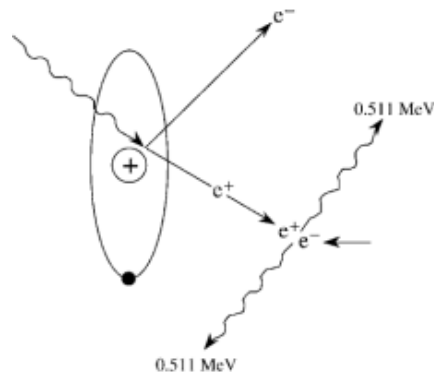


Figure 2-16: Pair production and annihilation radiation (taken from Martin 2006)

2.4.3 Internal Conversion

An alternate method of isometric transition is internal conversion. There is some probability that the wave function of an inner-shell orbital electron and the wave function of its associated nucleus overlap. In this instance, an excited nucleus may impart excess energy onto the overlapping electron. In some nuclear transformation scenarios, there is no possibility that gamma-ray emission can occur owing to an identical spin state between the excited progeny nucleus and ground state progeny nucleus (Navratil 2003). The nucleus can only impart excess rest energy to one of its orbital electrons (generally K or L shell). These affected electrons are commonly referred to as conversion electrons. The conversion electron is dislodged from its orbit with kinetic energy equal to the difference between the imparted energy and binding energy. Unlike beta particles, conversion electrons are monoenergetic as there are no antineutrinos included in the process.

2.5 Atomic Transitions

Atomic transitions typically involve less energy than nuclear transitions as their binding energies are much lower than the strong force felt inside the nucleus (Martin 2006). There are two primary transitions which occur in tandem; dislodgement of an electron from its shell and, as a consequence, the emission of electromagnetic radiation as the vacancy is filled. As

described in the above transitions, an electron may be dislodged from its orbital only when energy imparted to the electron exceeds its binding energy. Electrons that spend more time near the nucleus (K and L inner shells) are the most likely to be dislodged.

A dislodged electron leaves a vacancy which will be filled by an electron in a higher (less stable) orbital. Electromagnetic radiation generally in the form of a photon must be emitted to conserve energy as the atomic structure reorganizes into the more stable configuration. Photons that are created as a result are referred to as characteristic x-rays and carry energies that range between 1keV to 300 keV.

Auger electrons can be emitted by an atom in place of x-rays. This occurs when an x-ray produced from an inner shell is absorbed by another orbital electron while attempting to exit the electron cloud. The electron may then be dislodged if the x-ray carried more energy than the electron's binding energy.

2.6 Scintillation Detection Systems

Scintillation detectors represent the most commonly used ionizing radiation detectors in the world (Knoll 2000). They are comprised of a variety of materials, each with unique design based on the target radiation. The detectors can be shaped and customized for each specific application. They are inexpensive spectroscopy devices and many do not require enhanced cooling systems. For these reasons scintillation detectors are found throughout industry, research, and health care.

The basic process by which they operate is fairly simple, ionizing radiation produces light proportional to the energy deposited within the scintillator. The photons travel through the scintillating material and are incident upon a photomultiplier (PM) tube, where they are converted into photoelectrons, the photoelectrons are multiplied, and finally collected at an anode. Because scintillators exhibit light proportionality, the

detectors can be used to count and quantify the incident radiation. The following image (Fig 2-17) illustrates a generic sodium iodide scintillation detector and PM tube.

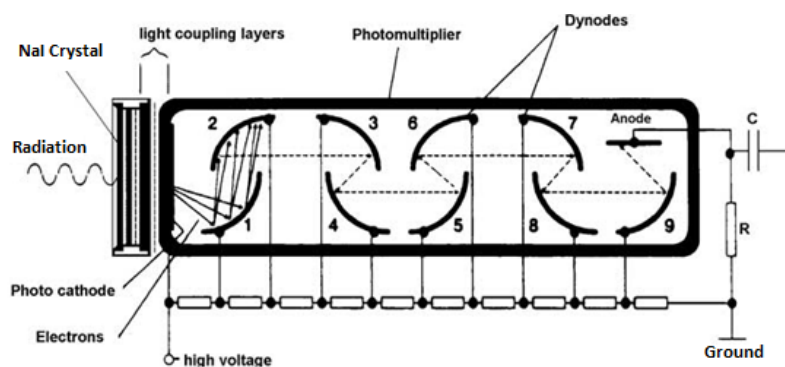


Figure 2-17: Generic NaI(Tl) scintillator and PM tube

2.6.1 Scintillation Physics

A scintillator absorbs incident radiation, which in turn excites its electrons into higher bound energy states. The electrons de-excite back to their ground states and emit photons to conserve energy. Scintillators are classified as *organic* or *inorganic* based on the material from which they are made. Organic and inorganic materials have different electron configurations, resulting in different excitation and de-excitation processes. Scintillation efficiency is the fraction of all incident absorbed energy which is converted into light (Knoll 2000). The rate at which de-excitation occurs for a scintillator is commonly referred to as the light-decay constant. Both of these properties vary by type of scintillator and are provided by the manufacturer.

Organic scintillators are based on organic molecules that possess a π -electron structure (Knoll 2000). This structure provides multiple bound electron states per molecule, each separated by 3-4 eV. In general, the net effect of excitation produces a population of molecules with a single excited energy level (Singlet level 10 or S_{10}) (Knoll 2000). Prompt fluorescence, which is the desired form of scintillation light, is produced by de-excitation from S_{10} to the

ground state and only takes a few nanoseconds (Knoll 2000). The time response may be characterized by,

$$I = I_o \left(e^{-t/\tau_1} - e^{-t/\tau_2} \right) \quad (2.19)$$

where τ_1 depicts the light decay constant and τ_2 depicts the electron excitation time constant (Knoll 2000).

Organic scintillation efficiency suffers due to increased excitation that produces vibrations or heat rather than S_{10} excitation. Additionally, organic scintillators do not possess high-Z material, limiting the photoelectric effect. As a result organic scintillators have virtually no response to high energy photons. Figure 2-18 below illustrates the electron states found in organic scintillators (Knoll 2000).

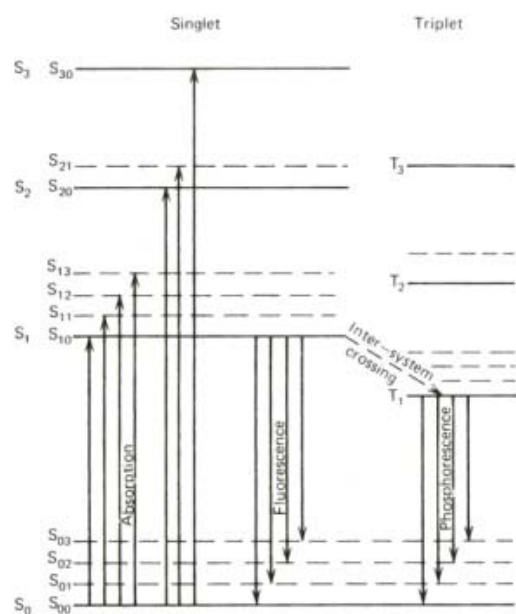


Figure 2-18: Organic scintillator excitation levels (taken from Knoll 2000)

Inorganic scintillators are most often formed as a crystal lattice, placing electrons into discrete energy bands (Knoll 2000). Absorbed energy may elevate an electron from its ground state (valence band) into a mobile excited state (conduction band). In this process a 'hole' is

created in the valence band where the electron previously resided. Impurities added uniformly to the crystal lattice decrease the energy difference between the valence and conduction bands (band gap). Electrons and holes migrate to these impurities where the probability of de-excitation is greater (Knoll 2000). Inorganic scintillators have a range of light-decay constants and light yields and these values are provided by the crystal manufacturer or other literature (Knoll 2000).

The impurity sites are commonly referred to as activators, since the majority of photons produced in a scintillator originate there (Knoll 2000). The impurities also serve to shift the energy of the de-excitation photons. If de-excitation occurs outside of an activation site, the energy of the photon is equal to the energy required to raise an electron from its valence band into the conduction band. The result is that this photon may never escape the scintillator as it continually gets reabsorbed and re-emitted. De-excitation at activator sites produces photons of lower energy since the impurity decreases the band gap, preventing re-absorbance. Figure 2-19 below illustrates the valence and conduction bands along with the shift in band gap due to activator sites (Knoll 2000).

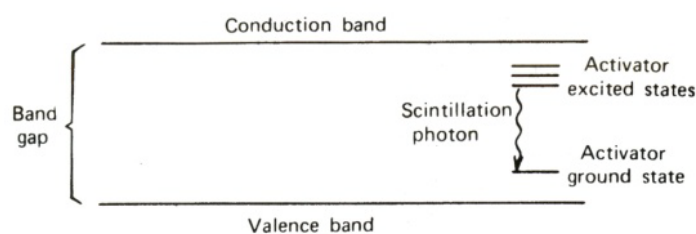


Figure 2-19: Inorganic valence and conduction bands with activator impurity (taken from Knoll 2000)

2.6.2 Photomultiplier Tube

A photomultiplier (PM) tube converts photons into electrons (referred to as photoelectrons) and then multiplies the number of photoelectrons, enhancing the electrical signal. This process is vitally important with scintillation detectors since only a few hundred scintillation photons

may be produced per event (Knoll 2000). The PM tube operates with a few basic steps; first photons incident upon the photoemissive material are absorbed and converted into photoelectrons, next the photoelectrons migrate into the photocathode and are focused and accelerated, next the photoelectrons impinge upon a series of electron multiplying dynodes, finally the electrons are collected at an anode (Knoll 2000). Figure 2-20 below illustrates the functional components of a PM tube (Knoll 2000).

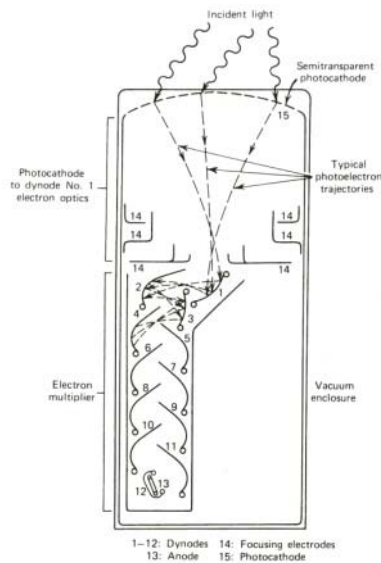


Figure 2-20: Components of a generic PM tube (taken from Knoll 2000)

The voltage pulse generated by a PM tube is produced between 20 – 80 nanoseconds following a scintillation event (Knoll 2000). The shape of the voltage pulse varies with the anode circuitry built into the PM tube. Two cases exist with respect to scintillation based detection systems. The first case occurs when the anode time constant is made much larger than the scintillator's light-decay constant. The voltage response may be idealized by,

$$V(t) \cong \frac{Q}{C} (e^{-\theta t} - e^{-\lambda t}) \quad (2.20)$$

where θ is the reciprocal of the anode time constant ($1/RC$) and λ is the scintillator light decay constant (Knoll 2000). This circuitry is best suited when pulse height information is paramount rather than pulse shape or count rate.

The second case occurs when the anode time constant is made much smaller than the scintillator light-decay constant. In this scenario the voltage response may be idealized by:

$$V(t) \cong \frac{\lambda}{\theta} \frac{Q}{C} (e^{-\lambda t} - e^{-\theta t}) \quad (2.21)$$

This circuitry is best suited when pulse shape is paramount as the anode pulse shape will closely match that generated by the PM tube.

The current generation of phoswich detectors relies on PM tubes. However, future models will most likely utilize multi-pixel photon counters (MPPC) as they do not have the operating constraints and problems (high voltage requirement, temperature sensitivity, delicate, spurious pulses, gain shift) found with PM tubes (Yamamoto et al. 2006; Knoll 2000).

2.6.3 Phoswich Principles

Multiple scintillating layers may be optically coupled to a single PM tube, creating a phoswich detector. Phoswich detectors may be built for specific detection application by understanding of how each scintillating layer interacts with different forms of radiation. The chemical composition of a scintillating material may make absorption of radiation very likely or unlikely. As noted in section 2.6.1, organic scintillators typically are low-Z material and as a consequence, interaction with high energy photons has a low probability. Conversely, inorganic scintillators are comprised of higher-Z material and absorb all detectable forms of radiation.

Light-decay constants for different scintillators can vary from a few nanoseconds to several milliseconds (Knoll 2000). The rate at which scintillation photons were produced is easily measured as a voltage following the PM tube. Hence, the timing profile of the electrical pulse indicates in which layers energy was absorbed. Radiation type may be determined by combining the likelihood of interaction with the electrical response (Farsoni 2006). Figure 2-21 illustrates a high-energy beta particle from ^{90}Sr interacting with two layers of a phoswich detector and the corresponding electrical response.

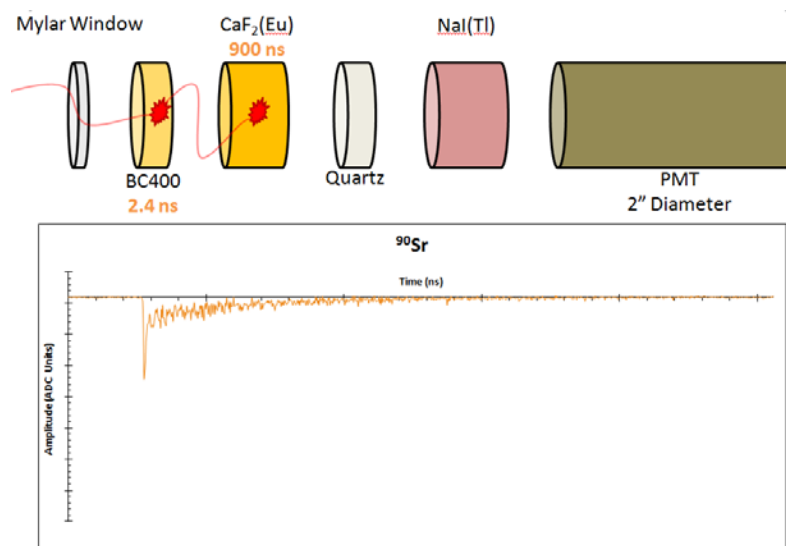


Figure 2-21: High-energy beta particle interacting in two layers of a phoswich and the recorded electrical pulse

The beta particle interacts with BC400 and CaF₂(Eu), which have 2.4 and 900 nanosecond light-decay constants, respectively. The electrical response clearly indicates two components of exponential decay or two different light-decay constants.

There are several factors that need to be addressed in order to build a successful phoswich detector. First the average wavelength of emission for each layer must fall within an acceptable range. Photons from the first layer need to transit through additional layers before they can be measured. Hence, the wavelength must be such that the photons view the scintillation layers as transparent. Another consideration is the index of refraction for each layer. If these indices are not similar, optical coupling efficiency will degrade the light collection ability of the phoswich.

A variety of phoswich detectors have been developed over the last two decades. Takada et al. (1996) developed a two layer system using an inner NE213 scintillator and an outer CaF₂(Eu) wall. It could separate fast (nanoseconds) and slow (microsecond) pulses from gamma-rays and neutrons. White et al. (1999) developed a triple-layer system that could discriminate between alpha/beta/gamma radiations. Miller et al. (2004) developed four prototype detectors; a triple-

layer system for alpha/beta/gamma swipe counting, well-type system that subtracts high energy background, a large area beta counting system for use in the presence of a photon background, and another large area system designed to measure low energy photons in the presence of a photon background. A fifth annular system is proposed for counting liquid waste streams. Farsoni (2006), Hennig et al., (2007), and Farsoni et al. (2008, 2009) have developed triple-layer systems for radioxenon measurements with varying scintillator geometries and methodologies.

2.6.4 Digital Pulse Processing

Traditional pulse processing utilizes bulky analog electronics to analyze the electrical response from a detection system. Digital systems have continued to evolve and are replacing analog systems (Grzywacz 2003). The electrical pulse from the PM tube needs to be conditioned and filtered before digital conversion. Impedance matching between the PM tube circuitry and an analog-to-digital converter (ADC) is accomplished with a preamplifier. Additionally, in order to satisfy the Nyquist-Shannon sampling theorem, the electrical pulse is subject to a low-pass filter prior to the ADC (Shannon 1949).

The ADC converts the incoming analog voltage into a binary number. The number of possible binary voltage amplitude assignments is known as the ADC's resolution. An 8-bit ADC can provide 2^8 or 256 unique amplitude assignments. The sampling rate reflects the number of times the ADC can perform the resolution function in a second (listed in Hz). The amplitude assignments are kept in order with respect to time. The ADC produces a series of data bits that accurately reflect the originally analog electrical pulse. The resolution and sampling rate are unique properties to each ADC model and many different configurations are commercially available.

The digital information moves in real time from the ADC to a processor that computes prescribed trigger criteria (Grzywacz 2003). When the trigger is met, the data may be manipulated as desired by the user. This may include data stored in onboard memory, transfer

to another system for storage and post-processing, or near real-time digital pulse processing. Figure 2-22 depicts a simplified digital detection diagram.

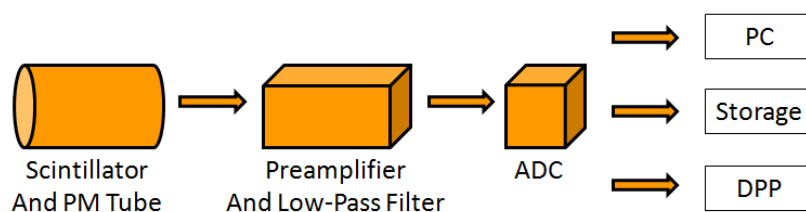


Figure 2-22: Diagram of digital signal processing steps

2.6.5 Pulse Shape Discrimination

A variety of methodologies have been developed to determine radiation type by pulse shape, commonly referred to as pulse shape discrimination (PSD). Most methodologies analyze components of the pulse rise-time. Ely et al. (2003) created a phoswich detector that utilized a variety of rise time measurements to separate beta and gamma events that originated in a $\text{CaF}_2(\text{Eu})$ window and $\text{NaI}(\text{TI})$ layer. However, beta-gamma coincident events could not be resolved. Grzywacz (2003) developed multiple digital phoswich systems that utilized 4 - 18 field programmable gate arrays (FPGA) in which histories of 'hits' could be reconstructed. The FPGA setup provides flexibility to process and store pulse information (Farsoni 2006). Figure 2-23 illustrates his digital detection process (Grzywacz 2003).

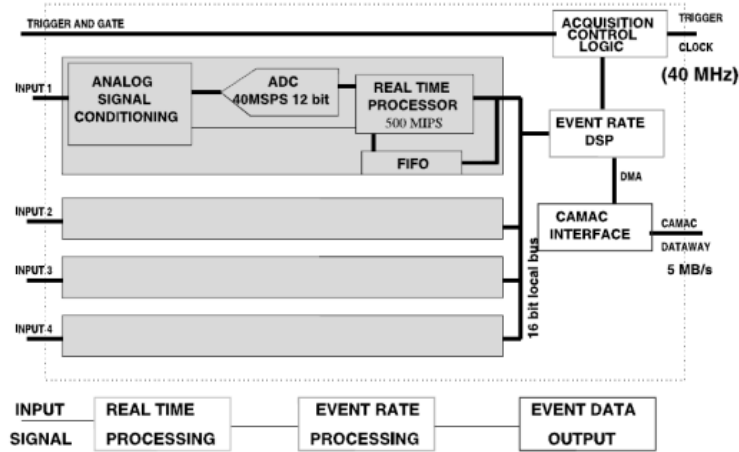


Figure 2-23: Multiple digital signal processors, configured in parallel (taken from Grzywacz 2003)

Hennig et al. (2005) developed a two layer phoswich (BC404 and CsI(Tl)) coupled with a pixie-4, which sent pulses to storage for post-processing. Pulses could be accurately separated as originating in the BC404, CsI(Tl), or a combination of the two layers utilizing an algorithm which combined pulse rise-time and energy thresholds.

Farsoni (2006) and Farsoni et al. (2007a) developed a triple-layer phoswich detector (BC400; $\text{CaF}_2(\text{Eu})$; $\text{NaI}(\text{Tl})$) coupled to a high-speed ADC and FPGA loaded with proprietary corresponding algorithm which measured four parameters (baseline; peak amplitude; M1; M2) of each pulse to determine from which layers the pulse originated. Two additional parameters (A and B) are measured to determine the amount of energy deposited in each layer. Figures 2-24 and 2-25 illustrate the measurements utilized in their work (Farsoni et al. 2007a).

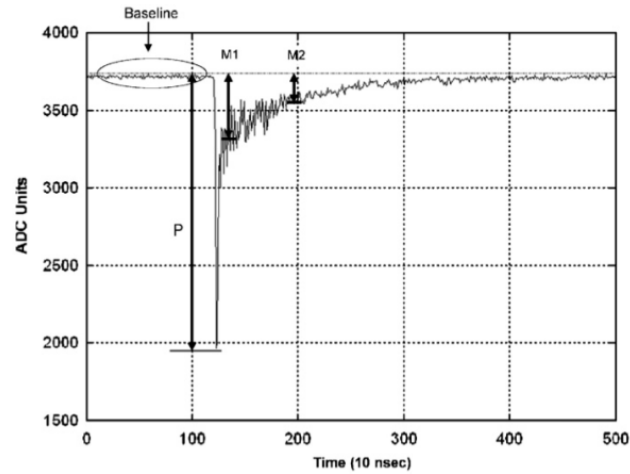


Figure 2-24: Measurement of electrical baseline, peak amplitude, and relative decays M1 and M2 (taken from Farsoni et al. 2007a)

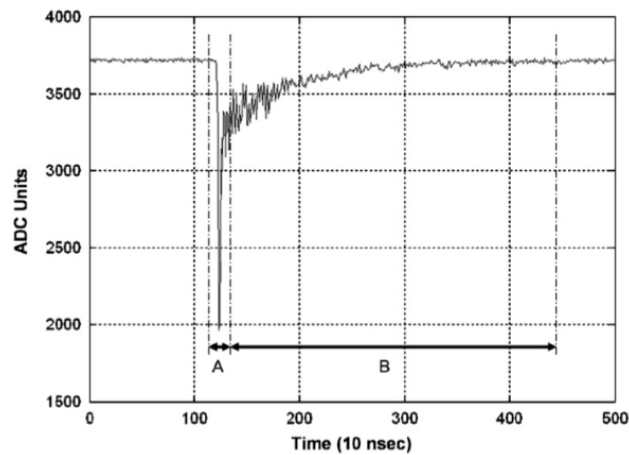


Figure 2-25: Area measurements A and B, to assess deposited energy by layer (taken from Farsoni et al. 2007a)

Methodologies are constantly improving as newer ADC's and processors have improved operating speeds, resolution, and processing power. The most recent methodologies take advantage of these improvements and involve near real-time pulse integration, allowing for accurate Compton suppression through anti-coincidence logic (Farsoni et al. 2010b).

3 Materials and Methods

3.1 Prototype Triple-Layer Phoswich

Farsoni and Hamby modeled (Farsoni et al. 2005) and built (Farsoni 2006) a triple-layer phoswich designed for beta particle and gamma-ray detection. The first layer consists of a low-Z organic scintillator (BC400) with a fast light-decay constant, intended for low-energy beta particle detection. The second layer consists of a low-Z inorganic scintillator ($\text{CaF}_2(\text{Eu})$) with a very slow light-decay constant, intended for high-energy beta particle detection. The combination of these two layers is sufficient to stop beta particles up to 3.2 MeV (Farsoni 2006). The third layer consists of a high-Z inorganic scintillator ($\text{NaI}(\text{Tl})$) with a light-decay constant in-between the preceding two layers, intended for gamma-ray detection. These scintillators share similar maximum emission wavelengths and refractive indices. Properties for these materials are listed in Table 3-1 below.

Table 3-1: Physical properties of scintillation material used in the studied phoswich

Scintillator	Density (g/cm ³)	Max. Emission Wavelength (nm)	Light Output (% $\text{NaI}(\text{Tl})$)	Index of Refraction	Light Decay Constant (ns)
BC400	1.032	423	26	1.58	2.4
$\text{CaF}_2(\text{Eu})$	3.19	435	50	1.47	900
$\text{NaI}(\text{Tl})$	3.67	415	100	1.85	230

The front window of the phoswich is comprised of aluminized mylar. An inert layer of transparent quartz crystal lies between the $\text{CaF}_2(\text{Eu})$ and $\text{NaI}(\text{Tl})$ layers to prevent moisture degradation of the $\text{NaI}(\text{Tl})$ layer owing to its hygroscopic nature (Farsoni 2006). The quartz layer does attenuate beta particles and as such, a beta particle must have an initial energy above 6.7 MeV to reach the $\text{NaI}(\text{Tl})$ layer (Farsoni 2006). The layers are packaged inside an aluminum housing and are optically coupled to a two inch diameter PM tube (ETI 1266¹). Figure 3-1 is an

¹ Saint-Gobain Crystals Inc. 6801 Cochran Road, Solon, Ohio 44139

illustration of the phoswich detector and Figure 3-2 is a photograph of the actual phoswich detector.

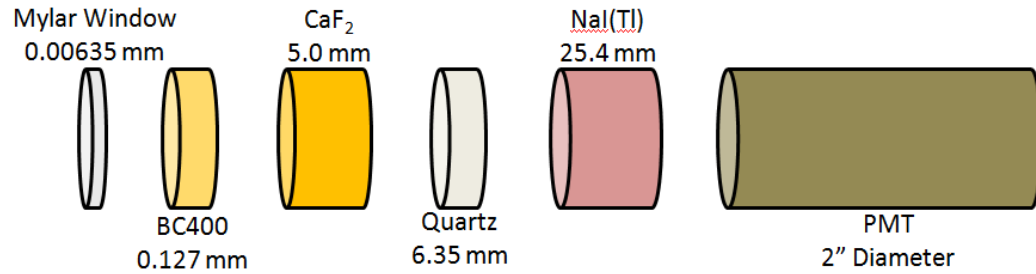


Figure 3-1: Layers of the studied phoswich detector



Figure 3-2: Photograph of the studied phoswich in its final state

These scintillating materials and geometries were specifically chosen for two reasons: first, incident radiation ideally imparts all energy into either the first layer (low-energy beta particle), the first and second layer together (high-energy beta particle), or the third layer (gamma-ray); second, the large separation in light decay constants provides a means for discriminating between events in the different layers (Farsoni 2006).

There are nine possible interaction scenarios for this phoswich detector relative to beta particles and gamma-rays, two of which are superfluous for practical purposes (no interaction at all, beta particle interaction in all three layers ($E_{\beta\text{max}} > 6.7 \text{ MeV}$)). The remaining seven scenarios

were modeled with Monte-Carlo N-Particle (MCNP) simulation (Farsoni et al. 2006). Table 3-2 lists the probability for all seven interaction scenarios given 1 MeV beta particles or separately 1 MeV gamma-rays².

Table 3-2: Probability of 1MeV beta particle or gamma-ray interaction by layer in the studied phoswich²

Interaction Layer (X)			Probability (%)		Pulse Recorded as
BC400	CaF ₂ (Eu)	NaI(Tl)	Gamma	Beta	
X			0.35	12.32	Beta Particle
X	X		0.07	81.70	Beta Particle
X	X	X	0.01	0.57	Rejected
X		X	0.06	0.08	Rejected
	X		14.40	4.60	Rejected
	X	X	2.65	0.03	Rejected
		X	12.87	0.00	Gamma-ray

The MCNP results indicate that the most probable beta particle interactions match those desired by design. Similarly, gamma-ray interactions are probabilistically limited to NaI(Tl) or CaF₂(Eu) layers. However, gamma-ray interaction in the CaF₂(Eu) layer is not desired due to the differences in light output and light decay constant for this material. Interactions of beta particles and gamma-rays that occur in any combination of layers outside the three ideal scenarios are rejected. Rejected scenarios and other coincidence events are often referred to as ‘cross-talk’ in the interaction history of a counting period (Farsoni 2008).

A MATLAB algorithm has been developed which determines the interaction scenario responsible for the observed electrical pulse. Additionally, the algorithm quantifies the energy of the incident radiation and can plot a corresponding energy spectrum. The MATLAB algorithm methodology and application are discussed in further detail in section 3.3 below.

² A.T. Farsoni, D.M. Hamby, A system for simultaneous beta and gamma spectroscopy, Nuclear Instruments and Methods in Physics Research, A 578 (2007) 528–536

3.2 Phoswich Detection System

The detection system was configured similarly throughout all prototyping and testing phases. The phoswich component was shielded by two-inch lead bricks. Radioactive sources were contained within the shielding during the prototyping phase. The shielding configuration was altered during the testing phase to minimize Compton scattering effects. During testing, the phoswich window was moved outside of the shield so that only low-Z material remained between sources and the phoswich. A black cloth placed over the lead shield and radioactive sources acted as an additional light shield. Figure 3-3 is a photograph of testing phase shielding configuration.



Figure 3-3: Shielding configuration during testing phase, the black cloth would be moved over the phoswich window while taking measurements

High-voltage (HV) coaxial cable connected the phoswich PM tube to power from a NIM bin based HV power supply. An additional coaxial cable sent analog electrical pulses from the phoswich to a digital pulse processing (DPP) board with components described in sections 3.2.1 and 3.2.2 below. This board was designed by Farsoni and is referred to as 'DPP 2.0'. The DPP 2.0 board converts the analog pulse into a digital signal which is temporarily stored on a circular buffer. A trigger system is employed that when satisfied, releases a pulse via USB 2.0 to a Dell Optiplex GX620 desktop PC (Intel Pentium D series), running Windows XP operating system, and

MATLAB R2007a. Pulses may then be processed in real time or saved for post-processing as desired. In this work, all signal processing is handled exclusively by MATLAB. Copies of MATLAB code for real time analysis is provided in Appendix A.

3.2.1 Analog Electronics

Analog electronics are still necessary to convert the electrical pulse generated at the anode of the PM tube into a digital signal. A preamplifier is used to impedance match the analog pulse from the PM tube to the DPP circuitry. From there a 3rd order, low-pass Bessel filter eliminates any electrical pulse component above 95 MHz to satisfy the Nyquist-Shannon Sampling Theorem (Farsoni et al. 2008). The analog pulse is then subject to a differentiating amplifier (Analog Devices³ AD8138A), required for optimal wideband performance of the analog-to-digital converter (ADC) (Analog 2007). The analog pulse is then sampled at 200 MHz with 12-bit resolution by an ADC converter (Analog Devices² AD9230). The digitized signal is sent to a DPP module, where trigger logic and circular buffer are implemented.

3.2.2 Digital Pulse Processor

The DPP module is based on an Opal Kelly XEM3010⁴, which includes a FPGA (SPARTAN-3 XC3S1500-4FG320) and USB microcontroller (Cypress CY7C68013A). The FPGA hosts trigger logic and circular buffer functions, while the USB microcontroller enables transmission of data from the DPP to a PC via USB 2.0.

Trigger logic is based on the convolution of a 75 nanosecond triangular filter with digital data from the ADC. The convolution operation is covered in more detail in section 3.3. The result is an assessment of whether the data covered by the filter contains the beginning of a new pulse. An adjustable threshold setting provides the minimum convolution result which indicates a pulse has been detected. The circular buffer releases 450 nanoseconds of data

³ Analog Devices Inc. One Technology Way, P. O. Box 9106, Norwood, MA 02062-9106

⁴ Opal Kelly Incorporated, 3442 SE Ironwood Ave., Hillsboro, OR 97123

before the trigger point and 4665 nanosecond of data following the trigger point, when trigger logic is satisfied. Therefore, each pulse represents 5115 nanoseconds of continuous data or 1024 twelve-bit data points.

3.3 MATLAB Algorithm

Farsoni et al. (2008) developed a discrimination methodology that analyzes the area of a pulse with respect to three different triangular filters. Pulse area is calculated utilizing the convolution mathematical operator. Convolution is an operation on two functions $f(\tau)$ and $g(\tau)$, producing a third function, which is a modified version of one of the two original functions. Convolution is expressed by:

$$(f * g)(t) \stackrel{def}{=} \int_{-\infty}^{\infty} f(\tau) g(t - \tau) d\tau = \int_{-\infty}^{\infty} f(t - \tau) g(\tau) d\tau \quad (3.1)$$

For pulse discrimination, $f(\tau)$ is a triangular filter and $g(\tau)$ is the digitized pulse. The resultant function of the integration is area versus time, relative to the size of the triangular filter.

The size of the three filters is based on the light-decay constant for each active layer of the phoswich. The first filter produces an assessment of the pulse area in a small time step (50 ns) relating to the BC400 layer, and is denoted, f_a . The second filter produces an assessment of the pulse area in a larger time step (300 ns) relating to the NaI(Tl) layer, and is denoted, f_b . The third filter produces an assessment of the pulse area in a very large time step (3000 ns) relating to the $\text{CaF}_2(\text{Eu})$ layer, and is denoted, f_c .

Two ratios that portray the timing profile of the electrical pulse are derived from these three area assessments. The first ratio, referred to as the Fast Component Ratio (FCR), portrays how quickly a pulse decays by comparing the maximum area of first filter to that of the second filter. The FCR is calculated by:

$$FCR = \frac{f_a}{f_b} \quad (3.2)$$

Incident radiation that interacts solely in the BC400 layer (first layer) will produce a rapidly decaying pulse (40-50 ns) (Farsoni 2006). In this case, f_a and f_b would roughly equal each other and the FCR value should be close to unity. An interaction in multiple layers will exhibit a slower decaying pulse. Therefore, f_a is smaller than f_b and the FCR value shifts to be noticeably less than unity. Figure 3-4 is the electrical pulse recorded by the detector from beta particle interactions in BC400 only.

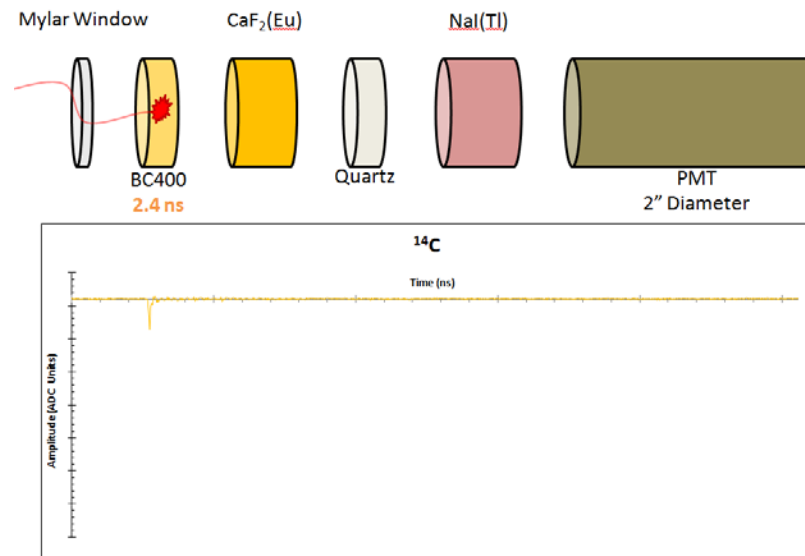


Figure 3-4: Pulse recorded from beta particle interaction in the BC400 layer

The second ratio, referred to as the Slow Component Ratio (SCR), portrays how slowly the tail of a pulse decays. $\text{CaF}_2(\text{Eu})$ has a much slower light-decay constant than the other two materials. However, beta particles that interact in the $\text{CaF}_2(\text{Eu})$ layer must cross the BC400 layer first, and inevitably deposit some energy there. This produces an initial fast response in the observed pulse. As a result, the tail of such a pulse reveals accurate information about the $\text{CaF}_2(\text{Eu})$ light-decay constant. Therefore, the f_a filter is subtracted during SCR assessment. The SCR is calculated by:

$$SCR = \frac{f_b - f_a}{f_c - f_a} \quad (3.3)$$

Incident radiation that interacts with the NaI(Tl) layer only, produces a moderately decaying pulse (Fig. 3-5). In this scenario f_a produces the smallest response, f_b produces a large response, and f_c produces the largest response. About 65 percent of the light produced in the NaI(Tl) layer is recorded by f_b and as a result, the difference between f_b and f_c is significant, but not extreme. In this scenario an SCR value of around 0.5 is expected.

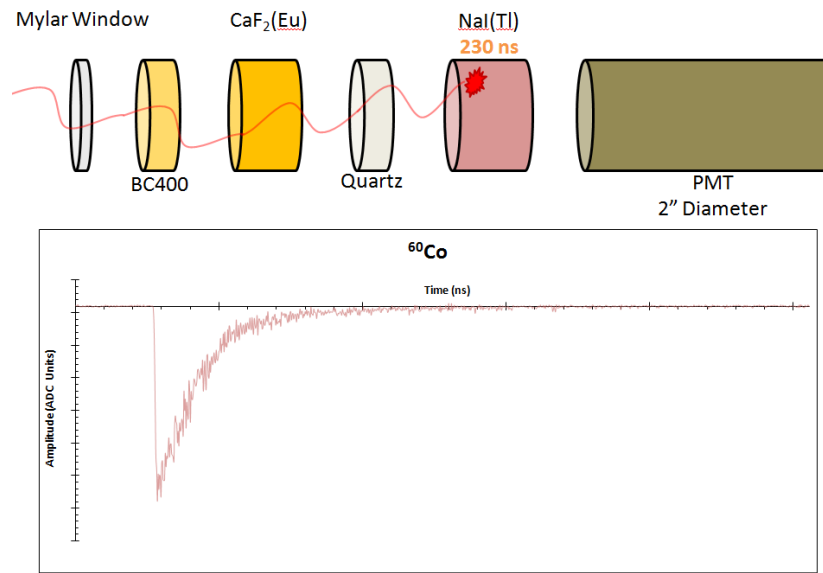


Figure 3-5: Pulse recorded from gamma-ray interaction in the NaI(Tl) layer

Incident radiation that interacts with both BC400 and $\text{CaF}_2(\text{Eu})$ layers will have a quickly decaying initial peak generated from BC400, followed by a very slowly decaying pulse generated from the $\text{CaF}_2(\text{Eu})$ (Fig. 3.6). In this scenario f_a still produces the smallest response, f_b produces a moderate response, and f_c produces a significantly larger response than f_b . Now the difference between f_b and f_c is substantial and the SCR value is expected to be lower than 0.5.

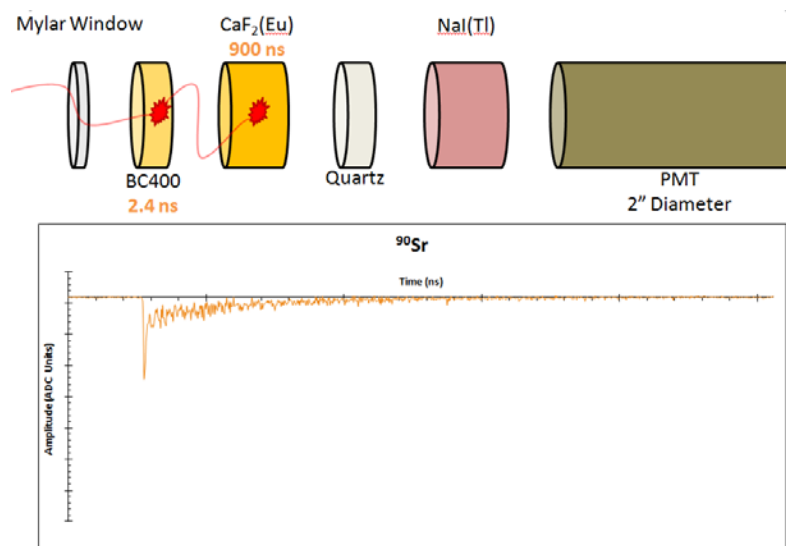


Figure 3-6: Pulse recorded from beta particle interaction in the BC400 and CaF₂(Eu) layers

Pulse discrimination is achieved by calculating the FCR and SCR for known radionuclides. The FCR and SCR data for valid pulses forms a 2D histogram, from which FCR/SCR regions that depict interaction between specific layer(s) are defined (Farsoni et al. 2008). Incident radiation may then be compared against the defined regions and categorized accordingly. Figure 3-7 is a FCR/SCR 2D histogram for unshielded ¹³⁷Cs.

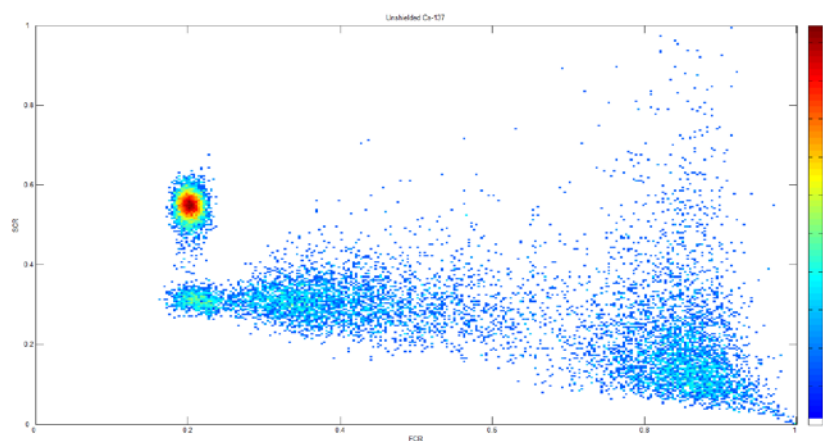


Figure 3-7: 2D histogram of FCR and SCR values from 65,000 pulses collected from an unshielded ¹³⁷Cs source. The color bar represents density where points overlap and is in log scale

There are several parameters in the algorithm that need to be determined prior to accurate pulse discrimination, including the FCR and SCR regions, and will be discussed in the following sections.

3.3.1 Offset and Gain

Offset and gain settings in MATLAB need to be optimized for the studied detector configuration. The offset adjusts the location of the baseline electrical response. Gain adjusts the amplification of the signal. These two parameters are set such that the largest electrical pulse from the PM tube resides within $\pm 10\%$ of the maximum and minimum amplitude assignments from the ADC (Analog 2007). Twelve-bit resolution translates to 4096 amplitude assignments (ADC units). Therefore, the offset and gain need to be set so that pulses do not exceed 3686 or fall below 410 ADC units.

Several reference sources were independently placed in the detector apparatus and ^{60}Co produced the largest electrical pulse. The offset and gain were varied until the pulses satisfactorily met the 10% criteria. The offset was determined to be 1985 with a corresponding gain of 2650. Figure 3-8 illustrates the initial and final offset and gain settings from a ^{60}Co source.

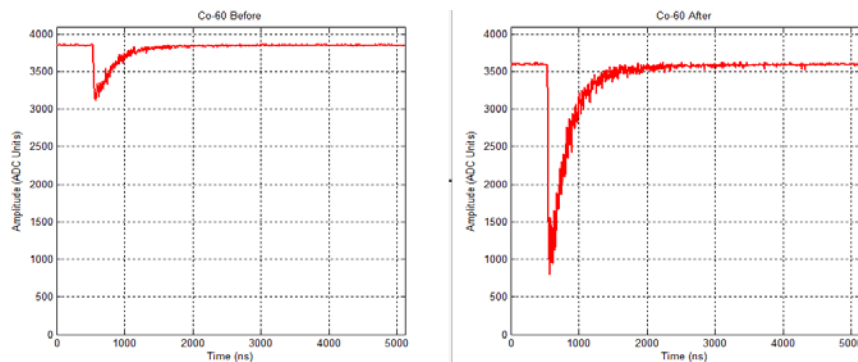


Figure 3-8: The effect of offset and gain settings on pulses collected from a beta-particle shielded ^{60}Co source

3.3.2 Threshold

The threshold criterion sets the minimum convolution area required for trigger logic to be satisfied. If the threshold is set too low, dark counts from the PM tube or electronic noise may trigger the circular buffer as valid pulses. If the threshold is set too high, beta particles and gamma-rays may not be counted at all. To determine the optimal threshold criteria, a ^{14}C source was placed 5 cm from the detector and the trigger logic threshold criterion was set to the lowest possible value, allowing for spurious pulses to be collected alongside valid pulses. A variant MATLAB algorithm was developed that included an extra filter, prior to FCR/SCR calculation, which mimicked trigger logic. Like trigger logic, a minimum convolution area was established to validate a pulse.

The threshold criterion was analyzed by varying the DPP trigger logic threshold value, while using a fixed minimum convolution area (650 ADC Units) associated to the extra filter in the variant MATLAB algorithm. The extra filter acted in place of trigger logic and calculated the number of valid and invalid pulses released by trigger logic for different threshold values. Both valid and invalid pulses were analyzed to determine the energy associated with each type of event. Figure 3-9 illustrates the number of pulses out of 10,000 that were validated or invalidated while varying the DPP threshold value. Figure 3-10 illustrates the average energy deposited for validated and invalidated events with varying DPP threshold values.

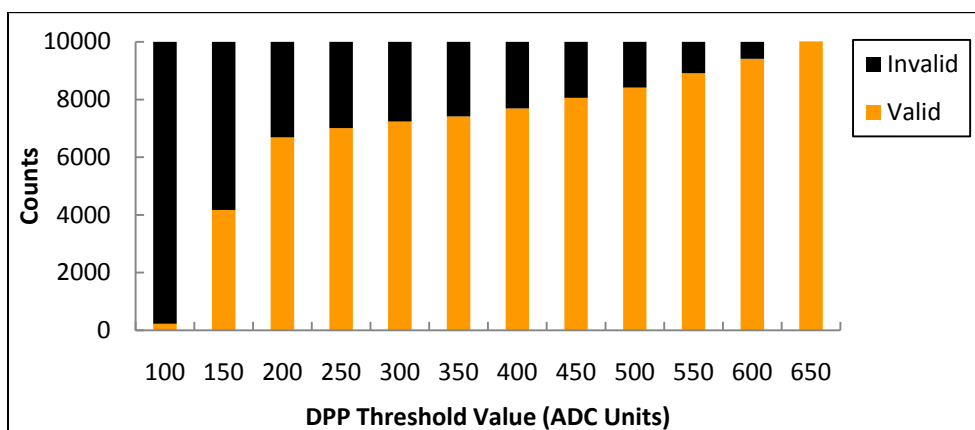


Figure 3-9: Validated and invalidated pulses out of 10,000 per threshold setting

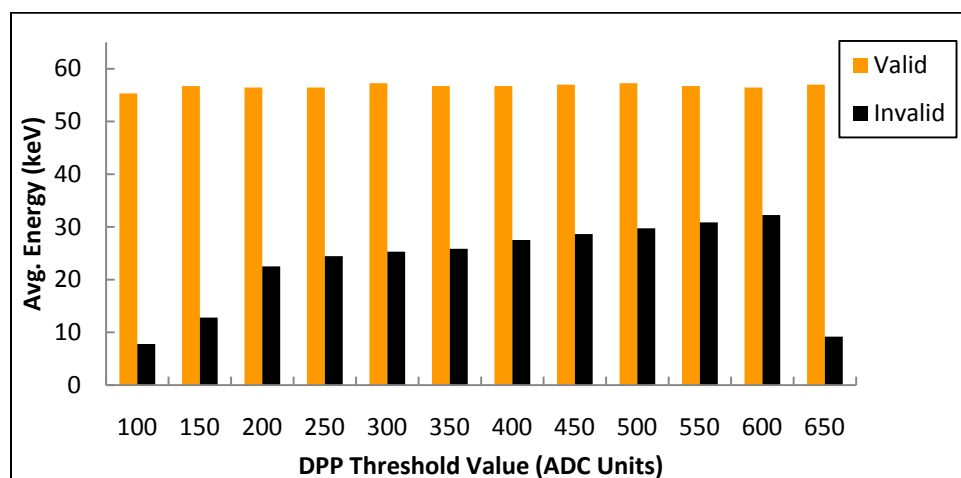


Figure 3-10: Average energy of validated and invalidated pulses per threshold setting

The threshold criterion used during prototyping and testing phases was conservatively defined at 650 ADC units or an energy deposition of about 55 keV for gamma-rays and 35 keV for beta particles. Any pulses, spurious or otherwise that are less than these values will not trigger a release from the circular buffer. This threshold setting was acceptable for this research objective, but will not be suitable when low-energy radiation is important. The threshold may be adjusted to lower energies as necessary with marginal inclusion of spurious counts to 200 ADC units or an energy deposition of about 20 keV.

3.3.3 Relaxation Correction

Farsoni et al. (2009) discovered and corrected a phenomenon observed from pulses created in the BC400 layer, dubbed “ringing effect”. Ringing effect occurs when a pulse decays very rapidly towards the baseline voltage, but rather than stabilize at baseline, the pulse would move beyond baseline resulting in a decaying oscillation around baseline (Fig. 3-11). The average area under the decaying oscillation was found to be non-zero, affecting the FCR calculation.

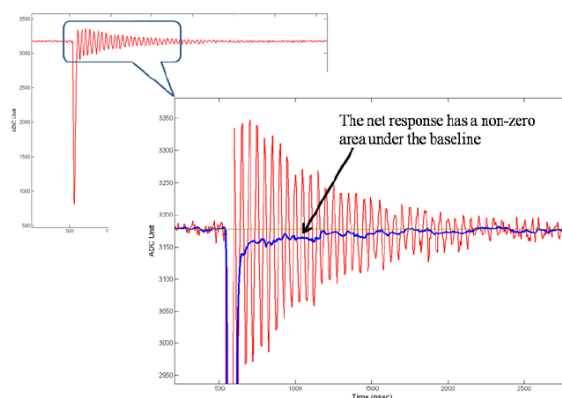


Figure 3-11: Ringing effect observed by Farsoni et al. (2009)

The ringing effect was determined to be produced by a low quality voltage divider inside the PM tube (Farsoni et al. 2009). An additional parameter known as relaxation correction was added to the MATLAB algorithm to prevent incorrect pulse discrimination of beta particles. Relaxation correction operates by calculating the average value over 50 nanoseconds, 250 nanoseconds after the pulse's peak. Another 50 nanosecond average is calculated 400 nanoseconds before the peak, which represents the true baseline value. The first average is divided by the second and if the resulting ratio is greater than or equal to 0.95, the pulse's FCR is automatically set to 1. If the ratio is less than 0.95, no change to the FCR calculation occurs. Figure 3-12 demonstrates the effect relaxation correction has on a FCR/SCR 2D histogram.

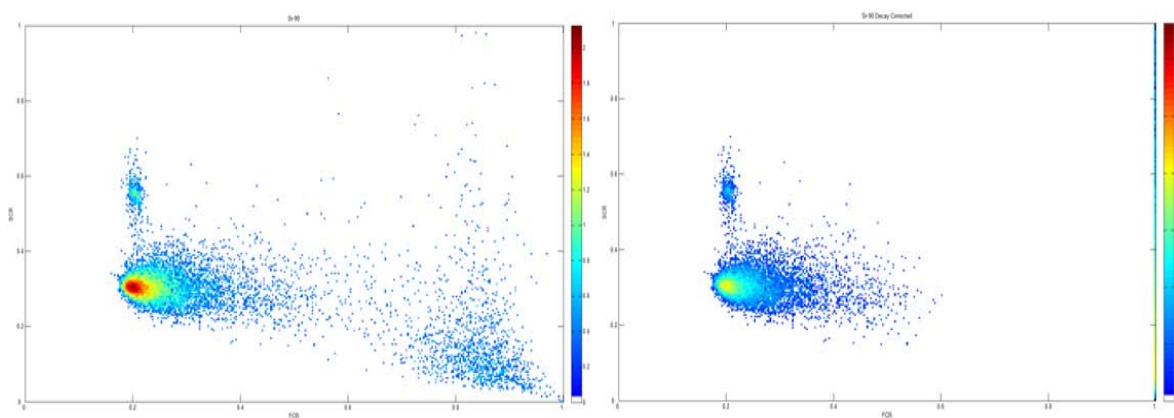


Figure 3-12: Relaxation correction effect on the same FCR/SCR data set, notice the colored line on the FCR (x) axis at unity in the picture on the right

3.3.4 Fast Component Ratio and Slow Component Ratio Regions

An unshielded ^{137}Cs source was used to establish beta particle and gamma-ray interaction regions in the FCR/SCR 2D histogram that represent different interactions in the layer(s) of the phoswich. These regions were verified with ^{14}C and ^{90}Sr for beta particle interactions and ^{60}Co for gamma-ray interactions. Figure 3-13 depicts the FCR/SCR regions and Table 3-3 defines the interaction layer, incident radiation type, and if the region is important.

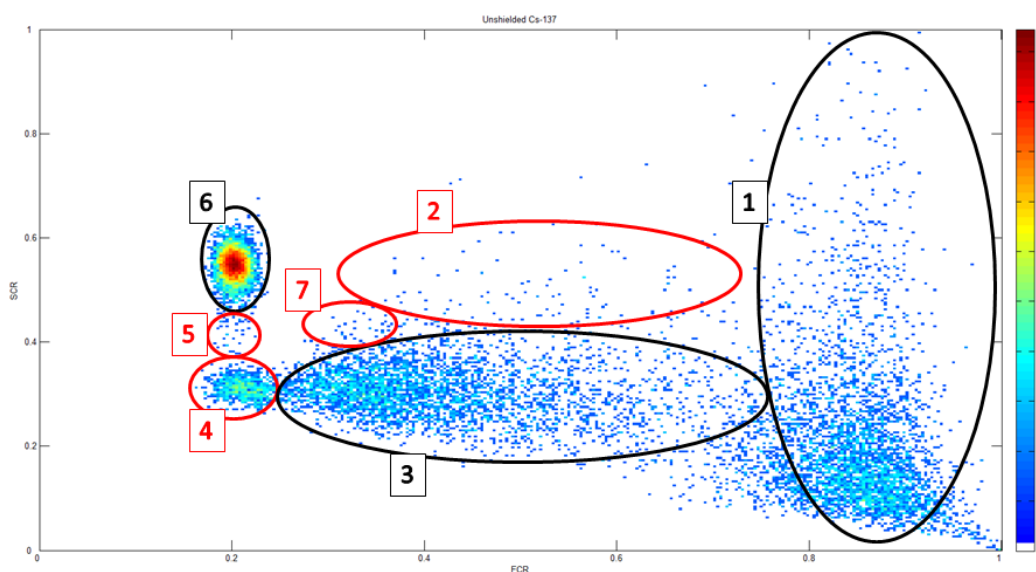


Figure 3-13: Outlined interaction regions of a 2D FCR/SCR histogram from an unshielded ^{137}Cs source

Table 3-3: Interaction type and region as defined from the 2D FCR/SCR histogram illustrated in Fig. 3.13 above

Region	Interaction Layer	Interaction Type	Accepted/Rejected
1	BC400	Beta Particle	Accepted
2	BC400 + NaI(Tl)	Coincidence Gamma-ray, Beta/CE	Rejected
3	BC400 + $\text{CaF}_2(\text{Eu})$	Coincidence X-ray, Beta/CE	Accepted
4	$\text{CaF}_2(\text{Eu})$	X-ray, Gamma-ray	Rejected
5	$\text{CaF}_2(\text{Eu}) + \text{NaI}(\text{Tl})$	Coincidence Gamma-ray	Rejected
6	NaI(Tl)	Gamma-ray	Accepted
7	BC400 + $\text{CaF}_2(\text{Eu}) + \text{NaI}(\text{Tl})$	Coincidence Gamma-ray, Beta/CE	Rejected

A relaxation corrected series of pulses from a ^{137}Cs button source that was not shielded against beta particles, were collected and used to determine the FCR and SCR regions for gamma-ray interaction in NaI(Tl) and beta particle interaction in BC400 and BC400 + $\text{CaF}_2(\text{Eu})$. Table 3-4 lists the FCR and SCR values for the desired regions. The following three figures (Fig. 3-14, 3-15, and 3-16) illustrate pulse discrimination by the determined FCR and SCR regions given identical data.

Table 3-4: Experimentally determined FCR and SCR regions

Layer	FCR Region	SCR Region	Particle Type
NaI(Tl)	0.15 to 0.25	0.45 to 0.75	Gamma-rays
BC400	Must Equal 1	0 to 1	Low-Energy Beta Particles
BC400 + $\text{CaF}_2(\text{Eu})$	0.25 to 1	0.2 to 0.425	High-Energy Beta Particles

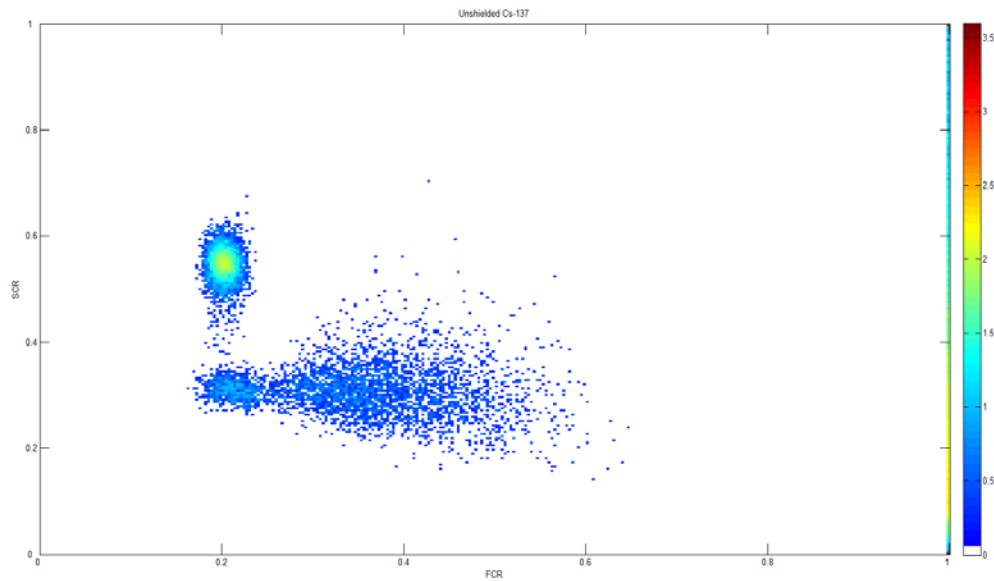


Figure 3-14: Relaxation corrected 2D FCR/SCR histogram from unshielded ^{137}Cs

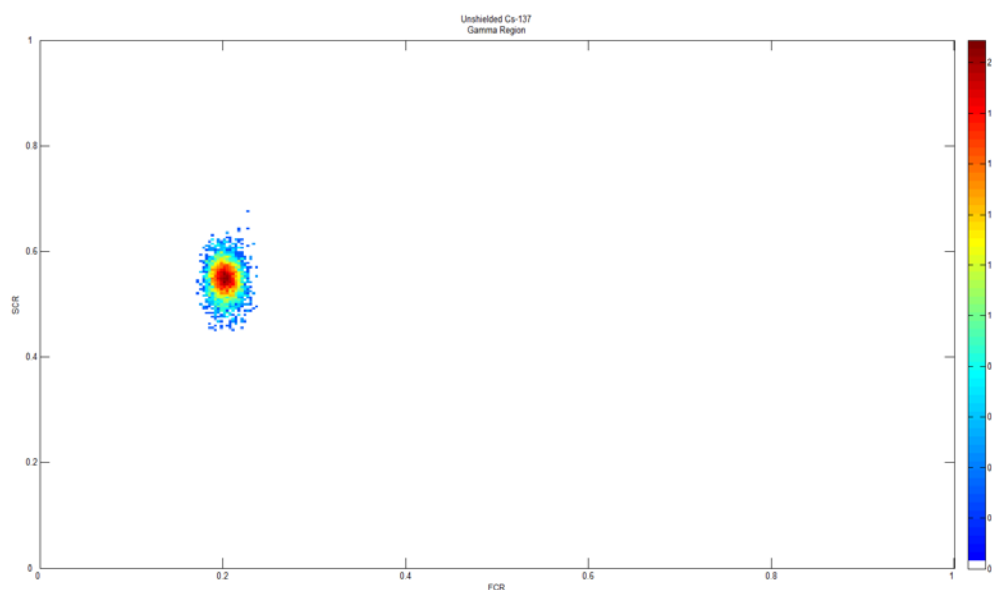


Figure 3-15: Relaxation corrected 2D FCR/SCR histogram from unshielded ^{137}Cs with NaI(Tl) region selected

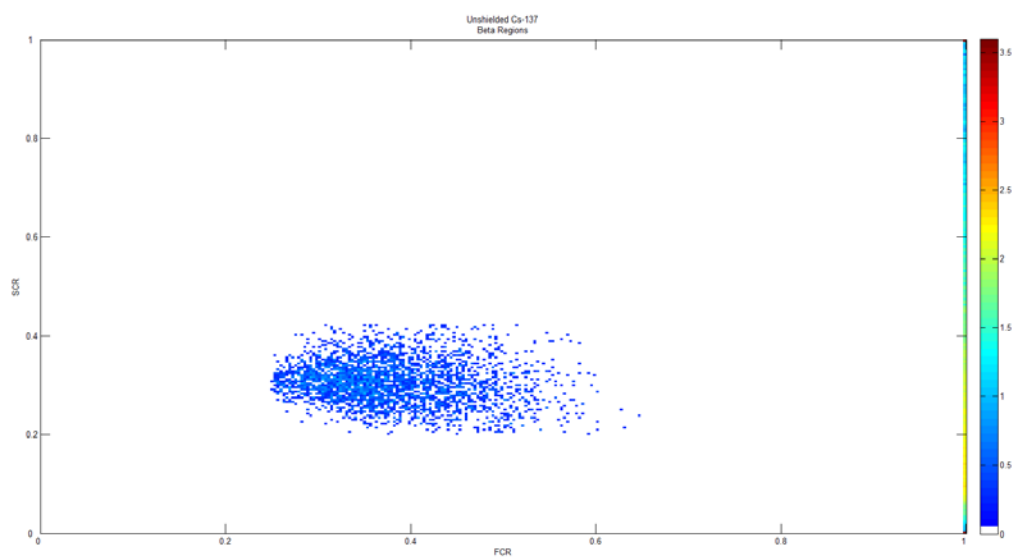


Figure 3-16: Relaxation corrected 2D FCR/SCR histogram from unshielded ^{137}Cs with BC400 and $\text{CaF}_2(\text{Eu})$ regions selected

3.3.5 Optimal Filter Size

The filters are designed for two purposes: first, they must be sufficiently different in size from one another to allow for accurate pulse discrimination; second, they must be of sufficient size to accurately calculate the area of pulses' created in their respective layer(s) of the phoswich. A balance between these two purposes needs to be maintained. Raw pulses were collected from ^{137}Cs and the f_a and f_c filter sizes were adjusted to determine optimal filter size for these two layers. The f_b filter was fixed at 300 nanoseconds, a length of time which is about one light-decay constant for the NaI(Tl) layer, and as it has the least affect on FCR and SCR calculations.

It was plainly observed that smaller f_a filter values (around 30 ns) provided improved separation between BC400 + $\text{CaF}_2(\text{Eu})$ region (beta particles) over the pure $\text{CaF}_2(\text{Eu})$ region (x-rays and gamma-rays). However, smaller f_a filter values underestimated the pulse area from pure BC400 layer interactions. A value of 50 nanoseconds was selected as providing adequate separation between the regions and accurate assessment of pulse area. It was also observed that an f_c filter value of 3,000 nanoseconds produced accurate results. Values less than 3,000 nanoseconds consolidated regions into increasingly smaller areas, while values greater than 3,000 exhibited a Gaussian broadening of the regions. Examples of the FCR/SCR 2D histograms with varying filter values are provided in Appendix B.

3.4 Radioactive Sources

Different forms of radiation sources were used throughout testing which include: sealed button sources; electroplated foil sources; and filter paper sources. The complete list of radioisotope used, activity level, targeted beta particle and gamma-ray energies are listed in Table 3-5 below.

Table 3-5: Radioactive sources used, activity at time of measurement, target emission type, and energy

Source Type	Radionuclide(s)	Activity (μCi)	Target Emission Type and Energy		
Sealed Button	¹³⁷ Cs	0.855	γ, 662 keV		
Sealed Button	⁶⁰ Co	0.78	γ, 1173 keV	γ, 1332 keV	
Sealed Button	⁵⁷ Co	1.5E-4	γ, 122 keV		
Sealed Button	¹³³ Ba	0.405	x-ray, 30.9 keV	γ, 356 keV	
Sealed Vial	²⁴ Na/ ³⁸ Cl	Undefined	γ; 2754, 2167, 1642, 1368 keV		
Foil	¹⁴ C	10	β _{max} ≈ 156 keV	B _{avg} ≈ 49 keV	
Foil	⁹⁰ Sr/ ⁹⁰ Y	0.0164	β _{max} ≈ 546 keV	β _{avg} ≈ 196 keV	
Foil			β _{max} ≈ 2280 keV	β _{avg} ≈ 934 keV	
Foil	³⁶ Cl	0.0188	β _{max} ≈ 709 keV	β _{avg} ≈ 251 keV	
Filter Paper (Sample 1)	¹³⁷ Cs	0.13	γ, 662 keV	β _{max} ≈ 514 keV	β _{avg} ≈ 174 keV
	¹⁴ C	0.02	β _{max} ≈ 156 keV	β _{avg} ≈ 49 keV	
	⁹⁰ Sr/ ⁹⁰ Y	0.02	β _{max} ≈ 546 keV	β _{avg} ≈ 196 keV	
			β _{max} ≈ 2280 keV	β _{avg} ≈ 934 keV	
Filter Paper (Sample 11)	¹³⁷ Cs	0.077	γ, 662 keV	β _{max} ≈ 514 keV	β _{avg} ≈ 174 keV
	¹⁴ C	0.048	β _{max} ≈ 156 keV	β _{avg} ≈ 49 keV	
Filter Paper (Sample 10)	¹³⁷ Cs	0.077	γ, 662 keV	β _{max} ≈ 514 keV	β _{avg} ≈ 174 keV
	⁹⁰ Sr/ ⁹⁰ Y	0.018	β _{max} ≈ 546 keV	β _{avg} ≈ 196 keV	
			β _{max} ≈ 2280 keV	β _{avg} ≈ 934 keV	

The filter paper sources are based on a specific end-user scenario and need some description. The first commercial generation of similar detector design has been purchased to analyze water and air samples that will be processed by filter paper collection. The end-user provided details on the dimension of the filters to be used in their apparatus. Thirteen similarly sized filter paper samples were prepared at Oregon State University. The filter paper used (WhatmanTM Cat No. 1001-042⁵) measures slightly less than two inches in diameter and were glued onto two-inch diameter planchets. Three radioisotopes (^{14}C , $^{90}\text{Sr}/^{90}\text{Y}$, ^{137}Cs) in a liquid state were mixed together at varying levels of activity, and evenly distributed onto the filter paper samples. These samples of mixed radioisotopes were used alongside the sealed and foil sources. Figure 3-17 is a photograph of three filter samples.

⁵ Whatman Inc., Building 1 800 Centennial Ave, Piscataway, NJ 08854



Figure 3-17: Beta particle and gamma-ray filter samples 1, 10, and 11. Filter samples were measured without plastic cases.

3.5 Characterization Tests

A series of tests designed to evaluate characteristics of the complete detector system were compiled from the literature, end-user specifications, and applicable ANSI standards (N42.34-2006, N42.43-2006) developed for the Department of Homeland Security. A description of each test and applicable standards are described in the following sections.

3.5.1 System Efficiency with varying Energy

The absolute efficiency of a detection system is based solely on two factors; the number of radioactive particles emitted by the source in a given amount of time, and the number of radioactive particles detected by the system during the same amount time. Absolute efficiency is defined as:

$$\epsilon_{abs} = \frac{\text{pulses detected}}{\text{radiation emitted by source}} \quad (3.4)$$

Intrinsic efficiency accounts for only those emitted particles that are incident upon the detector. The solid angle (Ω) is the integrated cone of emitted radiation traveling from the source that will

reach the detector (Knoll 2000). Figure 3-18 illustrates the solid angle between a discrete isotropic point source and right cylindrical detector, where S is the source and d the distance between source and detector (Knoll 2000).

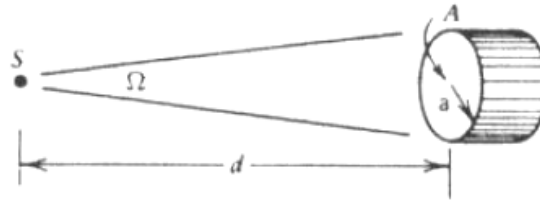


Figure 3-18: Solid angle relative to a point source and detector window (taken from Knoll 2000)

Thus, the intrinsic efficiency is the absolute efficiency corrected for geometric losses and may be solved by:

$$\varepsilon_{\text{int}} = \frac{\text{pulses detected}}{\text{radiation incident upon detector}} = \varepsilon_{\text{abs}} \left(\frac{4\pi}{\Omega} \right) \quad (3.5)$$

All sources used in this study were idealized as infinitely thin disks rather than discrete points. The solid angle calculation is rather different for disk sources than one which may be determined from figure 3-18 above. However, the theory is the same. The approximate solid angle for disk sources relative to a right cylindrical detector is solved with a complicated series of equations, which may be found in Knoll 2000, page 119.

Full-energy-peak efficiency relates only to incident radiation with deposited energy localized around a single full-energy-peak, rather than the whole spectrum. Most gamma-ray detectors are characterized by their intrinsic full-energy-peak efficiencies. ANSI requires that the manufacturer state the full-energy-peak efficiency for gamma-rays from ^{57}Co (122 keV), ^{133}Ba (356 keV), ^{137}Cs (662 keV), and ^{60}Co (1173 and 1332 keV). In addition to ANSI requirements, intrinsic full-energy-peak efficiencies for the above gamma-rays will be calculated, and detector efficiency for beta particles from ^{14}C , ^{36}Cl , and $^{90}\text{Sr}/^{90}\text{Y}$ will be measured. Furthermore, the efficiencies will be compared with values from mixed filter paper sources to determine any

performance difference in a mixed beta particle and gamma-ray radiation field. The test will be conducted with sources on axis and a distance of 5 cm from the phoswich window.

3.5.2 System Efficiency with varying Count Rate

^{137}Cs and ^{60}Co sources will be placed on axis at varying distances from the phoswich window, producing different levels of incident count rate upon the detection system. The intrinsic full-energy-peak efficiency will be measured at varying count rates to determine if system performance varies with incident count rate. Similarly, ^{14}C , ^{36}Cl , and $^{90}\text{Sr}/^{90}\text{Y}$ beta particle sources will be placed at varying distances from the detector. The total system efficiency will be determined for each beta spectrum. Filter paper mixed sources will also be placed at varying distances from the detector. System response to varying count rates of beta particles and gamma-rays will be analyzed. Measurements and calculations will be carried out using the setup and equations found in the preceding section.

3.5.3 Effective Range of Measurement

ANSI requires that detector systems be able to measure gamma-ray radiation between 50 keV and 3000 keV. Characteristic x-rays from a ^{133}Ba source (30 to 34 keV) will be used to demonstrate the detector's ability to measure energies below 50 keV. A specially prepared sodium-chloride source will provide high-energy gamma-rays from ^{24}Na (2754 keV) and was only used for this test. A gamma-ray source of higher energy could not be obtained during this study. However, 2753 keV is sufficiently high to demonstrate the detection systems capabilities.

3.5.4 Resolution by Energy

Resolution is defined as the full-energy width at half of the peak's maximum height (FWHM) divided by the central energy (H_o or *centroid*) (Knoll 2000). Figure 3-19 illustrates how resolution is determined (Knoll 2000).

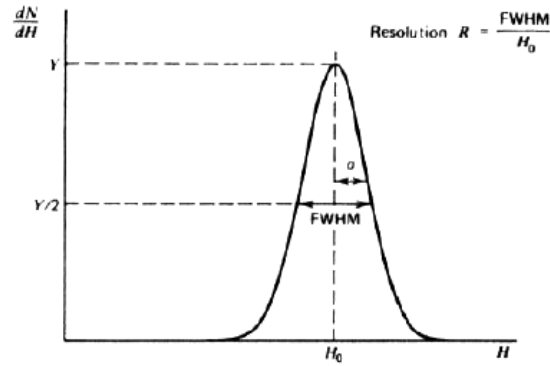


Figure 3-19: Representation of a full-energy-peak resolution calculation (taken from Knoll 2000)

ANSI requires that the maximum full-energy-peak resolution of ^{137}Cs (662 keV) be posted by the manufacturer. In addition the resolution of ^{57}Co (122 keV), ^{133}Ba (356 keV), and ^{60}Co (1173 and 1332 keV) will be provided to determine detector resolution across a range of energies. Radiation sources will be placed 5 cm away from, and on axis with, the detector window. The FWHM will be determined by linear interpolation between energy bins.

3.5.5 Minimum Detectable Activity

The Currie Equation was derived to provide a yes or no decision to whether a sample contains radioactivity (Knoll 2000). The Currie Equation determines the minimum number of counts (N_D) required ensuring, with 95% confidence, that activity was present (Knoll 2000). N_D is defined by,

$$N_D = 4.653\sigma_{BG} + 2.706 \quad (3.6)$$

where σ_{BG} is the standard deviation of the background in a given amount of time. N_D may be converted into a minimum detectable activity (MDA) by:

$$\text{activity} = \frac{N_D}{(\text{yield})(\text{absolute efficiency})(\text{counting time})} \quad (3.7)$$

The MDA will be determined for the testing phase detection system configuration. The N_D and minimum detectable activity will be determined for each full-energy-peak and beta particle spectra found in Table 3-5.

3.5.6 Pulse Discrimination Time

Pulse discrimination algorithms are integral to digital detection systems. Where they are implemented drastically affects performance of the system. Currently there are three implementation scenarios:

1. Pulse discrimination algorithm is carried out on a PC as a post-processing step.
2. Pulse discrimination algorithm is carried out on a PC in real time.
3. Pulse discrimination algorithm is carried out directly on the DPP and only critical information is sent to a GUI.

In all three scenarios, pulses still must satisfy trigger logic prior to the pulse discrimination algorithm. The total processing time for different detection system configurations, to include algorithm processing time, data transfer time, and other bottlenecks will be analyzed. Maximum detectable count rate will be established for the different configurations.

3.5.7 Digital Pulse Processor Programming Time

ANSI requires that a detection system be operational within 2 minutes of start-up. With digital detection systems, there is a period of time before the system is capable of operating, while the DPP is being loaded or directories mapped. However, this time varies with different configurations. Unlike the three configurations outlined in the previous section, programming time occurs one time. Currently, three programming configurations exist:

1. The algorithm is preloaded onto the DPP and only GUI needs to be activated.
2. The algorithm needs to be loaded onto the DPP from external software.
3. The algorithm needs to be loaded onto the DPP and steps also are required.

Two variations of DPP module will be analyzed; the current DPP 2.0 board and a new model from Avicenna Instruments (RX1200⁶). Programming time will be determined for different detection system configurations so that a range of 'warm-up' times is established.

⁶ Avicenna Instruments LLC, 3470 NW Circle Blvd., Corvallis, OR 97330

4 Results

4.1 System Efficiency with Varying Energy

Table 4-1 lists the complete detection system absolute and intrinsic full-energy-peak efficiency for multiple sealed button sources. The button sources were shrouded in beta-particle shielding material. The absolute and intrinsic efficiency for pure beta particle emitting radionuclides with known transmission yields are given in Table 4-2. Efficiency calculations incorporate the full beta particle energy distribution (from β_{\max} to zero) for each radionuclide. Table 4-3 lists absolute and intrinsic efficiency for both full-energy-peak and beta particle distributions from mixed source filter standards. All measurements were taken with sources on axis and 5 cm from the phoswich window.

Table 4-1: Absolute and intrinsic full-energy-peak efficiencies for gamma-ray interaction in the NaI(Tl) layer, measured at 5 cm from the phoswich window

Source	Emission Rate (Bq)	Full-Energy Peak (keV)	Time (s)	Net Peak Counts	Net Peak CPS*	Abs. Peak Eff.*	Int. Peak Eff.*
⁵⁷ Co	53.74	122	2501	3232	1.29	2.405%	63.5%
¹³³ Ba	14969	356	326	8607	26.40	0.176%	4.66%
¹³⁷ Cs	26922	662	410	13204	32.20	0.120%	3.16%
⁶⁰ Co	28798	1173	292	3122	10.69	0.037%	0.98%
		1332		2940	10.07	0.035%	0.92%

*Note: Peak CPS, absolute, and intrinsic efficiency errors less than 4%

Table 4-2: Absolute and intrinsic efficiencies for beta particle interactions in BC400 + CaF₂(Eu) layers, measured at 5 cm from the phoswich window

Source	Emission Rate (Bq)	B _{max} (keV)	Time (s)	β Counts	Net β CPS*	Abs. Eff.*	Int. Peak Eff.*
¹⁴ C	369926	156	216	64188	297.01	0.08%	1.48%
³⁶ Cl	695	709	1253	25664	20.26	2.91%	54.6%
⁹⁰ Sr/ ⁹⁰ Y	606	2280	1136	21628	18.81	3.11%	58.2%

*Note: β CPS, absolute, and intrinsic efficiency errors less than 1%

Table 4-3: Absolute and intrinsic efficiencies for beta particles in BC400 + CaF2(Eu) layers from ^{14}C (156 keV), ^{137}Cs (514 keV), and $^{90}\text{Sr}/^{90}\text{Y}$ (2280 keV) and absolute and intrinsic full-energy-peak efficiencies for gamma-rays in NaI(Tl) from ^{137}Cs (662 keV)

Source	Emission Rates (Bq)	Time (s)	Net Peak γ Counts	Abs. Peak Eff.*	Int. Peak Eff.*	β Counts	Abs. Eff.*	Int. Eff.*
Sample 1	4092 γ / 6285 β	405	2881	0.174%	4.89%	34703	1.36%	26.7%
Sample 10	2423 γ / 3512 β	683	2754	0.166%	4.68%	30907	1.28%	25.2%
Sample 11	2423 γ / 4624 β	656	2892	0.182%	5.12%	31598	1.04%	20.4%

*Note: Absolute and intrinsic efficiency errors less than 1%

4.2 System Efficiency with Varying Count Rate

Tables 4-4, 4-5, and 4-6 provide the absolute and intrinsic full-energy-peak efficiencies of the complete detector system from sealed, and beta-particle shielded, button sources placed at varying distances from the phoswich window. Likewise, Tables 4-7, 4-8, and 4-9 show the absolute and intrinsic efficiencies from pure beta particle emitting sources placed at varying distances from the phoswich window. Tables 4-10, 4-11, and 4-12 list intrinsic full-energy-peak efficiencies and intrinsic beta particle efficiency for mixed radiation sources at varying distances from the phoswich window.

Table 4-4: Absolute and intrinsic full-energy-peak efficiencies with varying distance from the phoswich window from a beta particle shielded 0.855 μCi ^{137}Cs (662 keV) button source

Distance (cm)	Real Time (s)	Gross γ Counts	Net Peak Counts	Peak γ CPS*	Abs. Peak Eff.*	Int. Peak Eff.*
2.5	323	47847	12439	38.5	0.147%	1.64%
5	411	50807	13296	32.4	0.120%	3.16%
10	594	51536	12034	20.3	0.072%	5.78%
15	834	52371	9993	12.0	0.045%	7.41%
20	1065	52891	8132	7.6	0.028%	7.95%

*Note: Peak CPS, Absolute and Intrinsic efficiency errors less than 1%

Table 4-5: Absolute and intrinsic full-energy-peak efficiencies with varying distance from the phoswich window from a beta particle shielded 0.78 μCi ^{60}Co (1173 keV) button source

Distance (cm)	Real Time (s)	Gross γ Counts	Net Peak Counts	Peak γ CPS*	Abs. Peak Eff.*	Int. Peak Eff.*
2.5	251	43731	3107	12.4	0.043%	0.48%
5	289	47434	3277	11.3	0.037%	0.98%
10	403	49987	3234	8.0	0.029%	2.29%
15	559	51339	2672	4.8	0.017%	2.73%
20	718	51909	2626	3.7	0.013%	3.56%

*Note: Peak CPS, Absolute and Intrinsic efficiency errors less than 1%

Table 4-6: Absolute and intrinsic full-energy-peak efficiencies with varying distance from the phoswich window from a beta particle shielded 0.78 μCi ^{60}Co (1332 keV) button source

Distance (cm)	Real Time (s)	Gross γ Counts	Net Peak Counts	Peak γ CPS*	Abs. Peak Eff.*	Int. Peak Eff.*
2.5	251	43731	2538	10.1	0.035%	0.39%
5	289	47434	3078	10.7	0.035%	0.92%
10	403	49987	2861	7.1	0.025%	1.97%
15	559	51339	2620	4.7	0.016%	2.68%
20	718	51909	2457	3.4	0.012%	3.33%

*Note: Peak CPS, Absolute and Intrinsic efficiency errors less than 1%

Table 4-7: Absolute and intrinsic efficiencies with varying distance from the phoswich window from a 10 μCi ^{14}C (156 keV) foil source

Distance (cm)	Real Time (s)	β Counts	Net β CPS*	Abs. Eff.*	Int. Eff.*
1	216	64649	299.15	0.08%	0.26%
2.5	208	64591	310.38	0.08%	0.56%
5	216	64188	297.01	0.08%	1.48%
7.5	307	62571	203.66	0.06%	2.08%
10	618	57632	93.10	0.03%	1.64%

*Note: β CPS, Absolute, and Intrinsic efficiency errors less than 1%

Table 4-8: Absolute and intrinsic efficiencies with varying distance from the phoswich window from a 0.0188 μCi ^{36}Cl (708 keV) foil source

Distance (cm)	Real Time (s)	β Counts	Net β CPS*	Abs. Eff.*	Int. Eff.*
1	451	44687	98.86	14.2%	44.9%
2.5	728	38346	52.44	7.54%	50.3%
5	1253	25664	20.26	2.91%	54.6%
7.5	1615	17745	10.76	1.55%	59.2%
10	1881	12419	6.38	0.92%	60.1%

*Note: β CPS, Absolute, and Intrinsic efficiency errors less than 1%

Table 4-9: Absolute and intrinsic efficiencies with varying distance from the phoswich window from a 0.0164 μCi $^{90}\text{Sr}/^{90}\text{Y}$ (2280 keV) foil source

Distance (cm)	Real Time (s)	β Counts	Net β CPS*	Abs. Eff.*	Int. Eff.*
1	412	36019	87.20	14.4%	45.5%
2.5	651	30056	45.94	7.59%	50.5%
5	1136	21628	18.81	3.11%	58.2%
7.5	1571	14994	9.32	1.54%	58.9%
10	1797	10723	5.74	0.95%	62.0%

*Note: β CPS, Absolute, and Intrinsic efficiency errors less than 1%

Table 4-10: Absolute and intrinsic full-energy-peak efficiencies for the NaI(Tl) layer, and absolute and intrinsic efficiencies for BC400 + $\text{CaF}_2(\text{Eu})$ layers from a combined activity of 0.33 μCi (0.13 μCi ^{137}Cs , 0.02 μCi ^{14}C , 0.018 μCi $^{90}\text{Sr}/^{90}\text{Y}$) from filter paper source (Sample 1)

Distance (cm)	Real Time (s)	γ Counts	Net Peak γ Counts	Abs. Peak Eff.*	Int. Peak Eff.*	β Counts	Abs. Eff.*	Int. Eff.*
1	238	8707	2298	0.24%	1.33%	41291	2.76%	8.70%
2.5	285	10111	2450	0.21%	2.34%	39135	2.18%	14.6%
5	405	14399	2881	0.17%	4.89%	34703	1.36%	26.7%
7.5	588	19416	3044	0.13%	6.53%	30108	0.81%	32.4%
10	793	24431	3247	0.10%	8.27%	25703	0.51%	34.5%
15	1184	33313	2739	0.06%	9.47%	18082	0.24%	34.8%

*Note: Absolute, and Intrinsic efficiency errors less than 1.5%

Table 4-11: Absolute and intrinsic full-energy-peak efficiencies for the NaI(Tl), and absolute and intrinsic efficiencies for BC400 + CaF₂(Eu) layers from a combined activity of 0.095 μ Ci (0.077 μ Ci ¹³⁷Cs, 0.018 μ Ci ⁹⁰Sr/⁹⁰Y) from filter paper source (Sample 10)

Distance (cm)	Real Time (s)	γ Counts	Net Peak γ Counts	Abs. Peak Eff.	Int. Peak Eff.	β Counts	Abs. Eff.	Int. Eff.
1	300	9980	2218	0.31%	1.72%	41158	3.90%	12.3%
2.5	400	12651	2324	0.24%	2.67%	37825	2.69%	18.0%
5	683	19718	2754	0.17%	4.68%	30907	1.28%	25.2%
7.5	950	26274	2496	0.11%	5.60%	24747	0.74%	29.4%
10	1275	33175	2183	0.07%	5.84%	18730	0.41%	27.8%
15	1636	41515	1709	0.04%	7.22%	11477	0.19%	28.1%

*Note: Absolute, and Intrinsic efficiency errors less than 1.5%

Table 4-12: Absolute and intrinsic full-energy-peak efficiencies for the NaI(Tl), and absolute and intrinsic efficiencies for BC400 + CaF₂(Eu) from a combined activity of 0.125 μ Ci (0.077 μ Ci ¹³⁷Cs, 0.048 μ Ci ¹⁴C) from filter paper source (Sample 11)

Distance (cm)	Real Time (s)	γ Counts	Net PP γ Counts	Abs. Peak Eff.	Int. Peak Eff.	β Counts	Abs. Eff.	Int. Eff.
1	309	9960	2226	0.30%	1.68%	41623	2.91%	9.20%
2.5	415	13322	2324	0.23%	2.58%	37564	1.95%	13.1%
5	656	19364	2892	0.18%	5.12%	31598	1.04%	20.4%
7.5	975	26867	2689	0.11%	5.88%	24665	0.54%	21.7%
10	1261	33164	2525	0.08%	6.82%	19059	0.32%	21.8%
15	1633	41488	1651	0.04%	6.99%	11563	0.15%	21.8%

*Note: Absolute, and Intrinsic efficiency errors less than 1.5%

4.3 Effective Range of Measurement

Figure 4-1 is the photon energy spectrum produced by ¹³³Ba. Figure 4-2 is the photon spectrum produced by ²⁴Na and ³⁸Cl. The two spectra illustrate the detection system's sensitivity to photons below 50 keV and up to 3000 keV.

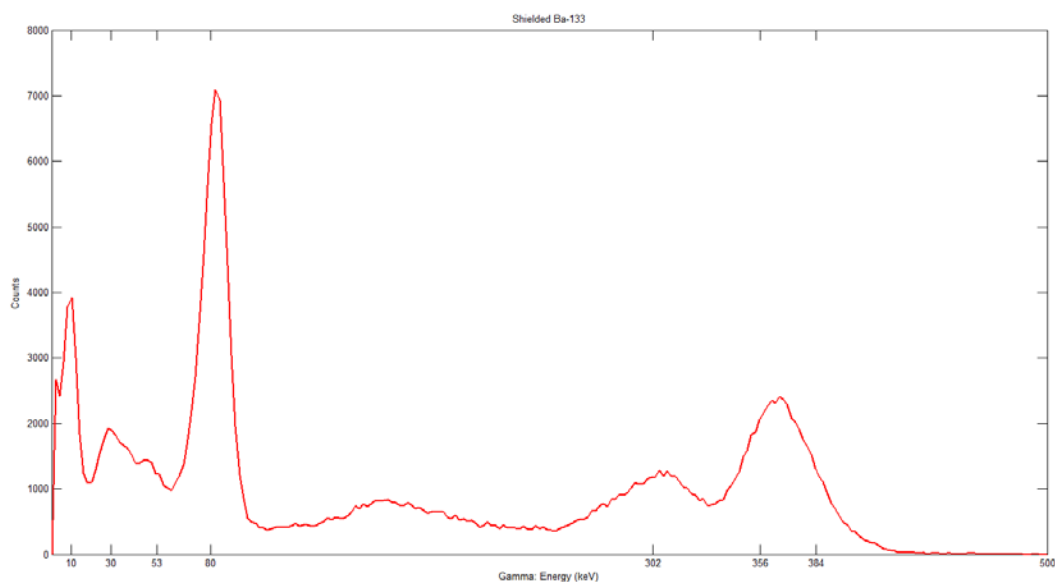


Figure 4-1: Gamma-ray and x-ray spectrum from ^{133}Ba . X-axis demarcations 384, 356, 302, 80, and 53 keV are known gamma-ray energies from ^{133}Ba . More feature details are identified in section 5.3.

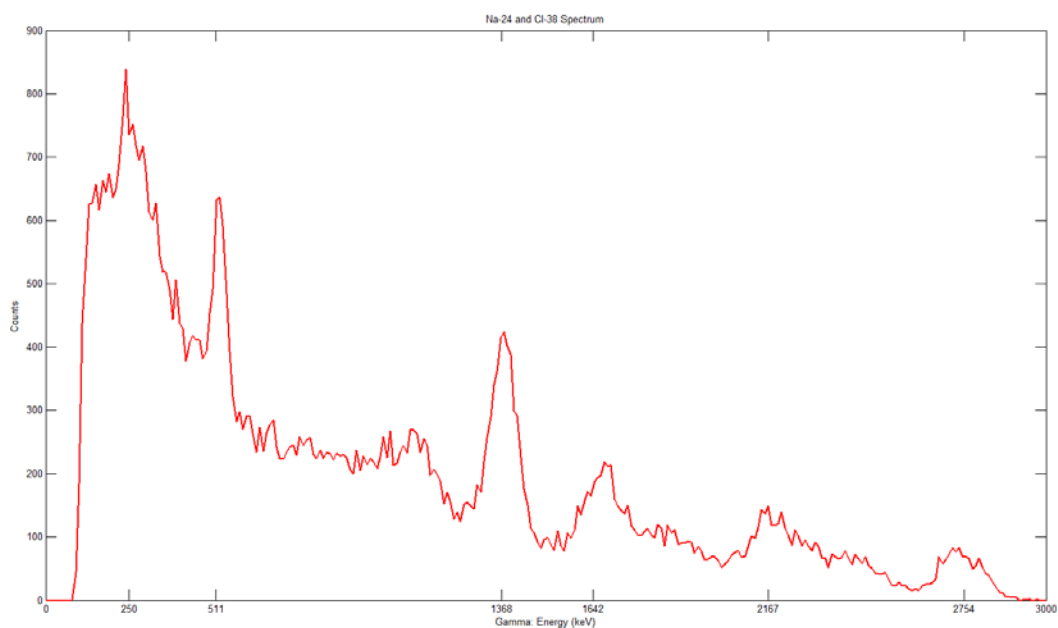


Figure 4-2: Gamma-ray spectrum from ^{24}Na and ^{38}Cl . X-axis demarcations 2754 and 1368 keV are known gamma-rays from ^{24}Na . X-axis demarcations 2167 and 1642 keV are known gamma-rays from ^{38}Cl . 511 keV is the annihilation peak produced from pair production. 250 keV peak is the maximum backscatter peak.

4.4 Resolution by Energy

Full-energy-peak resolution for five gamma-rays is shown in Table 4-13. All measurements were taken with beta shielded, sealed button sources, placed on axis and 5 cm from the phoswich window.

Table 4-13: Gamma-ray resolution in the NaI(Tl) layer by energy, measured 5 cm from the phoswich window

Source	Full-Energy-Peak (keV)	Interp. FWHM (keV)	Resolution
⁵⁷ Co	122	47.5	33.28%
¹³³ Ba	356	42.7	12.07%
¹³⁷ Cs	662	52.2	7.99%
⁶⁰ Co	1173	79.7	6.89%
	1332	82.3	6.29%

4.5 Minimum Detectable Activity

The calculated minimum detectable activity resulting in 95% confidence that radioactivity is present during a single 65,000 pulse collection period for gamma-rays and beta particles is provided in Table 4-14. The minimum detectable activity is calculated for the time interval covered while collecting the pulses (2579 seconds). The reason for this specific counting period is discussed in section 5.1. The MDA was calculated from background measurements in the region of interest around each full-energy-peak or beta particle energy distribution.

Table 4-14: Minimum Detectable Activity around specified regions of interest, taken for 65,000 counts over a span of 2579 seconds

Source	Energy (keV)	Background Counts	N _b (counts)	MDA (Bq)
⁵⁷ Co	122	15233	1543	52.42
¹³³ Ba	356	3608	1075	68.77
¹³⁷ Cs	662	183	906	107.60
⁶⁰ Co	1173	743	618	48.62
	1332	450	504	39.63
¹⁴ C	156	467	440	212.30
³⁶ Cl	709	577	705	9.54
⁹⁰ Sr/ ⁹⁰ Y	2280	591	970	7.72

4.6 Pulse Discrimination Time

The theoretical maximum time required to perform pulse discrimination on a single pulse is calculated relative to potential bottle-neck points for two different DPP 2.0 scenarios. Additionally, the maximum number of pulses that can be processed in one second is measured. An RX1200 was also analyzed to provide a comparison between DPP algorithm implementation techniques. The results are tabulated in Table 4-15.

Table 4-15: Theoretical and measured pulse discrimination time, data transfer time and overall maximum pulse collection rate for different algorithm implementation scenarios

Algorithm Implementation	Clock Speed (MHz)	Pulse Length (ns)	USB Transfer Time (μs)	Algorithm Run Time (per pulse)	Total Software Overhead	Maximum CPS Processed	Limiting Point
<u>DPP 2.0</u>							
Post-Processing	200	5120	0.341*	N/A	3.19 ms	310	Software
MATLAB†	200	5120	0.341*	35.2 ms	38.6 ms	26	MATLAB
<u>RX1200</u>							
MCA Mode	100	5000	273*	600 ns	N/A	1.78E5*	User Defined

*Note: Theoretical calculation

†Note: Real time algorithm calculation and histogram update

4.7 Digital Pulse Processor Programming Time

Digital pulse processor programming or initialization times were measured using MATLAB internal timing command, “tic/toc”. Tic/Toc was specifically designed to measure the time required for individual sections of code to complete their functions. It was found that the DPP 2.0 requires between 61.6 and 211 milliseconds before the detection system is operational based on possible system configurations. An RX1200 DPP was analyzed as a comparison. Programming times for both DPP’s are shown in Table 4-16.

Table 4-16: Maximum detection system initialization time with varying programming configurations

DPP platform	GUI Initiation	Program DPP	Additional Overhead
DPP 2.0	61.6 ms	149 ms	211 ms
RX1200	3.52 ms	88.1 ms	595 ms

5 Discussions

Before analyzing the results from the characterization tests (Sections 3.5 and 4) that were conducted, it is worthwhile to ensure that the detection system is operating as intended. The detection system's ability to separate gamma-rays, beta particles and cross-talk (listed below as noise) are presented in figures 5-1 through 5-10.

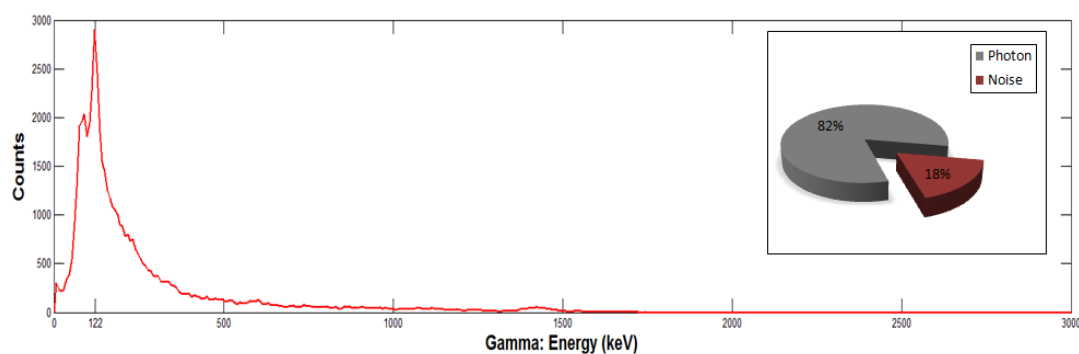


Figure 5-1, Photon spectrum and pulse discrimination level for a beta particle shielded 1.5E-4 μCi ^{57}Co button source, measured 5 cm from the phoswich window

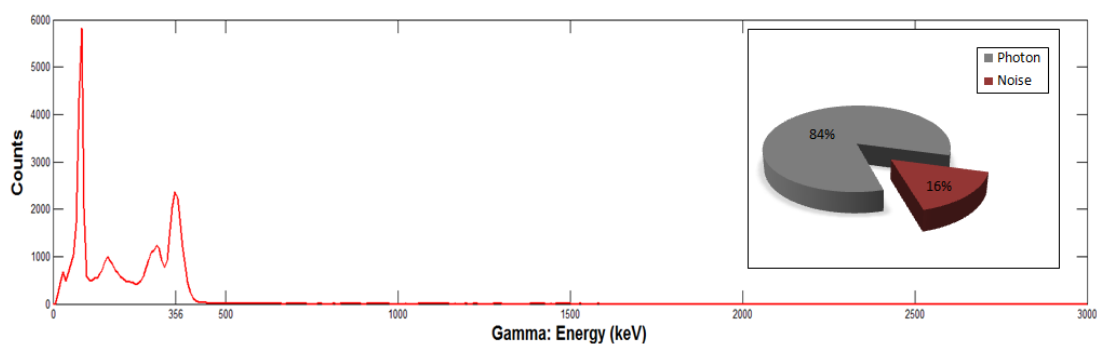


Figure 5-2, Photon spectrum and pulse discrimination level for a beta particle shielded 0.405 μCi ^{133}Ba button source, measured 5 cm from the phoswich window

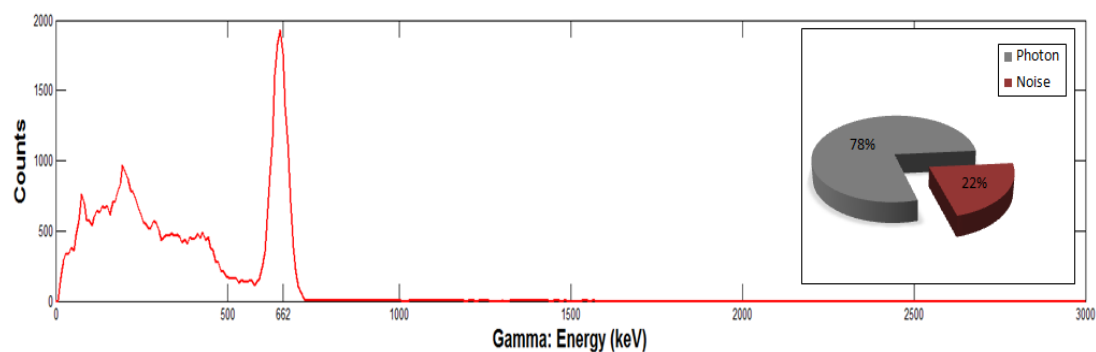


Figure 5-3, Photon spectrum and pulse discrimination level for a beta particle shielded 0.855 μCi ^{137}Cs button source, measured 5 cm from the phoswich window

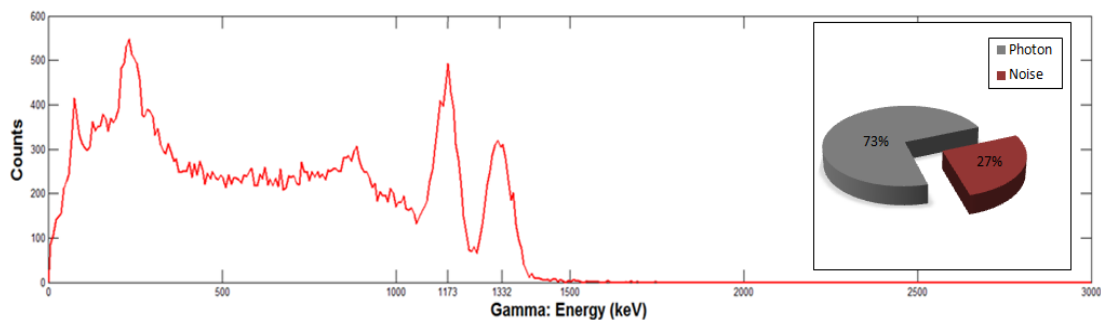


Figure 5-4, Photon spectrum and pulse discrimination level for a beta particle shielded 0.78 μCi ^{60}Co button source, measured 5 cm from the phoswich window

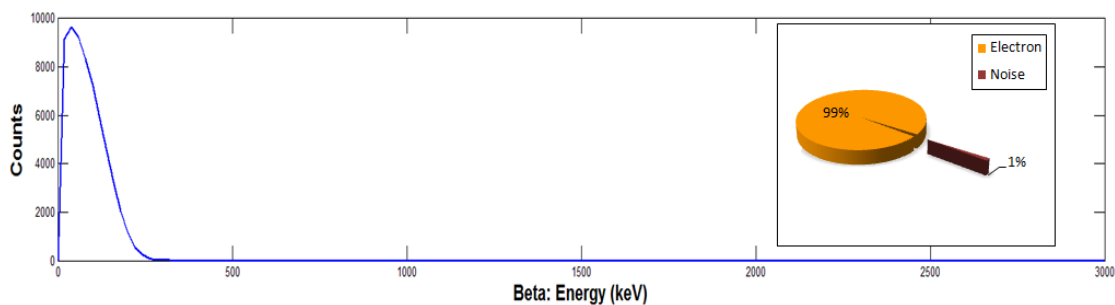


Figure 5-5, Electron spectrum and pulse discrimination level for a 10 μCi ^{14}C foil source, measured 5 cm from the phoswich window

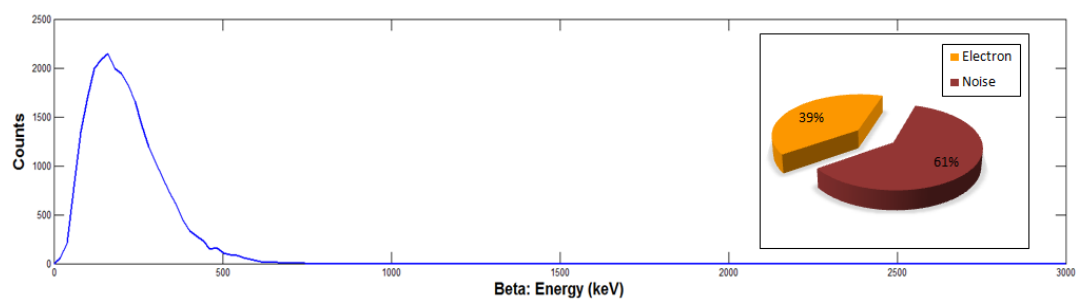


Figure 5-6, Electron spectrum and pulse discrimination level for a 0.0188 μCi ^{36}Cl foil source, measured 5 cm from the phoswich window

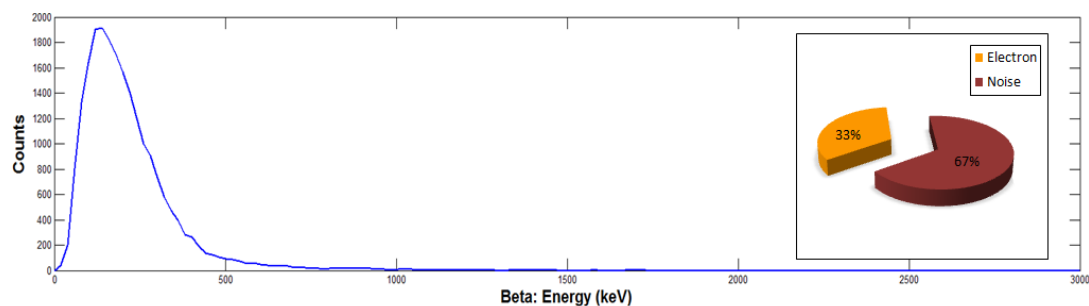


Figure 5-7, Electron spectrum and pulse discrimination level for a 0.0164 μCi $^{90}\text{Sr}/^{90}\text{Y}$ foil source, measured 5 cm from the phoswich window

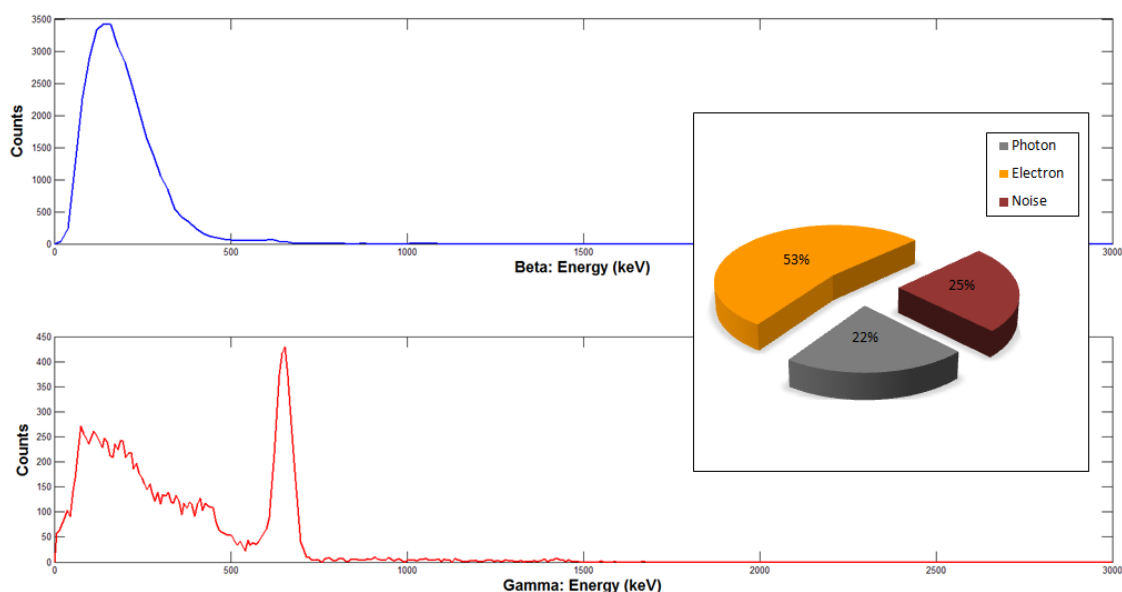


Figure 5-8, Gamma-ray and beta particle spectra and pulse discrimination level from a mixed radiation field consisting of 0.13 μCi ^{137}Cs , 0.02 μCi ^{14}C and 0.018 μCi $^{90}\text{Sr}/^{90}\text{Y}$ from a filter paper source (Sample 1), measured 5 cm from the phoswich window

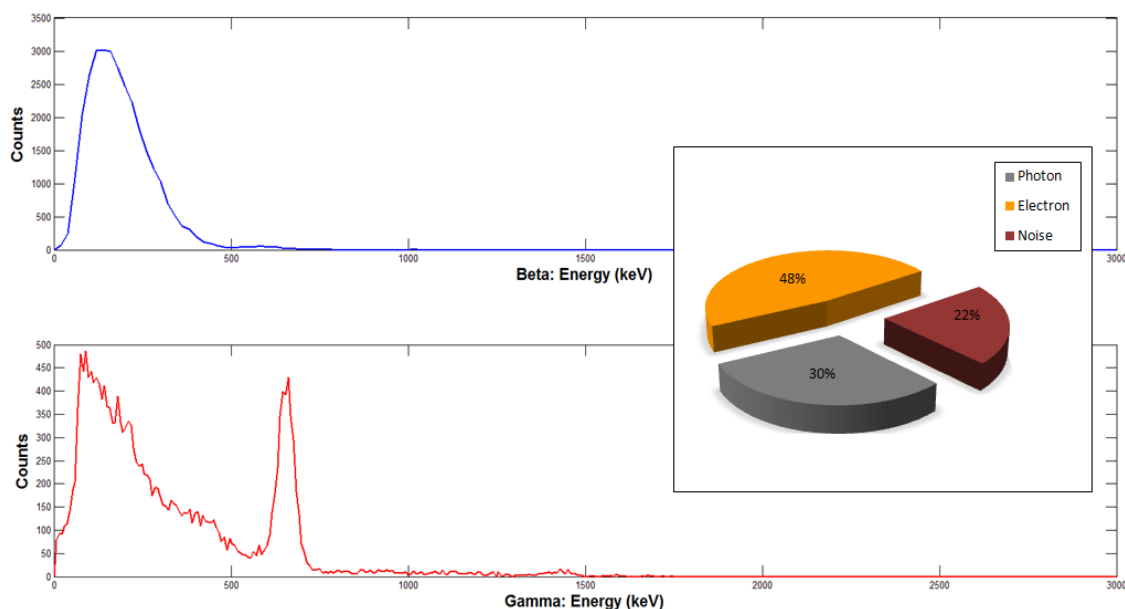


Figure 5-9, Gamma-ray and beta particle spectra and pulse discrimination level from a mixed radiation field consisting of 0.077 μCi ^{137}Cs and 0.018 μCi $^{90}\text{Sr}/^{90}\text{Y}$ from a filter paper source (Sample 10), measured 5 cm from the detector window

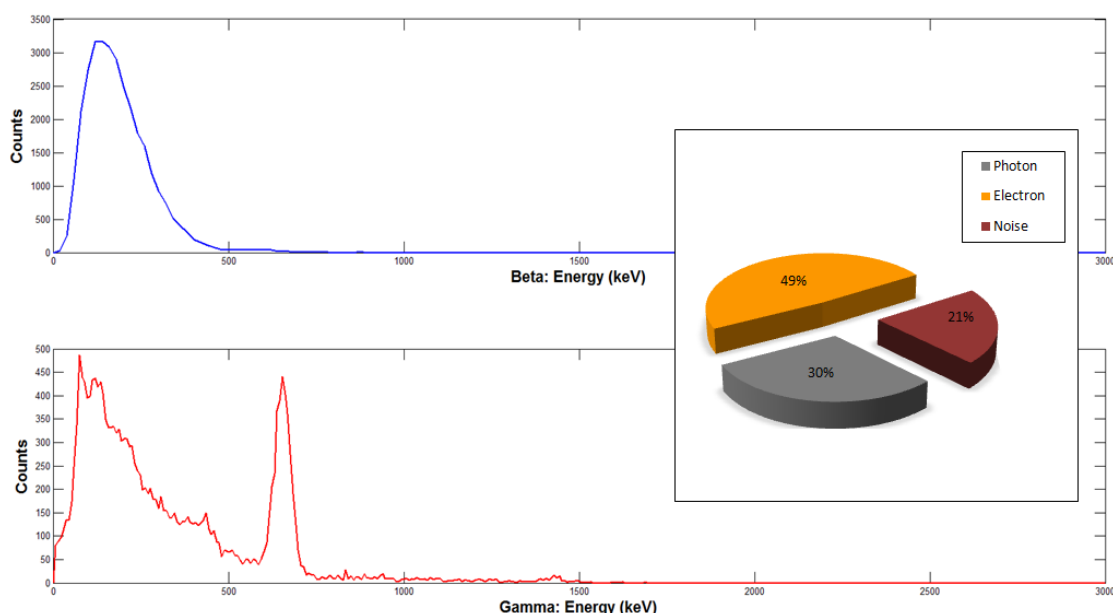


Figure 5-10, Gamma-ray and beta particle spectra and pulse discrimination level from a mixed radiation field consisting of 0.077 μCi ^{137}Cs and 0.048 μCi ^{14}C from a filter paper source (Sample 11), measured 5 cm from the detector window

The above illustrations clearly demonstrate that the detection system is accurately discriminating between the types of interacting radiation, accurately quantifying the energy deposited, and rejecting cross-talk events. The noise depicted in figures 5-1 through 5-4 are gamma-rays that interacted with the $\text{CaF}_2(\text{Eu})$ layer and were subsequently rejected from those spectra. The noise depicted in figures 5-5 through 5-7 are background photons or secondary x-rays that were collected in either the $\text{CaF}_2(\text{Eu})$ or $\text{NaI}(\text{Tl})$ layers. This effect is exacerbated with lower activity sources (Figs. 5-6 and 5-7), where longer collection periods allow for an increased influence from background radiation.

Figures 5-8 through 5-11 were produced from the filter paper mixed radionuclide sources (Samples 1, 10 and 11). The ^{137}Cs photon (662 keV) is clearly seen in all samples. There is an increased influence of background photons as the total activities of the filter paper samples are relatively low. Sample 1 has nearly twice the ^{137}Cs activity compared to Samples 10 and 11 (which have the same level of ^{137}Cs activity). The differences are readily apparent in the above spectra. The beta particle spectra are relatively uninspiring, owing largely to the influence of the

emission rate of beta particles from ^{137}Cs over the pure beta particle emitting radionuclides. The noise in these figures is also primarily due to photon interaction in the $\text{CaF}_2(\text{Eu})$ layer.

5.1 System Efficiency with Varying Energy

Scintillation detector efficiency is heavily dependent on design parameters (Knoll 2000). All scintillating material in the studied phoswich is of solid right circular cylinder shape. There are a few key variables that must be considered when analyzing efficiency of a scintillation based detector. First, absolute efficiency is greatly affected by source to detector spacing, but intrinsic efficiency is less so (Knoll 2000). The further the source is from the detector, the more statistically stable the absolute efficiency. Second, intrinsic efficiency is most affected by the thickness of the cylinder in the direction of incident radiation (Knoll 2000). Additionally, the physical nature of the source also affects efficiency measurements. Finally, radiation absorption that occurs between the source and detection system should be minimized. For these reasons, it is difficult to compare efficiencies of detection systems.

Efficiency is calculated by equations 3.4 and 3.4, where the number of collected pulses is in the numerator and the number of emitted pulses (during the same time period) is in the denominator. Generally pulses are collected for a defined period of time, which is the converted into a count rate (counts per second or cps). The count rate is then compared with the emission rate of a radioactive source, typically listed in disintegration per second (dps or Bq). There are three important timing metrics that need to be accounted for in any given counting period; real time, dead time, and live time. Real time is defined as the total time required to make a measurement. Live time is a subset of the real time, and is defined as the total amount of time that the detector is available to make a measurement. On the other hand, dead time is the opposite of live time. Dead time is the time where the detector cannot measure incident radiation because the system is busy processing the previous pulse.

When there are few radiation particles incident upon a detector, the real time is roughly equal to the live time as the likelihood of the detector being busy is low. Conversely, when there

are many radiation particles incident upon a detector, the real time may be much longer than the live time because the detector is constantly busy. In other words, there is a greater period of dead time. Radiation events that occur while the system is busy are lost and cannot be accounted for. Efficiency measurements will not be accurate when a detector is exposed to high levels of incident radiation if real time is used to calculate the count rate. For these reason, the count rate during a collection period is ideally based on the live time rather than the real time.

However, the phoswich detection system in the studied configuration was only able to record the real time of a collection period. Attempts to correct for dead time proved unreliable. As a result, this study discovered that there were two major issues affecting the phoswich detection system's count rate. The first and most significant of these issues is where the pulse discrimination algorithm is implemented. The maximum count rate that could be achieved in this study was only 310 counts per second. Sources with even a moderate level of activity (1 μCi) yield by far more disintegrations per second (37,000 Bq). The result is an artificially low absolute efficiency, which cannot be satisfactorily converted into intrinsic efficiency. The influence count rate has on efficiency is demonstrated in the following graphs (Fig. 5-12 through 5-23).

The second issues was dubbed, 'm number' effect. It was discovered that a variable in the primary 'while' loop of the MATLAB code affected the maximum count rate of the detection system. The variable was labeled 'm' in the MATLAB code and corresponds to the number of valid pulses the detection system was required to count in a given collection period. The larger the 'm number' assigned, the slower the detection system operated. This was a result of the software having to run the while loop at the end of each valid pulse to determine if the collection period was complete. The count rate was monitored with varying 'm number' (Fig. 5-11). From this data an 'm number' of 65000 provided statistically sufficient counts inside full-energy-peaks with little loss in count rate. The 'm number' was fixed to 65000 for all efficiency measurements to minimize software variation of counting statistics between the different sources.

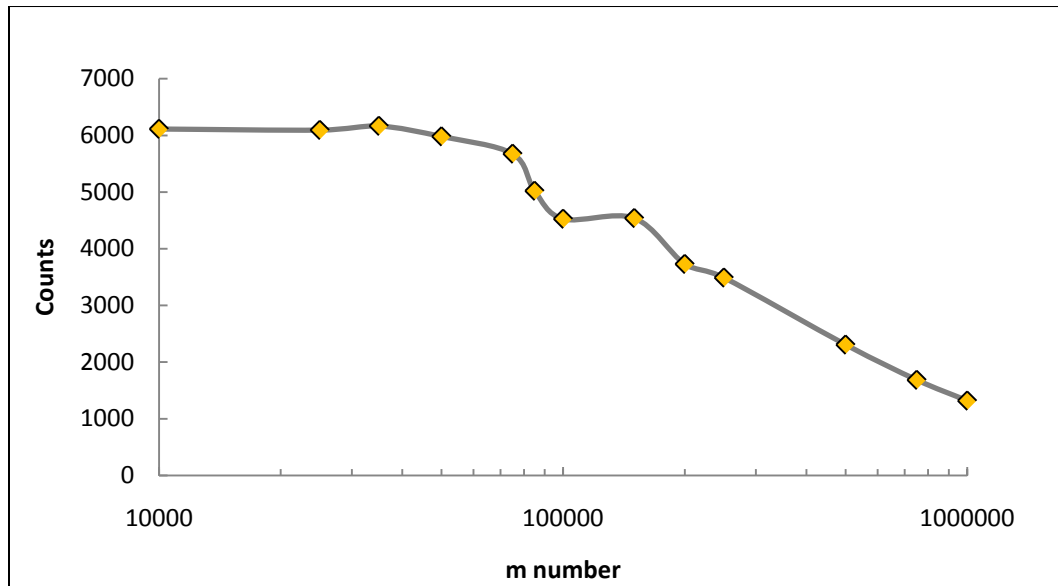


Figure 5-11: m number effect on the maximum number of counts collected in a 5 minute period

The measured NaI(Tl) efficiencies (Table 4-1) were paired with an MCNP simulation. The MCNP simulation modeled intrinsic efficiency, since the source was placed onto the window of the detector and only full-energy-peak interactions were recorded. Figure 5-12 shows the measured intrinsic and absolute full-energy-peak efficiencies along with the MCNP simulation results, and reproduced data from Evans et al. (1980).

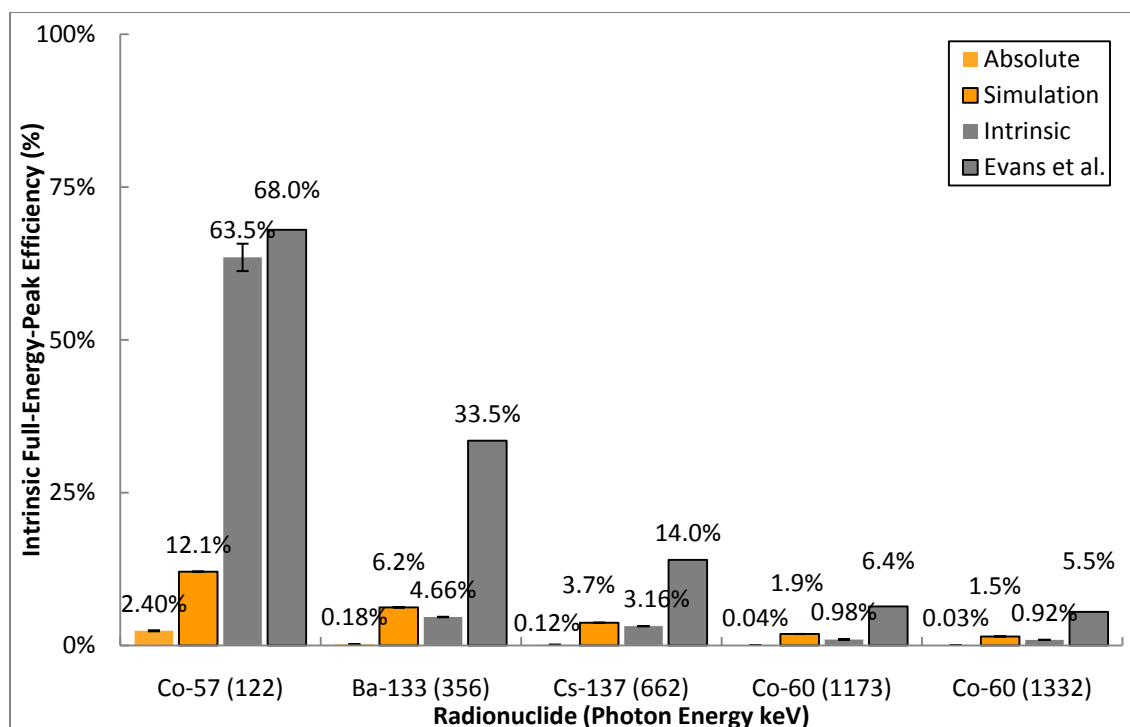


Figure 5-12: Measured and simulated full-energy-peak efficiencies in NaI(Tl) for ^{57}Co (122 keV), ^{133}Ba (356 keV), ^{137}Cs (662 keV), and ^{60}Co (1173 and 1332 keV), error is included per data point

Evans et al. (1980) measured the efficiency of right cylindrical NaI(Tl) crystal (3.8 cm x 3.8 cm dimensions) and found full-energy-peak intrinsic efficiencies of 68, 33.5, 14, 6.4, and 5.5 percent for ^{57}Co (122 keV), ^{133}Ba (356 keV), ^{137}Cs (662 keV), and ^{60}Co (1173 and 1332 keV), respectively. Hartwell et al. (2004) measured the efficiency of an identically sized NaI(Tl) crystal for ^{137}Cs (662 keV) and ^{60}Co (1332 keV) at 10 cm. He found full-energy absolute efficiencies of 0.043 and 0.0144 percent, respectively. Absolute efficiency for the studied detection system, measured at 10 cm, was found to be 0.0722 and 0.0247 percent for ^{137}Cs and ^{60}Co , respectively.

Hartwell et al. and Evans et al. reported values are representative, yet cannot be used as direct comparison since these were measurements of a single NaI(Tl) crystal rather than a multi-layer phoswich. The MCNP simulation provides a more comparable metric. The MCNP determined intrinsic full-energy-peak efficiency and that measured are in very close agreement, save for that measured from ^{57}Co (122 keV), which is more in line with values reported by Evans

et al. (1980). In general these values are in relative agreement with each other and differences are most likely owing to the key factors described above.

All beta particle efficiencies were expected to be quite good, due to the linear stopping power in the combined BC400 and $\text{CaF}_2(\text{Eu})$ layers. Figure 5-13 illustrates the measured efficiencies. It was observed that low activity and higher-energy beta particle sources produced better efficiencies. The count rate issues alluded to above are acutely observed with ^{14}C . The ^{14}C source used had an activity of 10 μCi (302k Bq) and the highest theoretical absolute efficiency measurement possible was 0.1 percent based on the count rate limitation. A lower activity ^{14}C source was not available for additional testing.

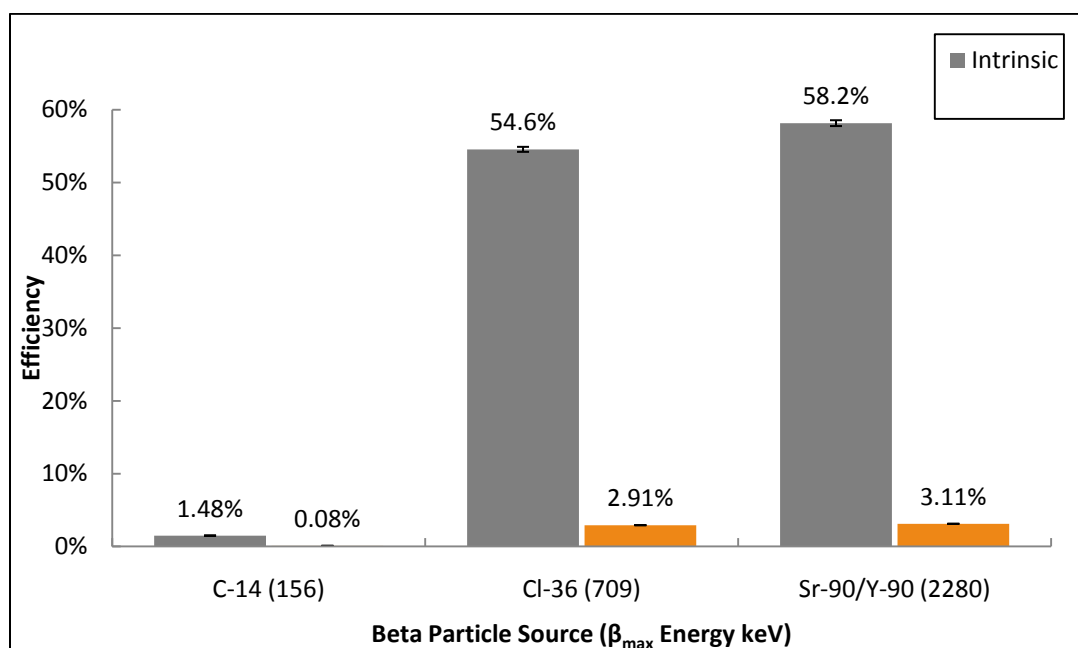


Figure 5-13: Measured efficiencies in BC400 + $\text{CaF}_2(\text{Eu})$ layers for ^{14}C (156 keV), ^{36}Cl (709 keV), and $^{90}\text{Sr}/^{90}\text{Y}$ (2280 keV), error is included per data point

Mixed source efficiency at 5 centimeters from the phoswich window demonstrated the detection systems ability to measure beta particles and gamma-rays from a mixed radiation field. The effect of count rate is again apparent (Fig. 5-14). The mixed ^{137}Cs activities were much lower than the button source and an increased efficiency was measured. Likewise, the beta

particle activity was increased compared to the foil sources and a lower efficiency was measured.

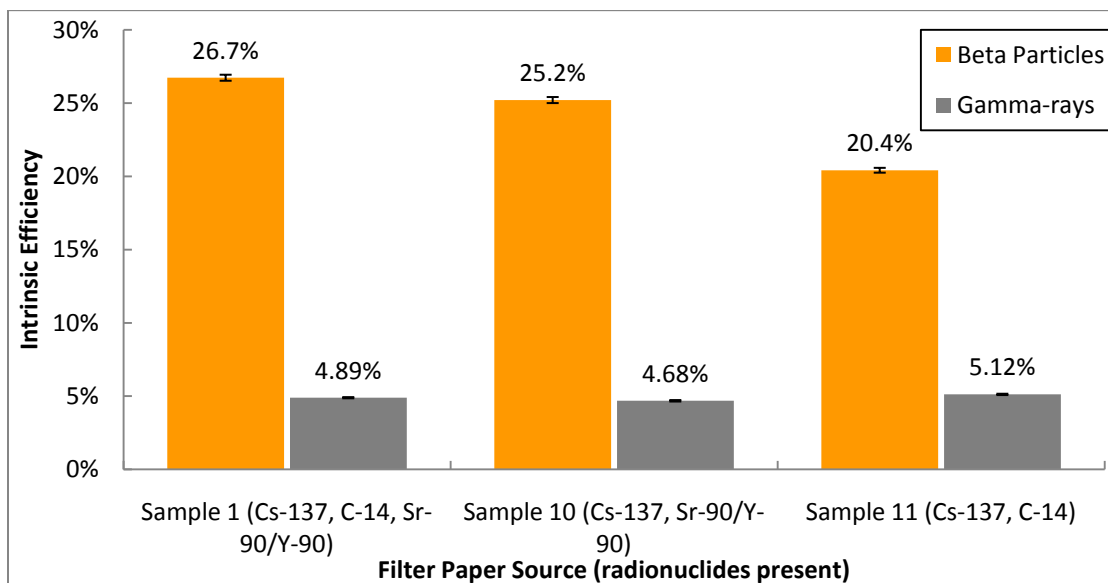


Figure 5-14: Measured intrinsic efficiencies for beta particles in BC400 + CaF₂(Eu) layers for ¹⁴C (156 keV) and ⁹⁰Sr/⁹⁰Y (2280 keV) and intrinsic full-energy-peak efficiency for gamma-rays in NaI(Tl) for ¹³⁷Cs (662 keV), error is included per data point

5.2 System Efficiency with Varying Count Rate

Figure 5-15 depicts the intrinsic full-energy-peak efficiency with varying count rate. This is expected to be a constant since the activity incident upon the detection system has been solid-angle corrected. However, the line has a slope, indicating that something is affecting efficiency. Increased incident activity upon the detector results in a decreased efficiency. Again, it is suspected that the limited count rate relative to the source activity is to blame. In other words, the detection system's dead time is the culprit and the real time cannot accurately be used to measure the incident radiation field.

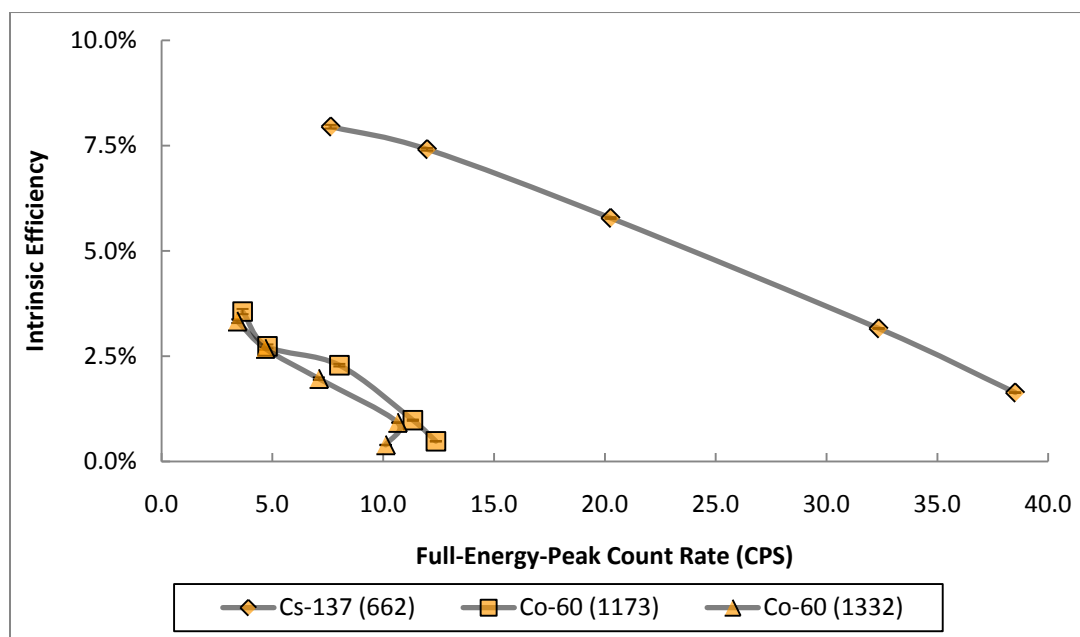


Figure 5-15: Measured intrinsic full-energy-peak efficiencies in the NaI(Tl) layer for ^{137}Cs (662 keV), ^{60}Co (1173 keV), and ^{60}Co (1332 keV) with varying incident count rate, error is included per data point

Figure 5-16 illustrates that at least in the case of 662 keV gamma-rays, there appears to be a plateau forming in the data as the distance between the source and detector increases (or alternatively, the level of activity incident upon the detector decreases). This finding lends some credence to the real time based count rate hypothesis. If the solid angle is the only acting variable on efficiency, then the absolute efficiency should decrease in a $\frac{1}{\text{distance}^2}$ manner. Figure 5-17 clearly illustrates that this is not what has occurred.

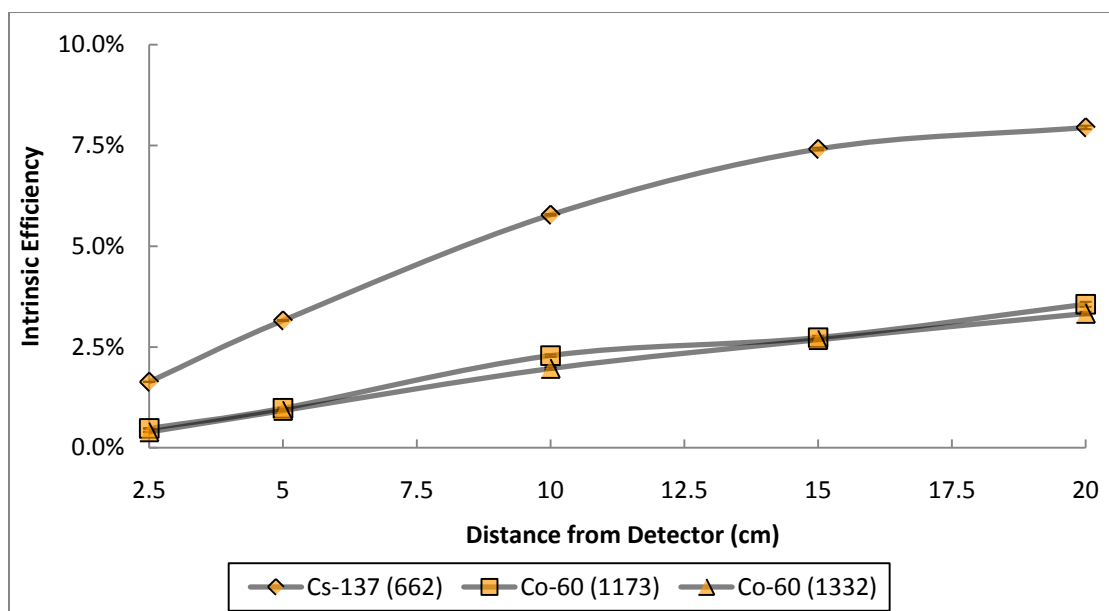


Figure 5-16: Measured intrinsic full-energy-peak efficiencies in the NaI(Tl) layer with varying distance between source and phoswich window, error is included per data point

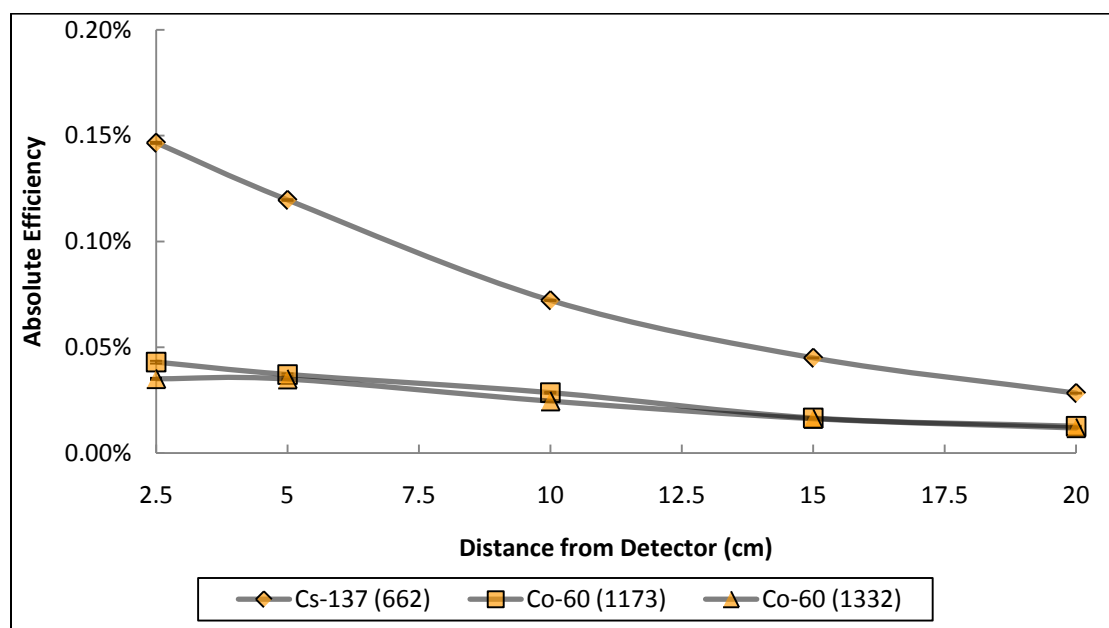


Figure 5-17: Measured absolute full-energy-peak efficiencies in the NaI(Tl) layer with varying distance between source and detector window, error is included per data point

Beta particle efficiency exhibits similar characteristics to what was observed with gamma-ray efficiency. Like the findings in Figure 5-13, ^{14}C efficiency is extremely poor (Fig. 5-18). Figure 5-19 suggests that the lower activity ^{36}Cl sample, and to a lesser extent the $^{90}\text{Sr}/^{90}\text{Y}$ sample, are nearing a plateau at greater distance from the phoswich window. Again, this suggests that at lower count rates the efficiency increases, or conversely, at higher count rates the detection system is experiencing an increase in dead time. Figure 5-20 demonstrates that the absolute efficiency follows the expected decrease in incident activity.

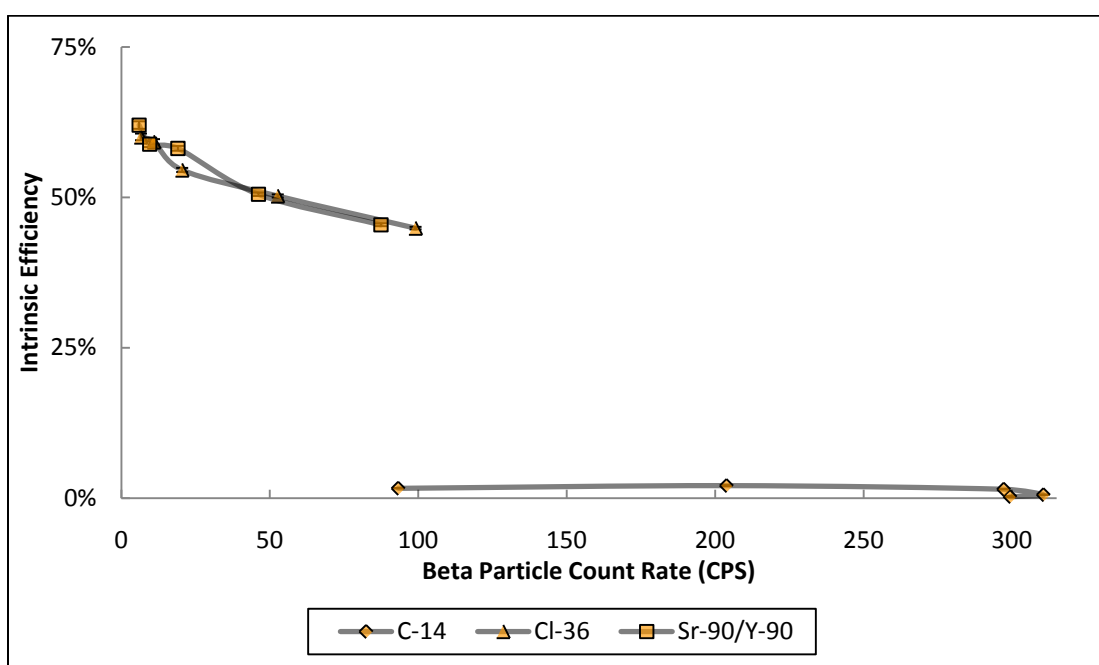


Figure 5-18: Measured beta particle intrinsic efficiencies in BC400 + $\text{CaF}_2(\text{Eu})$ layers with varying incident count rate on the phoswich window, error is included per data point

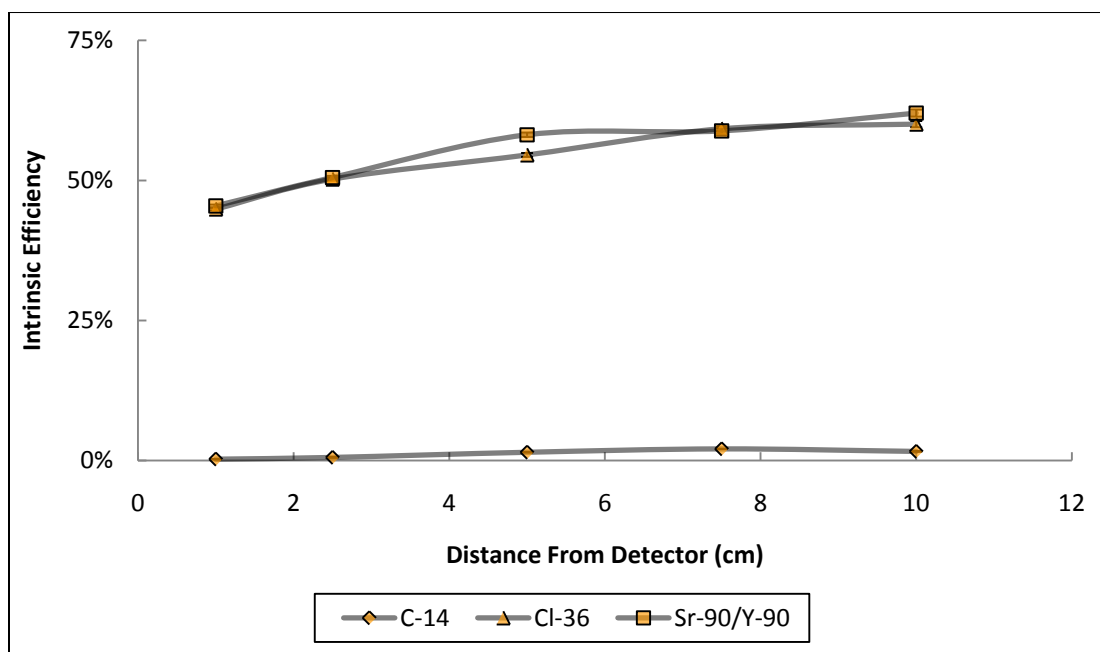


Figure 5-19: Measured intrinsic efficiencies in BC400 + CaF₂(Eu) layers with varying distance between source and phoswich window, error is included per data point

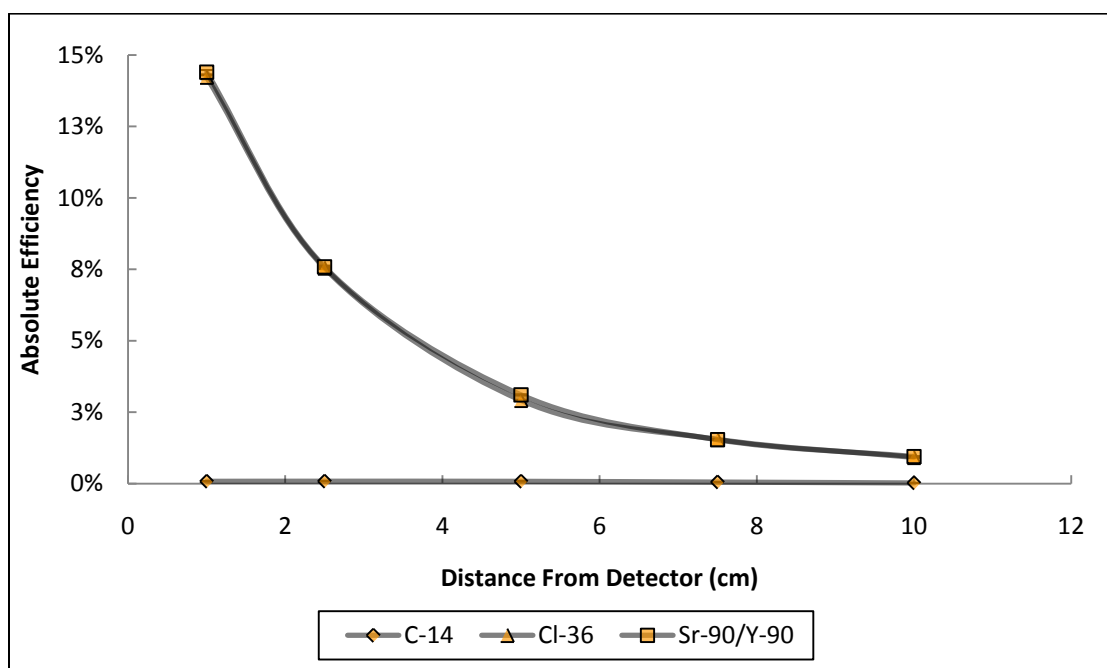


Figure 5-20: Measured absolute efficiencies in BC400 + CaF₂(Eu) layers with varying distance between source and phoswich window, error is included per data point

The mixed samples also display the same count rate issue (Fig. 5-21 and Fig. 5-22). However, owing to the lower emission rates of these sources, a plateau is readily seen (Fig. 5-23). These findings indicate that the detection system, in its present configuration, is experiencing a great deal of dead time with high incident radiation fields and efficiency measurements are not reliable.

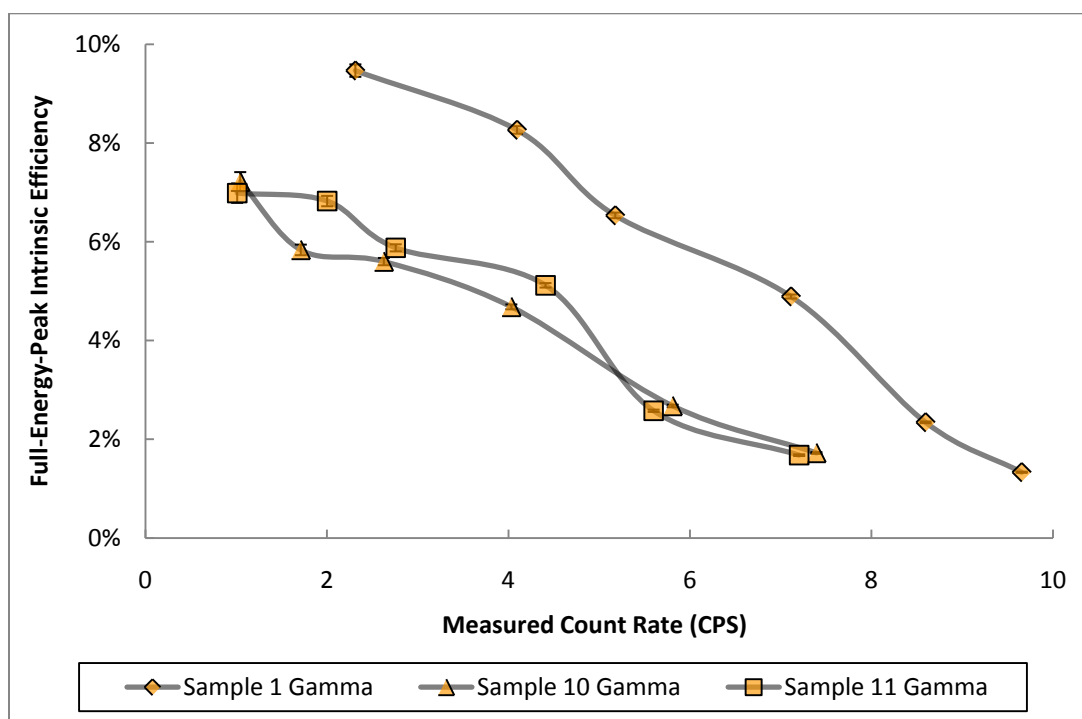


Figure 5-21: Measured intrinsic full-energy-peak efficiency in the NaI(Tl) layer for ^{137}Cs (662 keV) with varying incident count rate, in a mixed beta particle/gamma-ray radiation field, error is included per data point

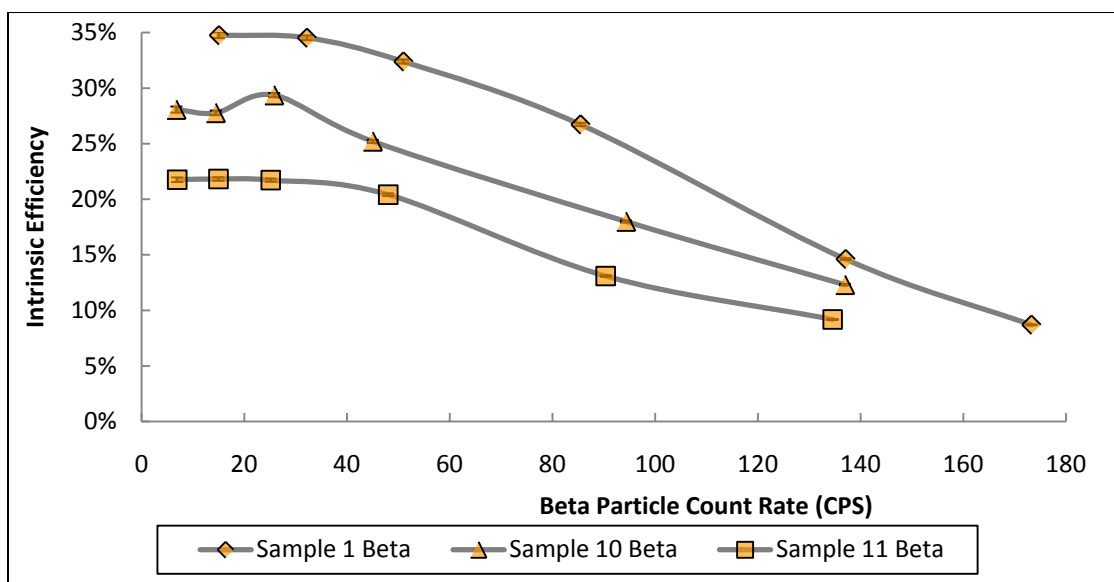


Figure 5-22: Measured beta particle intrinsic efficiencies in BC400 + CaF₂(Eu) layers with varying incident count rate, in a mixed beta particle/gamma-ray radiation field, error is included per data point

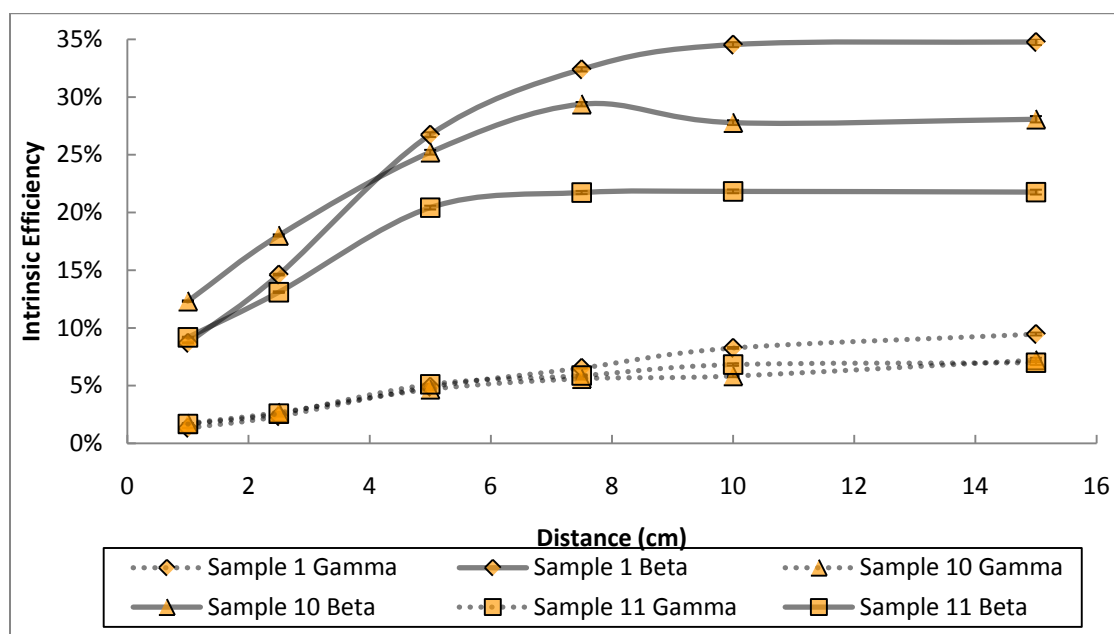


Figure 5-23: Measured beta particle intrinsic efficiencies in BC400 + CaF₂(Eu) layers and gamma-ray intrinsic full-energy-peak efficiency in the NaI(Tl) layer with varying distance between source and phoswich window, in a mixed beta particle/gamma-ray radiation field, error is included per data point

5.3 Effective Range of Measurement

The ^{133}Ba spectrum demonstrates the detection system's ability to analyze energies below 50 keV (Fig 4-1). An Analysis of this spectrum depicts an initial peak around 10 keV, which is a product of electrical noise. The second peak, marked near 30 keV, is a product of ^{133}Ba characteristic x-rays. Barium-133 has five characteristic x-rays between 30 and 36 keV, with the highest yielding x-ray (64.3 %) having a full-energy-peak of 30.973 keV (NNDC). These x-rays and a low-energy gamma-ray with full-energy-peak of 53 keV (2.2 %) contribute to the shape observed in the spectrum from 30 keV toward 80 keV (NNDC). Barium-133 emits gamma-rays with full-energy-peaks of 80 keV (34.1 %), 302 keV (18.33 %), 356 keV (62.05 %), and 384 keV (8.94 %) (NNDC). These peaks are visible in the spectrum, save for the last two full-energy-peaks, which are combined into a single feature.

The ^{24}Na and ^{38}Cl spectrum demonstrates the detection system's ability to analyze energies approaching 3000 keV (Fig 4-2). Six peaks are easily observed in the spectrum. Sodium-24 emits gamma-rays with full-energy-peaks of 2754 keV (99.85 %) and 1368 keV (99.99 %) (NNDC). Chlorine-38 emits gamma-rays with full-energy-peaks of 2167 keV (44.4 %) and 1642 keV (33.3 %) (NNDC). Both chlorine peaks appear to be broader than expected and shifted to higher energies. This is a result of counting influence exhibited by the single (2243 keV) and double (1732 keV) escape peaks created by the 2754 keV sodium full-energy-peak. The final two peaks are the annihilation peak at 511 keV and the backscatter peak at about 250 keV. The detection system should be capable of detecting energies above those present in the spectrum. However, a radioisotope which emits a gamma-ray with a full-peak-energy above 3000 keV and sufficient yield for detection, could not be obtained.

5.4 Resolution by Energy

The response of NaI(Tl) scintillators is well documented and may be described as nearly linear over typically encountered energy ranges (Valentine et al. 1998a). The primary contribution to full-energy-peak broadening is photoelectron statistics, which may be assumed

to follow Poisson statistics (Knoll 2000). The most significant contributor to photoelectron statistical fluctuation is when the number of information carriers in the signal chain is at a minimum. This generally occurs following the conversion of scintillation photons into photoelectrons by the photocathode (Knoll 2000). Figure 5-24 illustrates the measured full-energy-peak resolution for a 2.54 cm x 2.54 cm right cylindrical NaI(Tl) crystal (Valentine et al. 1998b).

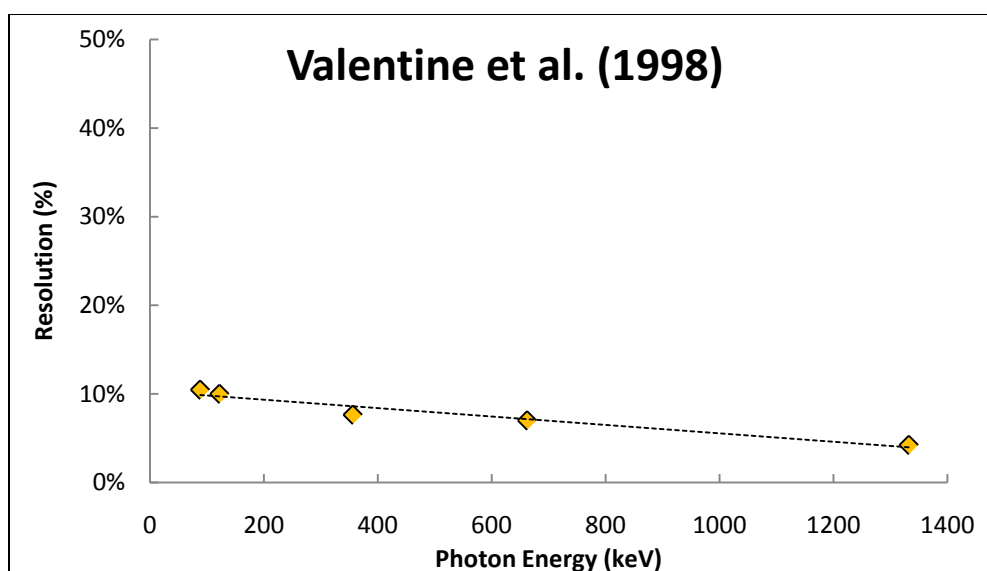


Figure 5-24: Resolution of a 2.54 cm x 2.54 cm NaI(Tl) crystal, trend line demonstrates near linear resolution by energy (adapted from Valentine et al. 1998b)

Additional contributions to broadening may be summarized into three parameters: physical characteristics of the crystal, variances introduced by the PM tube, and transfer variance (Knoll 2000). Therefore, it may be said that a scintillation detector's resolution measured at different energy should produce a relatively linear response, unique to the crystal and PM tube combination.

Figure 5-25 is a graph of the data presented in Table 4-13. The measured resolution shows linearity between all points except for the ^{57}Co peak (122 keV). Two linear trend lines were fitted to the data. The dashed line includes all full-energy-peaks, whereas the solid line excludes the

^{57}Co peak. The measured full-energy-peak resolutions are 1 or 2 % higher than, but agree with literature.

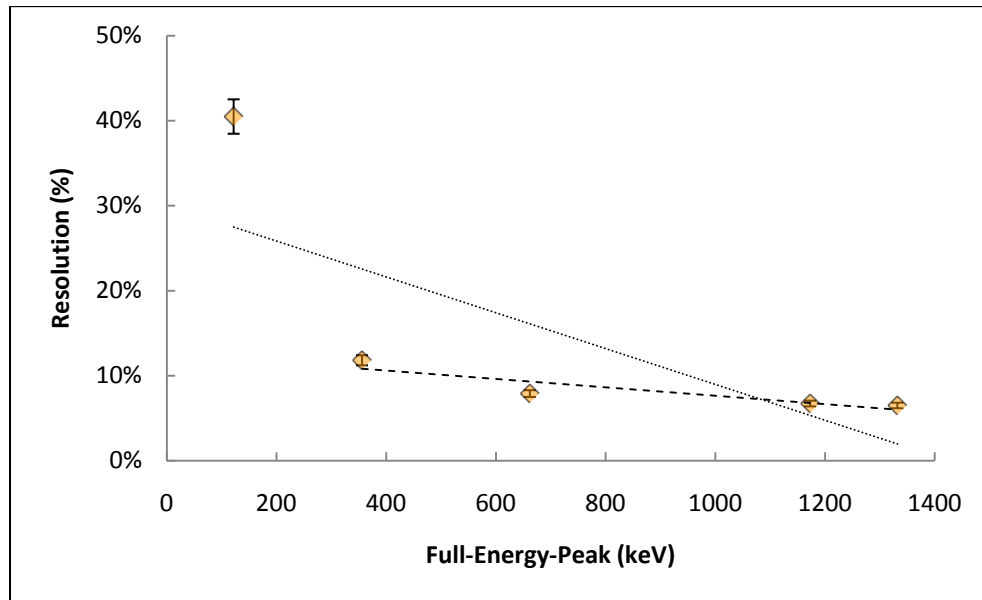


Figure 5-25: Measured full-energy-peak resolution in the NaI(Tl) layer from ^{57}Co (122 keV), ^{133}Ba (356 keV), ^{137}Cs (662 keV), and ^{60}Co (1173 and 1332 keV) sealed button sources, error is included per data point

An energy spectrum is a histogram of calculated energies and the number of bins that cover the spectrum effect the accuracy of the histogram. There is a real world trade-off that must be considered: how quickly does the spectrum need to be generated versus how accurate does the spectrum need to be. For example, a spectrum that spans from 0 to 3000 keV, which contains 100 bins, will be produced quickly. However, the result will not accurately reflect the energy of the radiation field being monitored. Likewise, the same spectrum, but containing 30000 bins, will take an exceptionally long time to produce.

Valentine et al. (1996) mathematically demonstrated that for randomly generated data, the standard deviation of the FWHM is $\leq 5\%$ of that for true Gaussian set of data if at least nine bins are contained within the FWHM energy range. The calibration function of the MATLAB codes has been set such that the FWHM of the 662 keV full-energy-peak from a ^{137}Cs source contains

10 bins. The FWHM range decreases with decreasing full-energy-peak values and the number of bins contained within the FWHM drops below 9 around 100 keV. However, this can be compensated for by collecting sufficient counts in the full-energy-peak. Figure 5-26 is taken from Valentine et al. (1996) and provides a means to assess FWHM standard deviation by the number of bins contained by the FWHM energy range. Figure 5-27 is also taken from Valentine et al. (1996) and determines number of bins required to be contained within the FWHM to maintain accurate Gaussian production of the data relative to counts inside the full-energy-peak.

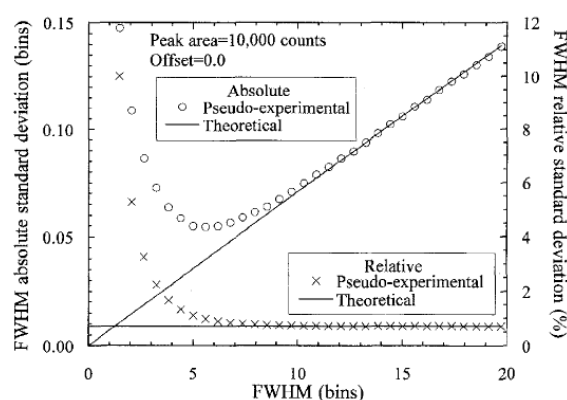


Figure 5-26: Absolute and relative standard deviation of the FWHM with varying bin number (taken from Valentine et al. 1996)

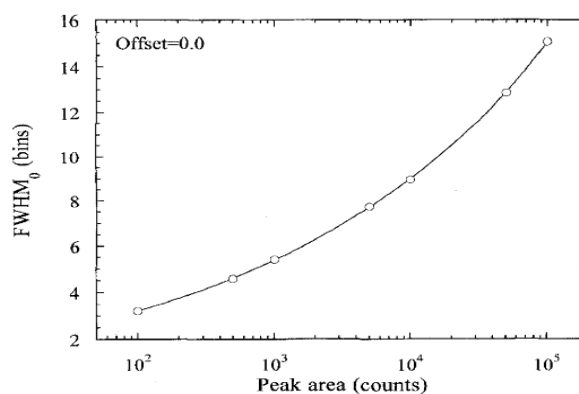


Figure 5-27: Minimum number of bins within the FWHM to maintain a FWHM standard deviation $\leq 5\%$ relative to the number of counts contained in the full-energy-peak (taken from Valentine et al. 1996)

The result from ^{57}Co is partially explained by the activity of the source relative to the MDA of the detection system. It was found that the ^{57}Co source activity was barely above the MDA for the detection system (1.29 Bq). The MDA calculation for different energy ranges is covered in the next section. As a result of the very low count rate above background, the FWHM for the 122 keV full-energy-peak could not accurately be assessed. Figure 5-28 is the ^{57}Co spectrum collected during testing. No higher activity ^{57}Co source was available.

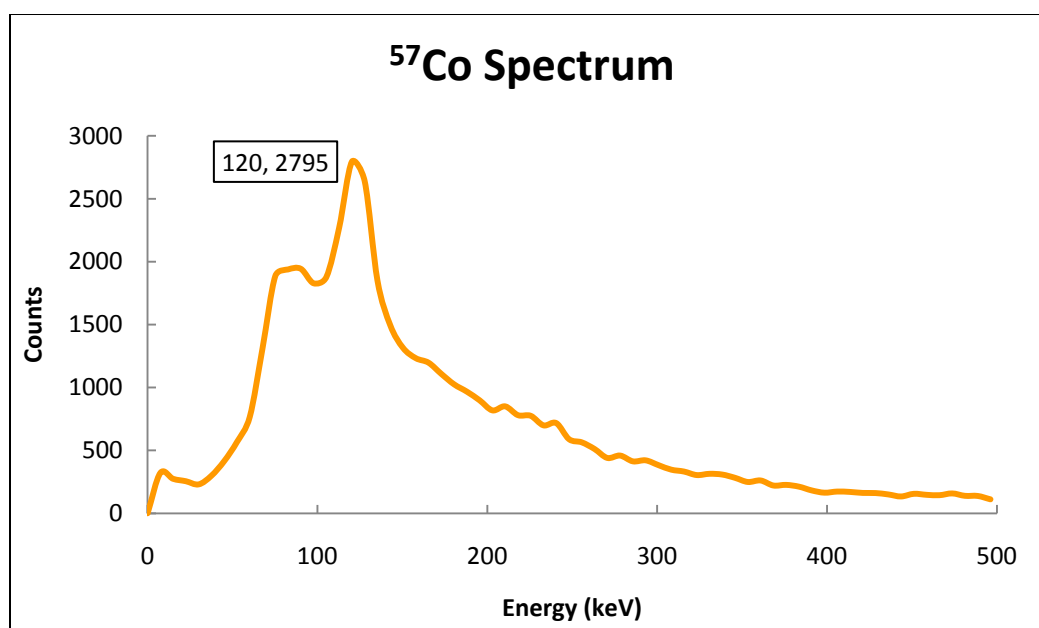


Figure 5-28: ^{57}Co spectrum, the 122 keV peak is barely above background

5.5 Minimum Detectable Activity

The minimum detectable activities calculated in Table 4-14 were based on a background spectrum collected with the exact same MATLAB code as used throughout the testing phase (Fig. 5-19). The results are specific to a particular shielding geometry and collection period. The phoswich window was not shielded throughout this work and it can be observed that there is a high level of photon background.

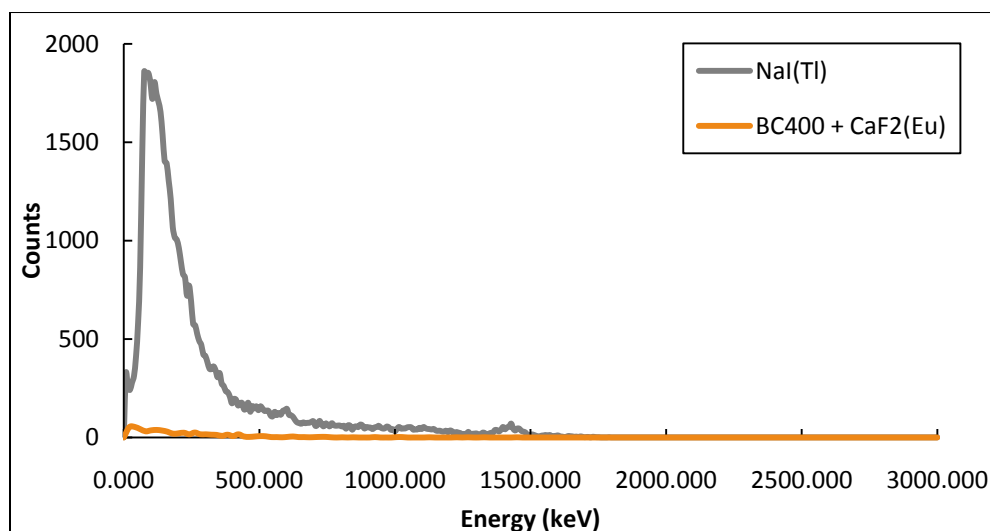


Figure 5-29: Background spectrum collected over 2579 seconds, highest photon background from ^{40}K (1460 keV), background counts increase toward the lead x-ray (77 keV)

The highest spectral energies are associated with ^{40}K (1460 keV), commonly found in building materials (Knoll 2000). Lower energies increase towards lead's characteristic x-ray (77 keV). The 'm number' effect again forced the collection period to be based on the number of pulses rather than a fixed time. For these reasons, the results presented in Table 4-14 are representative of the detector system and should only be directly applied to scenarios where the radiation source is at or near background levels. Ironically, the ^{57}Co source used to satisfy ANSI requirements is on its eleventh half-life with a calculated transformation rate of 53.7 Bq.

The calculated N_D and activities are in line with the observed background spectrum. High-energy gamma-rays and beta particles require lower counts to assess their presence as there is little background at these energies. As incident radiation energy decreases, background increases, and consequently, more incident radiation is necessary to assess the presence of real activity.

5.6 Pulse Discrimination Time

The pulse discrimination time and potential bottle-necks in the system were identified (Table 4-15). Theoretically calculated times are denoted with an * and do not incorporate overhead. The post-processing, “maximum pulse collection rate” represents the time required per pulse, to ensure the peak amplitude of the pulse corresponds to the correct range expected from trigger logic and then saving all 1024 twelve-bit sampling points that comprise the pulse. Algorithm run time was not measured since this implementation technique is suited for scientific applications, where immediate information about a radiation field is not necessary.

Real time MATLAB algorithm implementation demonstrates how slowly software runs relative to the high-speed digital electronics found on the DPP 2.0 board. The algorithm running on MATLAB takes up 92 % of the total pulse discrimination processing time. The 1024 twelve-bit data points that comprise each pulse are not saved in this implementation. However, spectral data is saved and updated in real time. The advantage is that the spectral data in total is roughly 5 KB in size, whereas each pulse is around 1.08 KB in size. As an example, considering a 250,000 pulse collection period, the resulting spectrum is still 5 KB in size, the pulse data that made up the spectrum is nearly 270 MB in size.

The RX1200 MCA Mode example demonstrates the superior algorithm run time and maximum pulse collection rate that may be attained when the algorithm is fully implemented onto a DPP. The system runs so quickly that the limiting factor becomes the longest light-decay constant in the phoswich or a user defined variable. The RX1200 analyzed was running a different algorithm than that found in the DPP 2.0 scenarios, as it was designed for a different phoswich detector. However, the algorithm methodology is unchanged and alterations were based on the light-decay constant of the differing scintillation material found in the other phoswich (BGO ~ 1000 ns light-decay constant).

The USB transfer time for the RX1200 is not the same as in the DPP 2.0 scenarios. The RX1200 algorithm run time includes updating a histogram stored in memory on the DPP board. The histogram is comprised of 4096 32-bit channels (131kb). The USB transfer time is the time

necessary to send the full histogram to the GUI, presently on a PC. A single histogram update may possess many thousand analyzed pulses. It should be noted that GUI update speed is user selectable. It is unnecessary to update the GUI thousands of times a second.

5.7 Digital Pulse Processor Programming Time

The times presented in Table 4.16 range from 61.6 to 211 milliseconds for DPP 2.0 and 3.52 to 595 milliseconds for RX1200. All times were measured in MATLAB using the tic/toc feature around relevant lines of code. In all scenarios, the initialization time required for the detection system to become operational is well below the maximum 2 minutes specified by ANSI regulations.

The GUI warm-up time refers to a scenario where the DPP has not been powered down since its last use. In this scenario, the DPP retains its programming and only requires input from the GUI to restart operation. The time difference observed the RX1200 and DPP 2.0 is mostly caused by the PC platform that each detection system is using. The RX1200 was tested on a Core-2 Duo chipset running Windows 7 and MATLAB 2010b software. The DPP 2.0 was tested on an Intel D series chipset running Windows XP Professional and MATLAB 2007a software.

The program DPP time refers to a scenario where the DPP was powered down. This necessitates that the DPP be programmed even if the GUI was not deactivated. Like in the previous scenario, the computer running the GUI plays a role in programming time. The RX1200 and DPP 2.0 are physically different and as a consequence, different sized programming files are required. The RX1200 programming file is smaller than that required by the DPP 2.0. The result is that the DPP 2.0 is much slower to program with these two factors coupled together.

There is some additional software overhead required by the GUI to program the DPP and begin operation. Both the RX1200 and DPP 2.0 use MATLAB (albeit in different capacities), which requires that all pertinent directories be loaded while the code is initiating. In other words, this time is not required to program the DPP, but is necessary to initiate operation. There are many

variables that will influence how quickly this task is completed. A few examples include the priority of the GUI/MATLAB, available system resources, folder arrangement, chipset, and processor speed.

6 Conclusion and Future Work

6.1 Conclusion

The phoswich detection system demonstrated that it is quite capable of accurately measuring the type and energy of radiation present in combined beta particle and gamma-ray radiation fields. The MATLAB algorithm effectively separates beta particle and gamma-ray interactions from X-ray and cross-talk interactions that occur within the phoswich. The MATLAB algorithm does not adversely change the overall system response to incident radiation. The BC400 and $\text{CaF}_2(\text{Eu})$ layers do not affect the efficiency or FWHM for gamma-ray interaction with the $\text{NaI}(\text{TI})$ layer. Likewise, gamma-rays do not affect beta particle detection. Gamma-rays do interact solely with the $\text{CaF}_2(\text{Eu})$ layer, but these events are effectively discarded by the algorithm. Additionally, the MATLAB code provides an excellent platform for rapid development and customization for specific collection criteria.

The phoswich detection system surpassed ANSI requirements for radiation monitors used in homeland security, which were tested. The effective range of measurement was shown to be below 50 keV and at least upwards of 2750 keV. The system's efficiency at low activity and resolution were comparable to other commercially available systems. The necessary warm-up time in the slowest scenario was less than 0.5 percent of the ANSI maximum of two minutes. It should be noted that some ANSI requirements were not tested (e.g. operating temperature range, resistance to vibration, neutron detection capability, etc.) as they did not correlate to this system's intended function or risked potential damage to the only prototype presently in operation.

The study findings also indicate that the phoswich detection system, in its present configuration of using MATLAB to operate the pulse discrimination algorithm can only collect a maximum 310 cps. The low collection rate is further hampered by an inability to assess live time versus real time. Both factors greatly impact the system's efficiency, and in-turn, its ability to quantify the activity of a radiation field. This is a significant drawback to the studied

configuration. It may be concluded that this configuration is suited for only those applications where activities are low or count rate is not important, such as acquiring a detailed spectrum, where the source can be collected over a long period of time.

6.2 Future Work

There are two topics that warrant further study. First, the algorithm needs to be exported from MATLAB and onto a DPP. Furthermore, the prototype phoswich should be replaced with an identical model to those that have been ordered by customers. Once those two changes are complete, the test conducted herein should be repeated with the new detection system and compared against the findings presented in this work to determine if there are any changes to operational characteristics. This should provide insight into three areas. First, the coding language would enable development of an accurate assessment of the live time, greatly improving performance in high radiation fields. Secondly, this should drastically improve the systems maximum collection rate, also improving efficiency measurements. Finally, this would more accurately reflect the operating parameters of the detection system for end-users.

The second topic is a more detailed analysis of the detection systems response in mixed radiation fields in close proximity to the phoswich window (less than 2.5 cm). In this study, beta particles were counted at a much higher rate at close proximity to the phoswich window. This was expected as the beta particle source activity was stronger than gamma-ray source activity. It was observed that as the distance from the window increased, fewer beta particles were detected. Again, this was expected due to the tortuous path beta particles suffer.

However, the collection rate of the studied system was too slow to analyze this in greater detail. There is the possibility that the close proximity findings were a consequence of the short light-decay constant of the BC400 layer. This raises the question; given an equal level of beta particle and gamma-ray activities penetrating the phoswich window, will beta particles satisfy trigger logic at a disproportionally higher rate? The results presented in this study do not suggest that there is a preference for beta particle detection over gamma-ray detection in mixed

fields, but they do not rule this out as a possibility. This particular characteristic may be of vital importance when beta particle and gamma-ray activities are of concern with samples measured at close proximity to the phoswich window.

7 Bibliography

- Analog Devices, *AD9230: 12-Bit, 170 MSPS/210 MSPS/250 MSPS, 1.8 V Analog-to-Digital Converter*, White Sheet, Analog Devices Inc., 2007
- American National Standards Institute (ANSI N42.34-2006), *American National Standard Performance Criteria for Hand-Held Instruments for the Detection and Identification of Radionuclides*, National Committee on Radiation Instrumentation, IEEE, 2007.
- American National Standards Institute (ANSI N42.43-2006), *American National Standard Performance Criteria for Mobile and Transportable Radiation Monitors Used for Homeland Security*, National Committee on Radiation Instrumentation, IEEE, 2007.
- Cember H., Johnson T., *Introduction to Health Physics*, 4th Edition, McGraw Hill Medical, 2009
- Childress, N., Miller, W., MCNP analysis and optimization of a triple crystal phoswich detector, *Nuclear Instruments & Methods in Physics Research*, Section A: Accelerators, Spectrometers, Detectors and Associated Equipment, A490: 263-270; 2002.
- De Celis, B., de la Fuente, R., Willart, A., de Celis Alonso, B., (2007) Coincidence Measurements in $\alpha/\beta/\gamma$ spectrometry with phoswich detectors using digital pulse shape discrimination analysis, *Nuclear Instruments and Methods in Physics Research*, A 580, 2007.
- Ely, J., Aalseth, C., Hayes, J., Heimbigner, T., McIntyre, J., Miley, H., Panisko, M., Ripplinger, M., (2003), *Novel Beta-Gamma Coincidence Measurements using phoswich detectors*, in Proceedings of the 25th Seismic Research Review – Nuclear Explosion Monitoring: Building the Knowledge Base, 2003.
- Evans, A., Orndoff, J., *Evaluation of techniques for dynamic measurement of fuel motion in liquid-metal-cooled fast-breeder reactor safety experiments*, Technical Report NUREG/CR-1398; LA-8301, Los Alamos National Lab., NM, 1980.
- Farsoni, A., Hamby, D., (2005) MCNP analysis of a multilayer phoswich detector for beta-particle dosimetry and spectroscopy, *Nuclear Instruments & Methods in Physics Research*, Section A: Accelerators, Spectrometers, Detectors and Associated Equipment. A 555, 2005.
- Farsoni, A., *Simultaneous Beta/Gamma Digital Spectroscopy*, Ph D Dissertation, Oregon State University, 2006.
- Farsoni, A., Hamby, D., (2006) *Study of a triple-layer phoswich detector for beta and gamma spectroscopy with minimal crosstalk*, in Proceedings of the 28th Seismic Research Review: Ground-Based Nuclear Explosion Monitoring Technologies, 2006.

- Farsoni, A., Hamby, D., (2007a) A system for simultaneous beta and gamma spectroscopy, *Nuclear Instruments and Methods in Physics Research*, A 578, 2007.
- Farsoni, A. T., Hamby, D., Roop, K., and Jones, S., (2007b) *A two-channel phoswich detector for dual and triple coincidence measurements of radioxenon isotopes*, in Proceedings of the 29th Monitoring Research Review: Ground-Based Nuclear Explosion Monitoring Technologies, 2007.
- Farsoni, A., Hamby, D., Lee, C., and Elliott, A., (2008) *Preliminary experiments with a triple-layer phoswich detector for radioxenon detection*, in Proceedings of the 30th Monitoring Research Review: Ground-Based Nuclear Explosion Monitoring Technologies, 2008.
- Farsoni, A., Hamby, D., (2009) *Characterization of triple-layer phoswich detector for radioxenon measurements*, in Proceedings of the 31st Monitoring Research Review: Ground-Based Nuclear Explosion Monitoring Technologies, 2009.
- Farsoni, A., Hamby, D., (2010a) *Characterizing a two-channel phoswich detector using radioxenon isotopes produced in the Oregon State University TRIGA reactor*, in Proceedings of the 31st Monitoring Research Review: Ground-Based Nuclear Explosion Monitoring Technologies, 2010.
- Farsoni, A., Hamby, D., (2010b) *Design and modeling of a Compton-suppressed phoswich detector for radioxenon monitoring*, in Proceedings of the 31st Monitoring Research Review: Ground-Based Nuclear Explosion Monitoring Technologies, 2010.
- Hartwell, J., Gehrke, R., McIlwain, M., Performance Comparison for Four Compact Room-Temperature Detectors – Two Cadmium zinc Telluride (CZT) Semiconductor Detectors, A $\text{LaCl}_3(\text{Ce})$ Scintillator, and an $\text{NaI}(\text{TI})$ Scintillator, *IEEE Nuclear Science Symposium Conference*, 2004.
- Hennig, W., Tan, H., Warburton, W., McIntyre, J., (2005) *Digital pulse shape analysis with phoswich detectors to simplify coincidence measurements of radioactive xenon*, in Proceedings of the 27th Monitoring Research Review: Ground-Based Nuclear Explosion Monitoring Technologies, 2005.
- Hennig, W., Tan, H., Warburton, W., Fallu-Labruyere, A., Sabourov, K., McIntyre, J., Cooper, M., Gleyzer, A., (2007) *Characterization of phoswich well detectors for radioxenon monitoring*, in Proceedings of the 29th Monitoring Research Review: Ground-Based Nuclear Explosion Monitoring Technologies, 2007.
- Kouzes, R., Detecting Illicit Nuclear Materials, *American Scientist*, Vol. 93, Issue 5, 2005.
- Knoll, G., *Radiation Detection and Measurement*, 3rd Edition, John Wiley and Sons, Inc. New York. 2000.

- Krane, K., *Modern Physics*, 2nd Edition, John Wiley & Sons, Inc., 1996.
- Martin, J., *Physics for Radiation Protection*, 2nd Edition, John Wiley and Sons, Inc. New York. 2006.
- Miller, W., Diaz de Leon, M., (2004) Utilization of phoswich detectors for simultaneous, multiple radiation detection, *Journal of Radioanalytical and Nuclear Chemistry*, Vol 264, No. 1, 2004.
- National Nuclear Data Center (NNDC), Chart of Nuclides, Brookhaven national Laboratory, <http://www.nndc.bnl.gov/chart/>, Accessed May, 19 2011.
- Navratil, J., Hála, J., *Radioactivity, Ionizing Radiation, and Nuclear Energy*, 2nd Edition, Konvoj, spol. s r. o., Brno, Czech Republic, 2003.
- Ponomarev, L., *The Quantum Dice*, Institute of Physics Publishing, 1993.
- Shannon, C., Communication in the presence of noise, *Proc. Institute of Radio Engineers*, Vol. 37, No. 1, 1949.
- Takada, M., Shibata, T., Uwamino, Y., Nakamura, T., A performance study on a phoswich detector consisting of an inner NE213 scintillator and an outer CaF₂:Eu crystal wall, *Nuclear Instruments & Methods in Physics Research*, Section A: Accelerators, Spectrometers, Detectors and Associated Equipment. A379:293-306; 1996.
- Turner, J., *Atoms, Radiation, and Radiation Protection*, 3rd Edition, Wiley-VCH Verlag GmbH & Co., 2007.
- Valentine, J., Rana, A., Centroid and Full-Width at Half Maximum Uncertainties of Histogrammed Data with an Underlying Gaussian Distribution – The Moments Method, *IEEE Transactions on Nuclear Science*, Vol. 43, No. 5, 1996.
- Valentine, J., Rooney, B., Dorenbos, P., (1998a) More on the Scintillation Response of NaI(Tl), *IEEE Transactions on Nuclear Science*, Vol. 45, No. 3, 1998.
- Valentine, J., Rooney, B., Li, J., (1998b) The Light Yield Nonproportionality Component of Scintillator Energy Resolution, *IEEE Transactions on Nuclear Science*, Vol. 45, No. 3, 1998.
- White, T., Miller, W., (1999) A triple-crystal phoswich detector with digital pulse shape discrimination for alpha/beta/gamma spectroscopy, *Nuclear Instruments and Methods in Physics Research*, A 422, 1999.

Yamamoto, K., Yamaura, K., Sato, K., Ota, T., Suzuki, H., Ohsuka, S., (2007) *Development of Multi-pixel photon counter (MPPC)*, Nuclear Science Symposium Conference Record, 2006.

8 Appendix A (Real Time MATLAB Algorithm)

```

clear all

addpath('C:\Program Files\Opal Kelly\FrontPanel\API\Matlab');
addpath('C:\Program Files\Opal Kelly\FrontPanel\API');

if ~libisloaded('okFrontPanel')
    loadlibrary('okFrontPanel', 'okFrontPanelDLL.h');
end;

xptr = calllib('okFrontPanel', 'okUsbFrontPanel_Construct');

xem = okusbfrontpanel(xptr);
xem = openbyserial(xem, "");

configurefpga(xem, 'top4.bit')

% Apply Reset
setwireinvalue(xem,16,4,4);
updatewireins(xem);
setwireinvalue(xem,16,0,4);
updatewireins(xem);

m = 65000; % Number of pulses to be processed
t = 0:5:5115; % Time profile, 5 ns sampling points
adc = 0:4095; % Pulse range

% Set the threshold value to trigger circular buffer data release to PC
Th = 650;
Th = uint16(Th);
setwireinvalue(xem,17,Th,65535);

% Set the gain
gain = 2650;
setwireinvalue(xem,8,24,65535);
setwireinvalue(xem,9,gain*16,65535);
updatewireins(xem);
activatetriggerin(xem,64,0);

% Set the offset
off = 1985;
setwireinvalue(xem,8,25,65535);
setwireinvalue(xem,9,(off)*16,65535);
updatewireins(xem);
activatetriggerin(xem,64,0);

% Set the RUN MODE
run_mode = 0; % Run Mode = 0 : Free Running
setwireinvalue(xem,16,run_mode*2048,14336);
setwireinvalue(xem,16,1,1);
updatewireins(xem);

%%%%%% Allocate Memory %%%%%%

valid = 0; % valid counter allocation
valid_b = 0; % valid beta counter allocation
valid_g = 0; % valid gamma counter allocation
fcr = 0; % fab allocation
scr = 0; % fbc allocation
data_1 = zeros(1,1024); % size of each array that comprises a pulse

```

```

f1 = [ones(1,10)*-1 ones(1,10)*1]; % Fast Filter
f2 = [ones(1,60)*-1 ones(1,60)*1]; % Medium Filter
f3 = [ones(1,600)*-1 ones(1,600)*1]; % Slow Filter

max_ca = 1000; % max beta energy CaF2 layer
max_b = 1000; % max beta energy
max_g = 1000; % max gamma energy NaI(Tl)
bin_b = 150; % Total beta bins
bin_g = 400; % Total gamma bins
ebin_b = 0: max_b/(bin_b-1) : max_b; % x-axis bin size for betas
ebin_g = 0: max_g/(bin_g-1) : max_g; % x-axis bin size for gammas
amp_b = zeros(1,m); % BC400 amplitude allocation
amp_bf = 0; % builds array of beta amplitudes
amp_g = zeros(1,m); % NaI(Tl) amplitude allocation
amp_gf = 0; % builds array of gamma amplitudes
amp_ca = zeros(1,m); % CaF2 amplitude allocation
spec_b = zeros(1, length(ebin_b)); % beta spectra allocation
spec_g = zeros(1, length(ebin_g)); % gamma spectra allocation

a_ca = 0; % CaF2 calibration constant
a_bc = 0; % BC400 calibration constant
a_g = 0; % NaI(Tl) calibration constant
b_ca = .012; % CaF2 calibration coefficient
b_bc = .05; % BC400 calibration coefficient
b_g = .01165; % NaI(Tl) calibration coefficient

%%%%%%%%%% Data Acquisition %%%%%%%%%%%%%%

while valid ~=m; % Run "while" loop when valid is not equal to m

    updatewireouts(xem);
    pt=getwireoutvalue(xem,32);

    while bitand(pt,1) ==0
        updatewireouts(xem);
        pt=getwireoutvalue(xem,32);
    end

    if (m==valid+1) % Stop "while" loop when valid + 1 is equal to m
        setwireinvalue(xem,16,0,3);
        setwireinvalue(xem,16,0,14336);
        updatewireins(xem);
    end

    buf_1 = readfrompipeout(xem,160,2048); %CH 1
    k=1:1:1024;
    j=k*2;
    data_1(k)=uint16(buf_1(j))*256 + uint16(buf_1(j-1));

    data_1 = double(data_1); % Sets double precision so that integers may be used without failure
    [mn i] = min(data_1); % Locate the minimum value and index from data_1 array (1x1024 array)

    if mn > 0 && i > 95 && i < 125 % Logic set to determine if data_1 is a valid pulse from detector utilizing the array minimum and it's
index.

        valid = valid + 1; % Counter for valid pulses

        base = mean(data_1(i-80:i-70)); % Establish a baseline value before the peak
        a1 = mean(data_1(i+50:i+60)); % Establish a value after the peak
        relax = (a1-mn)/(base-mn); % Parameter that relates the baseline before and after the peak. Used to limit the effect of ringing
found in very fast pulses
        data = [ones(1,1700)*base data_1]; % Additional baseline data is added to the pulse to aid convolution.

```

```

con1 = conv(data,f1); % applying BC400 filter
con2 = conv(data,f2); % applying NaI filter
con3 = conv(data,f3); % applying CaF2 filter

fa = max(con1(1700:2650)); % Max integrated area of data_1 from fast filter
fb = max(con2(1700:2650)); % Max integrated area of data_1 from medium filter
fc = max(con3(1700:2650)); % Max integrated area of data_1 from slow filter

fcr = fa/fb; % Ratio faster filter to medium filter - FCR
scr = (fb-fa)/(fc-fa); % Ratio of percent medium filter over percent slow filter - SCR

ind1 = scr<0; % index of the fab array value < 0
ind2 = scr>1; % index of the fbc array value > 1
ind3 = relax>0.95; % index decay > 0.95

scr(ind1) = 0; % when ind1 true, fbc = 0
scr(ind2) = 1; % When ind2 true, fbc = 1
fcr(ind3) = 1; % When ind3 true, fab = 1

pause(0.0001)

end

%%%%%%%%%%%%%%%%%%%%%%%%%%%%%%%%%%%%%%%%%%%%%%%%%%%%%%%%%%%%%%%%%%%%%%%% Energy Calibration and Output %%%%%%%%%%%%%%%

%%%%%%%%%%%%%%%%%%%%%%%%%%%%%%%%%%%%%%%%%%%%%%%%%%%%%%%%%%%%%%%%%%%%%%%% CaF2 and BC400 %%%%%%%%%%
if (scr < 0.425 && scr > 0.2 && fcr > 0.25) || (fcr == 1) % Set region of pure beta interaction in CaF2 and/or BC400

    valid_b = valid_b + 1; % valid beta counter
    data_beta = [fa fb fc fcr scr]';

    amp_ca (valid_b)= a_ca + b_ca * (fc-fa); % area of slow component after fa
    amp_b (valid_b)= (a_bc + b_bc * (fa - (0.0756 * (fc-fa)))) + amp_ca(valid_b); % area of fa plus slow component after fa
    amp_bf = [amp_bf;amp_b];

    spec_b = hist(amp_b,ebin_b);
    spec_b(1) = 0;
    spec_b(bin_b) = 0;

    subplot(2,1,1)
    plot(ebin_b,spec_b,'.b','LineWidth',2,'MarkerSize',5),xlabel('Beta: Energy (keV)'),ylabel('Counts')

%%%%%%%%%%%%%%%%%%%%%%%%%%%%%%%%%%%%%%%%%%%%%%%%%%%%%%%%%%%%%%%%%%%%%%%% NaI %%%%%%%%%%
elseif scr < 0.75 && scr > 0.45 && fcr < 0.25 && fcr > 0.15 % Set region for pure gamma NaI(Tl) interaction

    valid_g = valid_g + 1; % valid gamma counter
    data_gamma = [fa fb fc fcr scr]';

    amp_g (valid_g)= a_g + b_g*fb; % area calibration equation for gamma pulses
    amp_gf = [amp_gf;amp_g];

    spec_g = hist(amp_g,ebin_g);
    spec_g(1) = 0;
    spec_g(bin_g) = 0;

    subplot(2,1,2)
    plot(ebin_g, spec_g,'.r','LineWidth',2,'MarkerSize',5),xlabel('Gamma: Energy (keV)'),ylabel('Counts')
end

end

```

9 Appendix B (Filter Sizes)

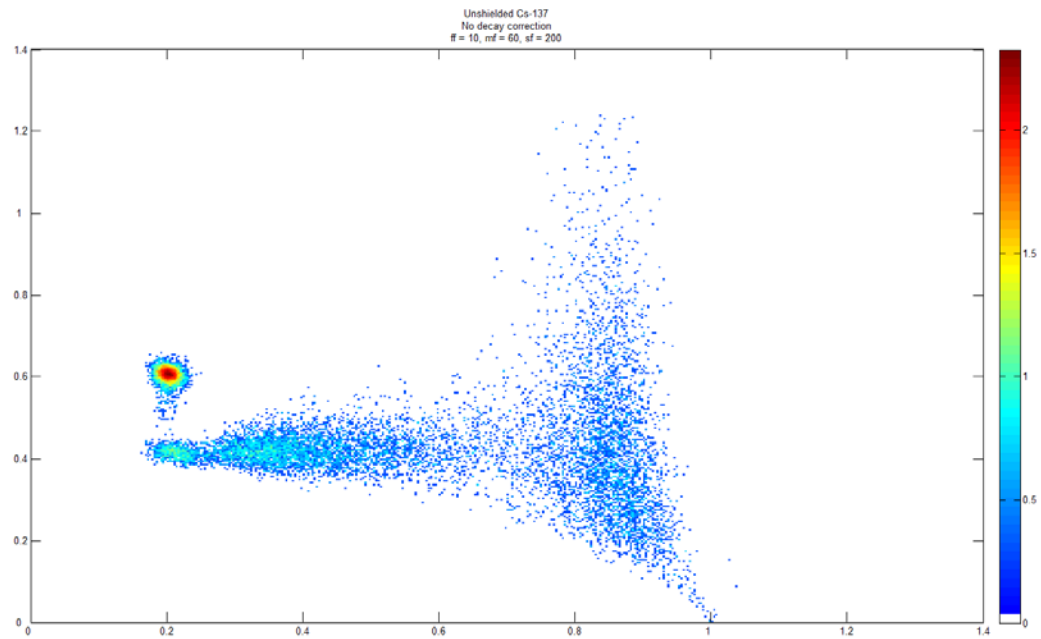


Figure 9-1: FCR/SCR 2D histogram for an unshielded ^{137}Cs source; $f_a = 10$, $f_b = 60$, $f_c = 200$

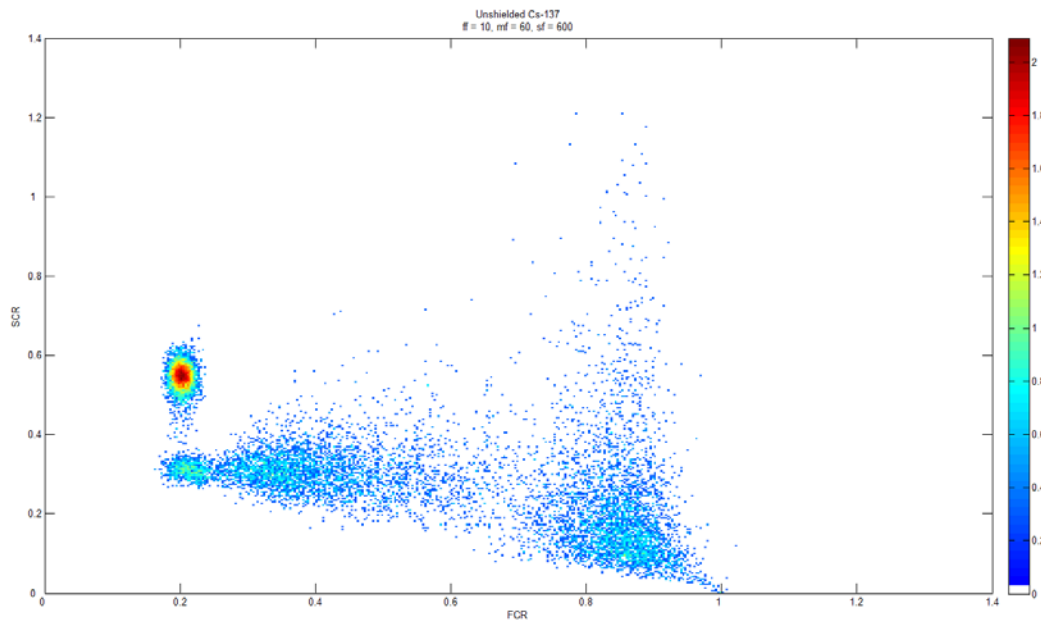


Figure 9-2: FCR/SCR 2D histogram for an unshielded ^{137}Cs source; $f_a = 10$, $f_b = 60$, $f_c = 600$

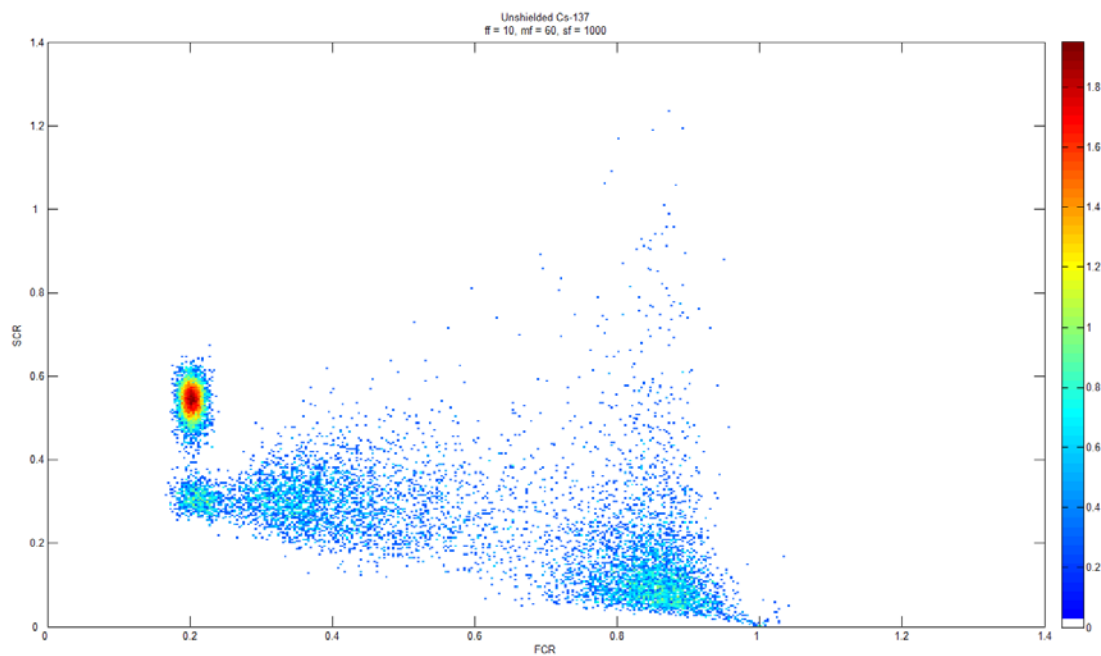


Figure 9-3: FCR/SCR 2D histogram for an unshielded ^{137}Cs source; $f_a = 10$, $f_b = 60$, $f_c = 1000$

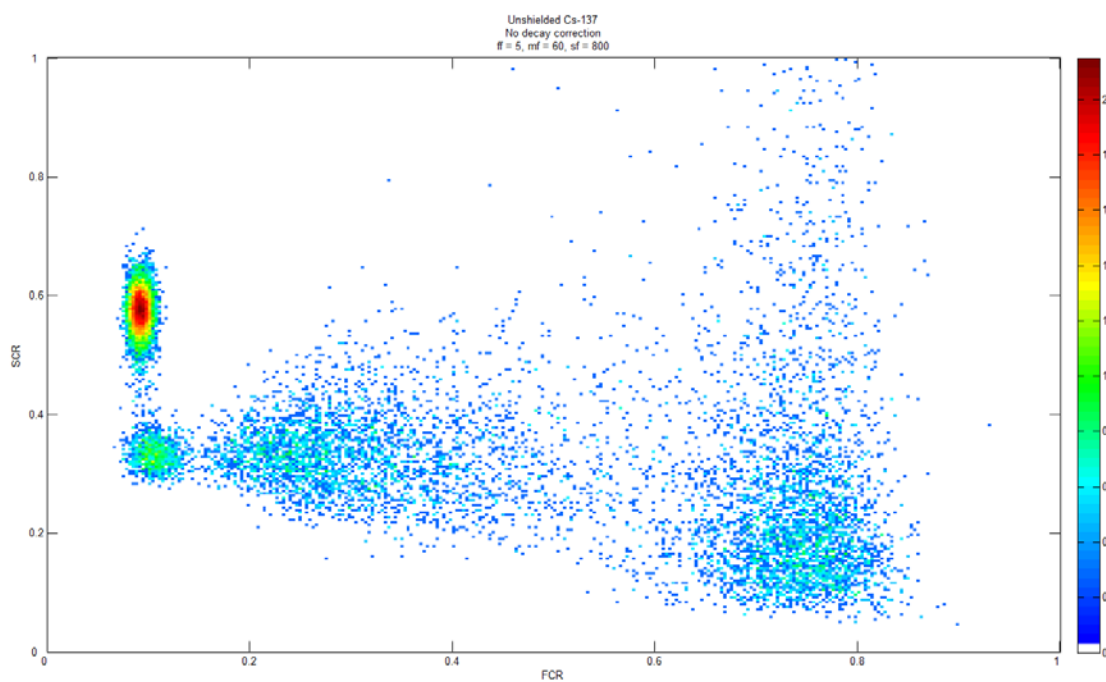


Figure 9-4: FCR/SCR 2D histogram for an unshielded ^{137}Cs source; $f_a = 5$, $f_b = 60$, $f_c = 800$

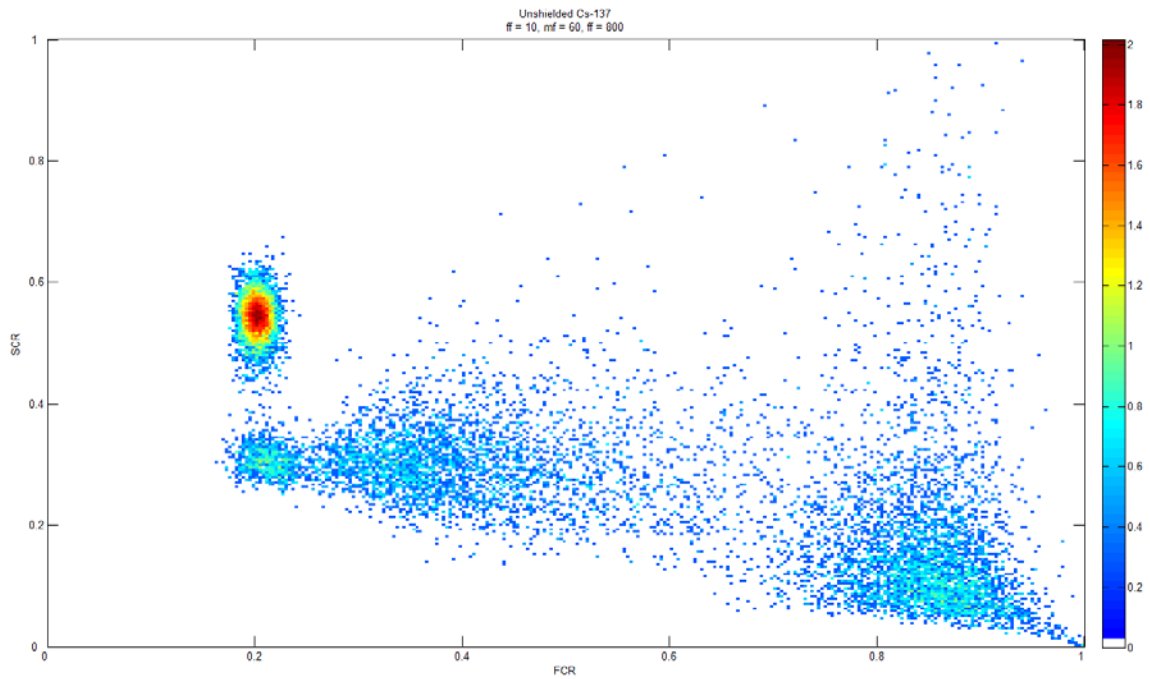


Figure 9-5: FCR/SCR 2D histogram for an unshielded ^{137}Cs source; $f_a = 10$, $f_b = 60$, $f_c = 800$

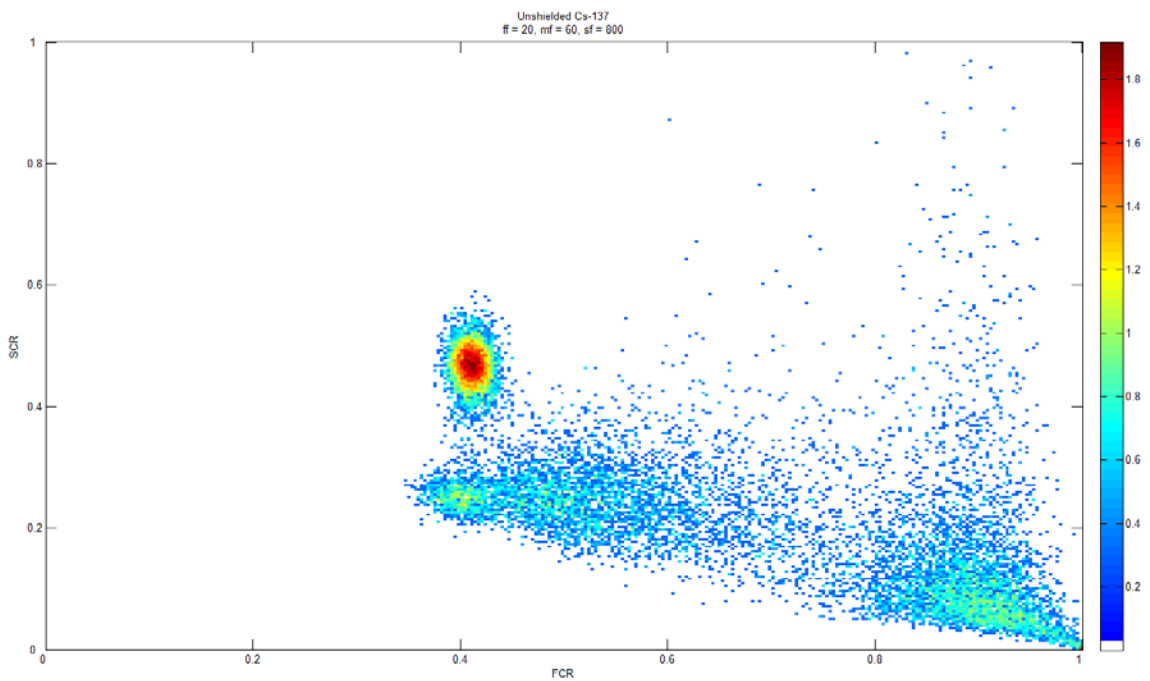


Figure 9-6: FCR/SCR 2D histogram for an unshielded ^{137}Cs source; $f_a = 20$, $f_b = 60$, $f_c = 800$

